
Politecnico di Torino

Master's Degree in Materials Engineering

Academic Year 2024/2025

Graduation Session October 2025

# Optimization of Solution Heat Treatment for a Novel Nickel-Base Superalloy Design for PBF-LB Process

**Academic supervisor:**
Prof. Daniele Ugues
**Industrial supervisor:**
Prof. Håkan Brodin - Siemens Energy

**Candidate:**
Gregorio Nikita Bersano

# Abstract

This thesis work, carried out at the Siemens Energy site in Finspång (Sweden), investigates the high-temperature behavior of a new superalloy (SAM), design to be processed by means of Laser Beam Powder Bad Fusion (LB-PBF) . The focus was placed on the formation and evolution of strengthening phases, precipitates and recrystallization, as function of different heat treatment temperatures. Thermo-Calc simulations were initially performed to understand phase stability and identify an appropriate heat treatment window, avoiding the occurrence of *incipient melting*. However, the database available for nickel-based superalloys includes only commercial alloys, whose chemical compositions differ significantly from that of SAM, leading to notable discrepancies with experimental observations. To improve predictive accuracy, future work will integrate experimental differential scanning calorimetry (DSC) data and additional characterization results into the computational model. The first cycle of heat treatments, consisting of three sequential steps—HIP, solution treatment, and aging—showed that the proposed temperatures were insufficient to trigger significant recrystallization, although preliminary indications of *grain boundary serration* were observed. These results suggest the potential for controlling microstructure by combining temperature and cooling rate. Further studies on the serration mechanism are required to subsequently analyze its influence on creep properties. Solution heat treatments conducted between 1180 °C and 1280 °C revealed more pronounced grain growth at 1200 °C, but still insufficient to maximize creep properties. At higher temperatures, the formation of a metastable phase appears to limit grain mobility, hindering their growth. Future work will focus on identifying and characterizing this phase to clarify the formation mechanism and explore possible mitigation strategies under process conditions. The effect of cooling rate from 1240 °C was also studied. Slow cooling likely allows atomic diffusion at grain boundaries, resulting in the disappearance of the metastable phase, while rapid cooling preserves its presence. The exact onset temperature of phase formation lies between 1220 and 1240 °C. Preliminary DSC results indicate a weak peak at 1215 °C, almost negligible, yet representing the only evidence of a phase change before the melting peak at 1330 °C. This work highlights the interaction between heat treatment parameters, phase evolution, and microstructural control in the SAM superalloy and its resulting properties. The combined experimental and computational approach provides a pathway to optimize heat treatment processes and, consequently, maximize creep properties for an alloy intended to operate at the highest temperatures encountered in a gas turbine.

# Abstract

Questo lavoro di tesi, svolto presso la sede di Siemens Energy a Finspång (Svezia), indaga l'ottimizzazione del trattamento termico di solubilizzazione per una nuova superlega (SAM), progettata per essere processata trameite *Laser Beam Powder Bad Fusion* (LB-PBF). Il focus è stato posto sulla formazione ed evoluzione delle fasi rinforzanti e dei precipitati, la ricristallizzazione e l'influenza di diverse temperature di trattamento sulle proprità miscrostrutturali del SAM. Le simulazioni con Thermo-Calc sono state inizialmente effettuate per comprendere la stabilità delle fasi ed individuare una finestra di trattamento termico adeguata, evitatno il fenomeno di *incipient melting*. Tuttavia, il database disponibile per le superleghe di nickel, inlcude soltando superleghre commerciali, che hanno composizioni chimiche che differiscono molto da quella del SAM, causando discrepanze significative con le osservazioni sperimentali. Per migliorare l'accuratezza predittiva, il lavoro futuro prevede l'integrazione dei dati sperimentali della calorimetria differenziale (DSC) e di ulteriori risultati di caratterizzazione nel modello computazionale. Il primo ciclo di trattamenti termici, consistente in tre step consequenziali: HIP, solubilizzazione ed invecchiamento, ha mostrato che le temperature proposte non erano sufficienti a innescare una ricristallizzazione significativa, sebbene siano state osservate indicazioni preliminari di *grain boudary serration*. Questi risultati suggeriscono la potenzialità e la possibilità di controllare la microstruttura combinando temperatura e velocità di raffreddamento. Sono necessari ulteriori studi sul meccanismo di *serration*, per poi analizzarne l'influenza sulle proprietà a creep. I trattamenti termici di solubilizzazione, eseguiti tra 1180°C e 1280°C hanno mostrato una crescita più evidente dei grani a 1200 °C, ma ancora insufficiente a massimizzare le proprietà di creep. A temperature più elevate, la formazione di una fase metastabile sembra limitare la mobilità dei grani, ostacolandone la crescita. Il lavoro futuro sarà dedicato all'identificazione e alla caratterizzazione di questa fase per chiarire il meccanismo di formazione e individuare possibili strategie di mitigazione nelle condizioni di processo. È stato inoltre studiato l'effetto della velocità di raffreddamento da 1240 °C. Il raffreddamento lento probabilmente consente la diffusione atomica ai bordi di grano, con conseguente scomparsa della fase metastabile, mentre il raffreddamento rapido ne preserva la presenza. L'esatta temperatura di onset della formazione della fase è compresa nel range tra 1220 e 1240 °C.. I risultati preliminari della DSC indicano un debole picco a 1215 °C, quasi trascurabile, ma allo stesso tempo, unica evidenza di un cambiamento di fase, prima del picco di fusione a 1330°C. Questo lavoro evidenzia l'interazione tra parametri di trattamento termico, evoluzione delle fasi e controllo microstrutturale nella superlega SAM e le sue conseguenti proprità. L'approccio combinato sperimentale e computazionale fornisce una strada per ottimizzare i processi di trattamento termico e massimizzare di conseguenza le proprietà a creep per una lega destinata ad operare alle più alte temperature presenti in una turbina a gas.

# Contents

# Chapter 1

# Introduction and State of Art

Superalloys are a family of high-performance metallic materials developed to withstand extreme conditions of temperature, stress, and corrosion, making them indispensable in industries where reliability and durability are critical. Their origins date back to the 1940s, when the rapid development of gas turbine engines during the Second World War created the need for materials that could retain mechanical strength and chemical stability at temperatures approaching or even exceeding half their melting point. Nickel-based alloys, first used in early turbojet engines, quickly proved to be superior than conventional steels.

What distinguishes superalloys is the unique combination of high-temperature strength, creep and oxidation resistance, and microstructural stability. One of the most remarkable features of superalloys is their ability to retain high mechanical strength at elevated temperatures—often up to 80% of their absolute melting point. This, combined with excellent resistance to hot corrosion and oxidation, makes them uniquely suited for service in environments where other materials would rapidly degrade. As a result, nickel-based superalloys are the material of choice for the hottest sections of gas turbine engines, where they can operate at temperatures approaching 1000°C [1]. This performances are achieved through carefully controlled compositions and the presence of ordered intermetallic phases, such as the $\gamma'$ precipitates in nickel-based systems, which allow the material to sustain high loads for prolonged periods. Over time, advances in alloy chemistry, solidification control, and thermomechanical processing have led to multiple generations of superalloys, each offering incremental improvements in temperature capability and mechanical reliability.

Today, superalloys are found in a wide range of critical applications, from the hot sections of aircraft and industrial gas turbines engines to components for nuclear reactors, chemical processing plants, and even space exploration systems. Their ability to perform in such demanding environments has made them central to progress in energy efficiency, propulsion technologies, and safety standards. Despite their maturity, research on superalloys remains active, driven by the constant push for higher operating temperatures, better oxidation resistance, and compatibility with new manufacturing routes like additive manufacturing processes.

## 1.1 Ni-based superalloys

Nickel, the principal element in Ni-based superalloys, crystallizes in a face-centered cubic (FCC) structure, also known as the gamma ($\gamma$) phase. In this arrangement, each unit cell contains atoms at the eight corners of a cube and at the centers of all six faces. This structure is stable from room temperature up to the melting point of nickel (1455°C) and imparts the alloy with high ductility and toughness. Nickel's density is approximately 8.9 g/cm$^3$, and its FCC structure is a key factor in its ability to accommodate a wide range of alloying elements, which is essential for the development of superalloys with tailored properties.
The FCC $\gamma$ matrix serves as the continuous phase in which other strengthening phases and secondary particles are embedded. The stability of this structure at high temperatures is crucial for maintaining the mechanical integrity of components exposed to extreme service conditions [2].

### 1.1.1 Strengthening Mechanisms

Nickel-based superalloys owe their exceptional high-temperature strength to a synergistic combination of microscale mechanisms that are engineered through chemistry design and tailored heat treatment. The principal contributors are (i) precipitation strengthening by ordered $\gamma'$ (Ni3(Al,Ti,Ta,Nb)) and, in some alloys, $\gamma''$ (Ni3Nb) phases; (ii) solid-solution strengthening provided by refractory and late transition elements (e.g., Re, W, Mo, Ta); (iii) coherency and misfit stresses at $\gamma/\gamma'$ interfaces; (iv) grain-boundary engineering and carbides/borides distributions.

#### 1.1.1.1 Precipitation Strengthening

Precipitation strengthening is dominant in most commercial alloys. Coherent, ordered $\gamma'$ precipitates impede dislocation motion either by being sheared (for small, coherent precipitates) or by forcing dislocations to bypass particles by Orowan looping when precipitates are larger or more widely spaced. The strengthening stress due to Orowan looping is often expressed as:

$$\tau_{\text{Orowan}} \approx \frac{Gb}{L}, \tag{1.1}$$

where $G$ is the shear modulus, $b$ the Burgers vector, and $L$ the effective interparticle spacing. The resultant strength depends critically on $\gamma'$ volume fraction, size, spacing, and interfacial coherency, all of which are set by alloy chemistry and aging treatments [1, 3].

#### 1.1.1.2 Solid-Solution Strengthening

Solid solution strengthening supplements precipitation effects and becomes especially important at elevated temperatures. Slow-diffusing refractory solutes (Re, W, Mo) increase lattice friction and retard diffusion-controlled processes such as dislocation

climb. The contribution from solid solution strengthening can be approximated by:

$$\Delta\tau_{\text{ss}} \propto \sum_i \epsilon_i^{3/2} c_i^{1/2}, \tag{1.2}$$

where $\epsilon_i$ is the size mismatch parameter and $c_i$ the atomic concentration of solute $i$. Refractory enrichment must be balanced against segregation and the risk of deleterious phase formation [4, 5].

#### 1.1.1.3 Interface Effects and Rafting

Interfacial misfit strains between $\gamma$ and $\gamma'$ phases generate internal stress fields that modify how dislocations interact with precipitates. Controlled positive or negative lattice misfits can increase resistance to dislocation motion and influence high-temperature morphological evolution. Under sustained stress, $\gamma'$ may undergo directional coarsening ("rafting"), which alters creep resistance depending on stress state and crystallographic orientation [5, 1].

#### 1.1.1.4 Grain Boundary Carbides and Borides Strengthening

Grain boundaries, carbides, and other second phases like borides play a dual role: they can strengthen by pinning grain boundaries and retarding grain boundary sliding (beneficial for creep and rupture resistance), yet they are also preferred sites for brittle phase formation and cavitation under long-term exposure. Thus, design strategies often aim to optimize grain size and boundary chemistry (including controlled precipitation of stable MC- and $M_{23}C_6$-type carbides), to maximize creep life while retaining fracture toughness and fatigue resistance.

### 1.1.2 Effect of alloying elements

The superior properties of Ni-based superalloys are achieved through the deliberate addition of a variety of alloying elements, each serving specific functions:

- Aluminum and titanium (or tantalum): promote the formation of $\gamma'$ precipitates, which are the primary source of precipitation strengthening.
- Chromium: enhances oxidation and corrosion resistance by forming a protective oxide layer.
- Cobalt: stabilizes the FCC structure and improves high-temperature strength.
- Molybdenum, tungsten, rhenium: provide solid solution strengthening and improve creep resistance.
- Niobium, tantalum: contribute to the formation of $\gamma''$ or $\gamma'$ when they replace Ti.

- Hafnium, zirconium, chromium: form borides and carbides that stabilize grain boundaries and control grain size.

The interplay between these elements determines the final microstructure and properties of the alloy. For example, high chromium content improves corrosion resistance but may reduce the solubility of $\gamma'$ formers, while minor additions of boron and carbon are critical for grain boundary strength but must be carefully controlled to avoid embrittlement.

### 1.1.3 Topologically Close-Packed (TCP) Phases

Topologically close-packed (TCP) phases are a class of intermetallic compounds that commonly form in Ni-based superalloys containing high concentrations of refractory elements such as Re, W, Mo, and Ru. While they are thermodynamically stable under certain conditions, their formation is generally detrimental to mechanical properties because they deplete the matrix of strengthening elements and act as brittle phases that can initiate cracks [6, 7]. TCP phases form due to the local enrichment of refractory elements and the reduction of Gibbs free energy through ordering into complex crystallographic structures such as $\sigma$, $\mu$, P, and R phases. Their precipitation is strongly influenced by temperature, alloy composition, and processing history. High concentrations of elements like Re and W promote the nucleation of TCP phases, particularly during long-term exposure at intermediate temperatures (700–1000°C) [8, 9].
TCP phases can reduce the volume fraction of $\gamma'$ precipitates and deplete solid solution strengthening elements, resulting in lower creep strength and ductility. They often nucleate at grain boundaries, interdendritic regions, or at interfaces with $\gamma'$ precipitates, which increases susceptibility to crack initiation under stress [10, 11]. Their morphology and distribution are critical; for example, fine, dispersed TCP phases may have less impact than coarse, continuous networks along grain boundaries.
To minimize TCP formation, alloy designers limit the total content of TCP-forming elements and carefully balance the ratio of refractory solutes. Heat treatments and aging schedules are also optimized to promote the stability of $\gamma'$ and $\gamma''$ phases while suppressing TCP nucleation. Addition of Ru has been shown to stabilize the matrix and slow TCP formation by altering diffusion kinetics and phase equilibria [9]. Thermodynamic modeling (e.g., CALPHAD) and experimental validation are widely used to predict the onset and growth of TCP phases in complex superalloys.

### 1.1.4 Carbides and Borides

Carbides and borides are secondary phases commonly used in Ni-based superalloys to improve high-temperature strength, creep resistance, and grain boundary stability. They are formed and tuned during solidification, heat treatment, or service exposure and are usually localized at grain boundaries [6, 12].
The most common carbides in Ni-based superalloys include MC, $M_{23}C_6$, and $M_6C$ types. MC carbides are typically rich in Ti, Ta, Nb, or Hf and precipitate during solidification, providing grain boundary pinning that reduces grain growth at high

temperatures. $M_{23}C_6$ carbides often form during aging or long-term service and are enriched in Cr, stabilizing grain boundaries against creep and sliding [6, 3]. This transformation can be represented as a chemical reaction between the matrix and MC-type carbides:

$$\gamma + \mathrm{MC} \longrightarrow \mathrm{M_{23}C_6} + \gamma' \tag{1.3}$$

The strengthening effect of carbides can be described qualitatively as a barrier to grain boundary motion and dislocation climb, improving creep resistance. However, excessive carbide formation, particularly coarse or continuous networks, can embrittle the component, it's important to reach the right fraction, shape and distribution of the carbides.

Here, the MC carbide (typically TiC, TaC of HfC) partially dissolves, and Cr from the matrix diffuses to form the more stable $M_{23}C_6$ at intermediate temperatures ( 700–900°C), depending on the particular alloy [6, 3, 12].

Borides, such as $M_3B_2$ and $M_5B_3$, typically contain refractory elements like Ti, Mo, and W. They contribute to grain boundary strengthening by pinning and stabilizing the microstructure at elevated temperatures. Boron additions are often minor (ppm levels) but are highly effective in improving grain boundary cohesion and ductility, especially during long-term high-temperature service [1, 12]. Alloy design must balance the benefits of carbides and borides against their potential to cause embrittlement. Controlled chemistry and heat treatment optimize particle size, distribution, and morphology. For instance, adjusting Ti, Ta, Nb, and C contents regulates MC carbide precipitation, while minor B additions enhance boride formation and grain boundary cohesion without forming excessive brittle phases.

### 1.1.5 Overview of SAM alloy

Currently, Additive Manufacturing (AM) by means of Laser Powder Bed Fusion (L-PBF) is largely limited to reasonably weldable alloys. These materials are mainly used in the cold sections of turbines and, to a certain extent, in the combustor area, where metal temperatures are still moderated by compressor cooling air. However, to fully exploit the design freedom and efficiency potential of AM, the ability to manufacture turbine components for the hot gas path downstream of the combustor is highly desirable. Such an advancement could lead to significant efficiency gains and provide a competitive advantage in the field of land-based gas turbines.
The main obstacle to this progress lies in the fact that Ni-based superalloys, which are typically employed in hot gas path components due to their outstanding high-temperature strength and oxidation resistance, are hardly weldable or even considered non-weldable. This poor weldability leads to high cracking susceptibility and inconsistent component quality when these alloys are processed by AM. Currently, there is no commercially available turbine alloy that fully addresses these limitations, and even the most promising candidates represent compromises between processability and high-temperature performance.

The SAM project is a trilateral, ongoing research collaboration between the Technical University of Braunschweig (Institute for Materials, Germany), VDM Metals International GmbH (Germany), and Siemens Energy (Sweden - Germany). The main objective of this collaboration is the design and development of an advanced nickel-based superalloy specifically tailored for additive manufacturing (AM), with a particular focus on hot gas path components in gas turbines, where extreme thermal and mechanical conditions demand exceptional material performance.
Unlike many development programs that aim to modify or adapt existing alloys, the SAM project deliberately follows a "clean sheet" alloy design approach, meaning that the chemical composition and microstructural concept were conceived from scratch. This strategy enables a level of compositional freedom and microstructural tailoring not achievable when working within the constraints of existing alloy families. As a result, the alloy under development is chemically and metallurgically unique.

The driving motivation for this novel design is to address the key limitations of currently available alloys used in AM for turbine components. Many conventional superalloys either exhibit poor weldability and high cracking susceptibility during the layer-by-layer build process and subsequent heat treatments, or they lack the high-temperature strength and creep resistance needed for long-term operation in hot gas path environments. The SAM alloy development therefore seeks to achieve a balanced performance profile, combining low cracking susceptibility during AM and post-processing with high mechanical strength, creep resistance, and oxidation resistance at elevated temperatures.
A core innovation in the alloy design is the exploitation of a peculiar chemistry, which enables precise tuning of the $\gamma'$ (gamma prime) solvus temperature and volume fraction, key parameters for high-temperature strength and microstructural stability. Additionally, the effects of minor alloying elements have been systematically investigated, with particular attention to hafnium additions, which have been found to influence microstructural evolution.

## 1.2 CALPHAD method, ThermoCalc software

Thermo-Calc is an advanced thermodynamic software for modelling and predicting phase equilibria and thermodynamic properties in metallic, ceramic, and polymeric materials. It is based on the CALPHAD method (CALculation of PHAse Diagrams), a computational approach that integrates thermodynamic models with experimental data to describe the behaviour of multicomponent systems. At the core of CALPHAD is the representation of the Gibbs free energy of each phase in a system as a function of chemical composition, temperature, and pressure. The parameters of these models are obtained through numerical optimization, comparing calculated results with experimental measurements. Once calibrated, the models can interpolate and even extrapolate material properties beyond the specific conditions tested experimentally.
Thermo-Calc relies on specialized thermodynamic databases, which contain sets of

polynomials describing the properties of individual phases in a system as functions of temperature, pressure, and composition. These polynomials are formulated in terms of Gibbs free energy functions, from which other thermodynamic properties can be derived.
The software complete the simulation by the "basic" principle of minimization of the total Gibbs free energy under given conditions.
These databases are developed according to CALPHAD principles and may also include kinetic data when used with the dedicated diffusion simulation module. With these tools, users can compute phase diagrams, thermodynamic properties (enthalpy, entropy, heat capacity), driving forces for phase transformations, and equilibrium compositions, even for complex multicomponent systems. In this work, the reference database used was TTNi8, the standard for nickel-based superalloys. Among the various objectives of the simulations was to assess whether the SAM alloy could be accurately "simulated," given that its unique chemistry has no equivalent in the superalloy market and is, of course, not represented in the Thermo-Calc databases. For this reason, initial basic simulations were carried out to verify preliminary experimental results, with the strategy of moving toward more complex simulations if a match was found between the Thermo-Calc predictions and the laboratory data.
Using the "single-axis equilibrium" simulation, it is possible to determine the relative fraction of each phase as a function of temperature, as well as the corresponding chemical composition of each phase. In this work, this method was applied to identify the heat-treatment window, defined as the temperature range between the onset of liquid phase formation and the precipitation of the $\gamma'$ phase, or of any other undesired phase.
To predict the variability of the material's behaviour within the specified chemistry tolerance window, the initial strategy was to simulate three cases: the target composition, the limit case where all elements are at the lower bound of the specification, and the limit case where all elements are at the upper bound.
This approach aimed to determining the temperature window for the solution stage of the heat treatment.
Thermo-Calc also offers the possibility to simulate the solidification process according to Scheil's theory. This model describes the non-equilibrium solidification of alloys under the assumptions of:

- No diffusion of solute in the solid phase after it forms.
- Complete mixing of solute in the remaining liquid phase.
- Local equilibrium at the solid–liquid interface.

Under these conditions, segregation effects become more pronounced, as solute elements tend to concentrate in the last liquid to solidify. Scheil simulations are particularly useful for predicting micro segregation patterns, identifying the onset of low-melting phases, and estimating the solidification range.
Since our case study involves an PBF-LB process with rapid solidification, it is more appropriate to use the Thermo-Calc option "Scheil with Solute Trapping." In this model, only one primary solid phase is assumed to form dendrites—this is not necessarily the

first phase to solidify. Solute trapping occurs exclusively in this primary phase, driven by the high solidification rate, while all other solid phases form with equilibrium compositions according to the classical Scheil model.
Key characteristics of this approach include:

- The amounts of all solid phases depend on both the extent of solute trapping and the solidification speed.
- The dynamic liquidus of the primary phase varies with solute trapping and solidification rate.
- The dynamic solidus corresponds to complete solidification of the alloy.

The core assumption is that the primary dendrite-forming phase experiences solute trapping due to rapid interface motion, and that this phenomenon also indirectly influences the composition and amount of any other phases formed during solidification. This makes the model well-suited for simulating micro segregation and phase formation in laser powder bed fusion and other high-cooling-rate additive manufacturing processes, where classical equilibrium or Scheil predictions tend to overestimate segregation [13].

## 1.3 Metal Additive Manufacturing

Metal Additive Manufacturing (AM) refers to a group of layer-wise fabrication techniques in which metallic components are built directly from a digital 3D model. Unlike conventional subtractive or formative methods such as casting or machining, AM allows the production of highly complex geometries, internal channels, lattice structures, and functionally graded materials that are otherwise challenging or impossible to fabricate. The layer-wise approach also enables significant material savings and shortened product development cycles, making AM particularly attractive for high-value sectors such as aerospace, energy, and biomedical applications [14, 15].

Despite these advantages, AM of metals presents unique challenges. The rapid solidification rates, often exceeding $10^5$–$10^6$ K/s, generate strong thermal gradients that produce distinctive microstructures, including cellular dendrites, columnar grains, high dislocation densities, and segregation of alloying elements. These features can result in anisotropic mechanical properties, residual stresses, and localized defects such as porosity, lack of fusion, or keyhole voids. Consequently, post-processing treatments such as hot isostatic pressing (HIP), heat treatments, surface finishing, and sometimes hot forging are required to improve density, relieve stresses, homogenize the microstructure, and optimize mechanical performance [14, 16].

Recent research has emphasized the need for AM-specific post-processing strategies, as conventional heat treatments designed for cast or wrought alloys do not always produce optimal microstructures in AM components. Tailored thermal cycles are required to

achieve the desired balance of strength, ductility, and creep resistance while addressing the unique features of the as-built material [14, 15];

### 1.3.1 Laser Beam Powder Bed Fusion

Laser Beam Powder Bed Fusion (LB-PBF) is one of the most widely used metal AM processes. In LB-PBF, a thin layer of metal powder is spread on a build platform. This step, for high-volume production is done automatically by the machine, while in R&D environment, as for the SAM, this step is done manually and takes up to four hours, exposing the powder to the atmosphere. The operator needs special equipment and in Figure1.1 it is possible to see this peculiar setup.

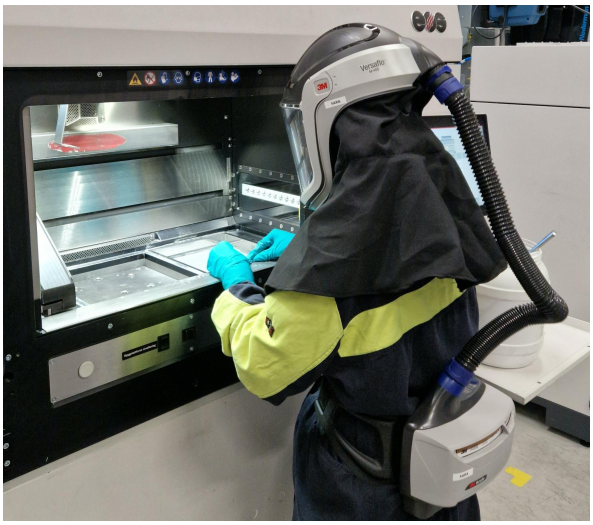

Figure 1.1: Manual charge of the powder inside the EOS M 290

A high-power laser selectively melts regions according to the cross-section of the part defined by a CAD model. After solidification, the platform is lowered, a new powder layer is applied, and the process repeats until the part is fully built [17, 15]; schematic illustration of the process is provided in Figure1.2 .

The extreme cooling rates and steep thermal gradients associated with LB-PBF lead to unique microstructural characteristics. Fine cellular dendritic structures, high dislocation densities, and strong crystallographic textures are commonly observed. The rapid solidification also causes micro-segregation of alloying elements, resulting in supersaturated solid solutions and non-equilibrium phases that differ significantly from cast or wrought analogues [14, 17]. These features can enhance yield and tensile strength but often produce anisotropy in mechanical properties and may reduce ductility.

Process parameters such as laser power, scan speed, hatch spacing, layer thickness, and build orientation have a direct influence on the resulting microstructure, defect formation, and residual stresses. Optimization of these parameters is essential to minimize porosity and achieve uniform properties. Furthermore, post-processing treatments, including HIP, stress-relief annealing, and tailored aging schedules, are often required to

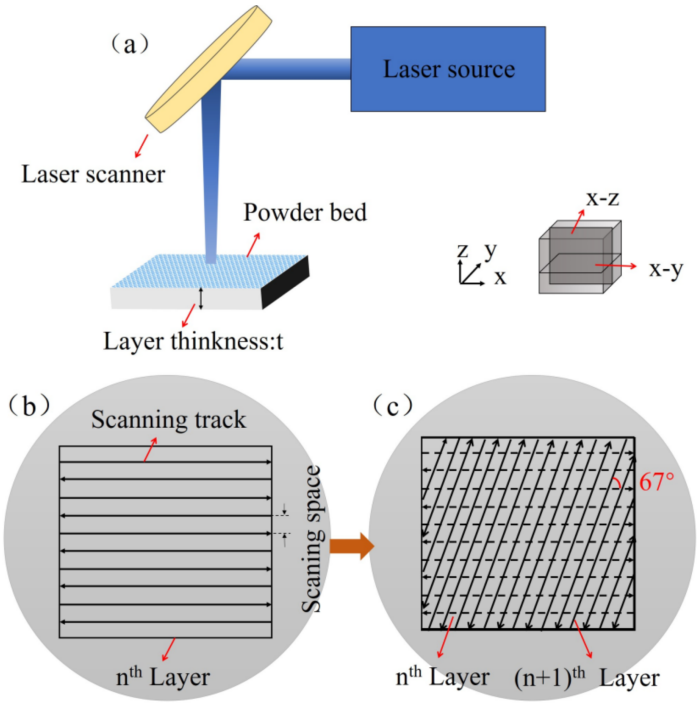


Figure 1.2: (a) Schematic diagram of the LBPBF process (b) laser scanning tracks on the nth layer and (c) laser scanning tracks on the nth layer and (n + 1)th layer [18].

densify the material, reduce residual stresses, and precipitate the desired strengthening phases [16, 17].
However, the layer-wise fabrication and rapid solidification impose significant challenges in predicting microstructural evolution, which has motivated the development of computational models and in-situ monitoring techniques to ensure repeatability and reliability of AM components [14, 16].

## 1.4 Heat treatment of Additive Manufactured Ni-based superalloys

Heat treatment of additively manufactured (AM) Ni-based superalloys is critical to recover the as-built microstructure, which is characterized by high residual stresses, cellular dendritic substructures, microsegregation, and process-induced porosity, into a microstructure comparable to or superior to conventionally processed alloys [19, 20]. Especially for nickel-base superalloys, heat treatment procedures developed for conventional processing routes such as casting or hot rolling cannot be directly transferred to additively manufactured (AM) parts. In fact, AM microstructures are characterized by features such as fine cellular dendrites, chemical microsegregation, high dislocation density, and significant residual stresses, which differ substantially from the relatively homogeneous microstructures obtained by traditional processing. As a result, AM alloys respond differently to standard solution and aging treatments. For example, while conventional heat treatments are primarily designed to optimize the $\gamma/\gamma'$ microstruc-

ture, in AM components they must also relieve residual stresses, promote recrystallization, and dissolve the cellular substructure before controlled precipitation can occur [21, 22]. Tailored post-processing strategies such as hot isostatic pressing (HIP), modified solution treatments, and adjusted aging steps are therefore necessary to achieve microstructural and mechanical properties comparable to those of conventionally processed superalloys.
The post-processing sequence generally consists of three main steps: hot isostatic pressing (HIP), solution treatment, and aging. HIP is performed at high temperature and pressure to close internal pores and heal lack-of-fusion defects, a step not required for wrought or cast alloys. Solution treatment homogenizes the segregated microstructure and promote the grain growth. Compared to traditional heat treatments, AM alloys often require higher solutioning temperatures or longer durations to achieve sufficient homogenization because of the severe microsegregation from layer-wise solidification [3, 1]. Finally, aging is applied to precipitate the strengthening phases ($\gamma'$, $\gamma''$), but with careful tuning to avoid overaging or possible precipitation of TCP phases. In some alloys, simplified routes have been developed that combine HIP and solution steps into a single cycle, followed by optimized aging [20].

### 1.4.1 Enhance creep properties

The creep resistance of AM Ni-based superalloys depends strongly on the effectiveness of the post-build heat treatment in stabilizing the microstructure. Precipitates such as $\gamma'$ and $\gamma''$ provide the primary strengthening mechanism, and their distribution and stability are sensitive to the applied thermal cycle. HIP treatment reduces porosity, thereby minimizing void nucleation sites during creep. Homogenization suppresses brittle secondary phases such as Laves and $\delta$, ensuring that Nb and other solutes are available for $\gamma''$ precipitation, which is essential for long-term creep performance [19, 3].

#### 1.4.1.1 Recrystallization and grain growth

Recrystallization during heat treatment is a key phenomenon in additively manufactured (AM) Ni-based superalloys, as it relieves the high dislocation density and internal stresses introduced during the rapid solidification and thermal cycling of the AM process. Several studies have established that new grain nucleation in the solid state is strongly dependent on the stored strain energy arising from dislocations, defects, and residual stresses. For example, De Terris *et al.* demonstrated that as-built L-PBF Inconel 625 specimens exhibit a very high density of dislocations and cellular substructures, which provide the driving force for recrystallization during post-processing heat treatments[23]. Similarly, a recent study reveals that the as-built condition commonly contains dislocation networks, microsegregation, and cellular structures, all of which contribute significant stored energy that promotes recrystallization once sufficient atomic mobility is provided by thermal exposure[24]. The beneficial effects of recrystallization include the removal of internal stresses, the reduction of anisotropy associated with columnar microstructures, and an overall enhancement of ductility and creep resistance through stabilization of the grain structure. However, excessive re-

crystallization or uncontrolled grain growth can be detrimental. Fine, equiaxed grains improve tensile ductility but tend to promote grain boundary sliding at elevated temperatures, which reduces creep strength. Conversely, very coarse grains suppress grain boundary sliding and enhance creep resistance, but this may come at the expense of toughness. As shown by Venkiteswaran [25], the minimum creep strain rate decreases significantly with increasing grain size at 700 °C, underlining the importance of optimizing grain dimensions for high-temperature service (Fig. 1.3). Therefore, an optimal balance is required: sufficient recrystallization to eliminate columnar substructures and residual stresses, but controlled grain growth to preserve creep strength while retaining adequate ductility. In practice, this balance is often achieved through the combined use of grain boundary pinning particles (e.g. carbides or borides) and carefully tailored heat treatment schedules.

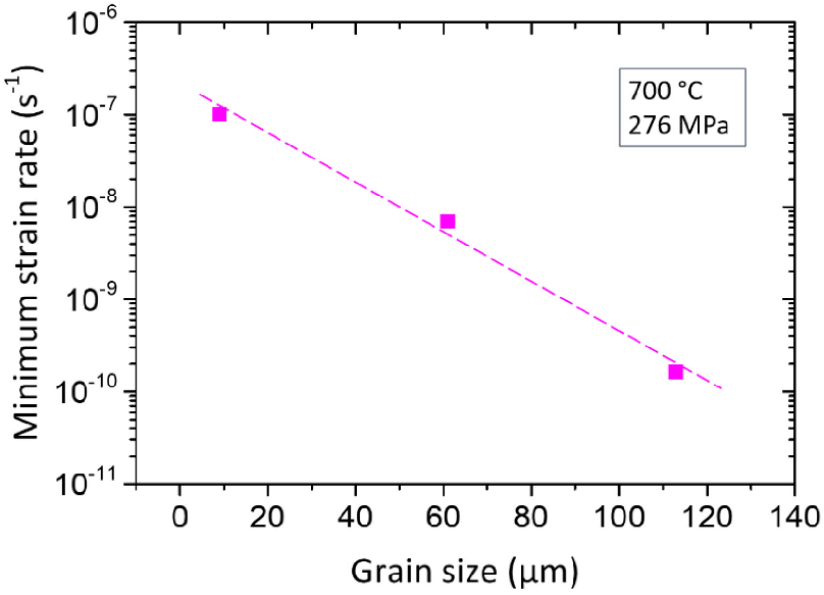


Figure 1.3: Dependence of minimum creep strain rate on grain size at 700 °C and 276 MPa, adapted from Venkiteswaran and Taplin [25].

#### 1.4.1.2 Grain Boundaries Serration

Grain boundary serrations are a recurrent feature in nickel-based superalloys and have been extensively studied because of their strong impact on high-temperature properties. The morphology of the grain boundaries influences grain boundary sliding, the propagation of cracks, and the overall resistance to creep, making the control of serrations an important design parameter in advanced alloys.
In additively manufactured alloys, Haack [26] demonstrated that the development of serrated boundaries in Haynes230 is not only composition-dependent but also strongly related to the complex thermal cycles inherent to the process. The repeated heating and cooling characteristic of additive manufacturing promote perturbations at grain boundaries that facilitate serration formation, suggesting that processing conditions are as influential as alloy chemistry.

Tang [27], focusing on Inconel 600, examined both the generation mechanisms and the mechanical consequences of serrated boundaries. The study revealed that serrations can enhance creep life and resistance to intergranular cracking by redistributing local stresses, although their effectiveness depends on a careful balance between boundary mobility and cohesion.

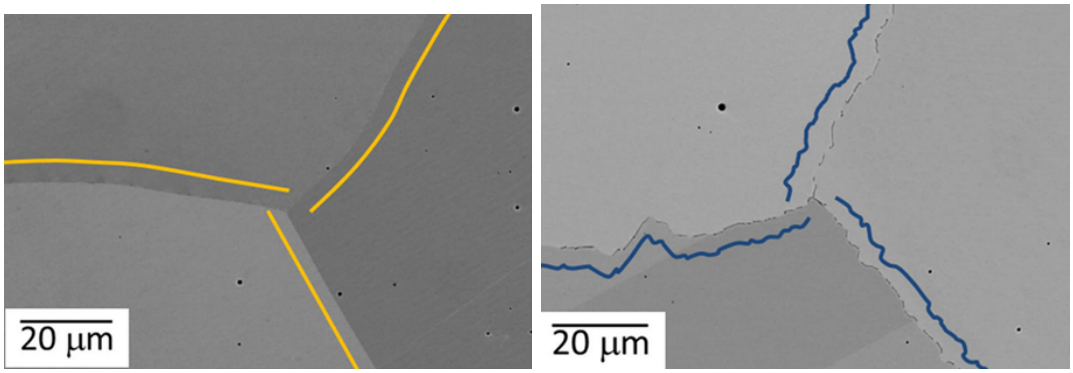


Figure 1.4: Comparison between (left) straight grain boundary and (right) serrated grain boundary in Inconel 600, adapted from Tang [27].

More recently, Tian *et al.* [28] investigated the formation mechanism of serrated grain boundaries in a high-performance powder metallurgy Ni-based superalloy (GH4742 ). Their study highlighted the key role of $\gamma'$ precipitate morphology at the grain boundary: coarse and fan-like $\gamma'$ promoted high-amplitude serrations (mechanism proposed by authors is illustrated in Figure1.5), whereas finer and more dispersed $\gamma'$ precipitates (obtained under faster cooling rates) led to lower-amplitude serrations. This work demonstrates that boundary serration is not only influenced by chemistry and thermal history, but also by the scale and distribution of $\gamma'$ at the grain boundary.

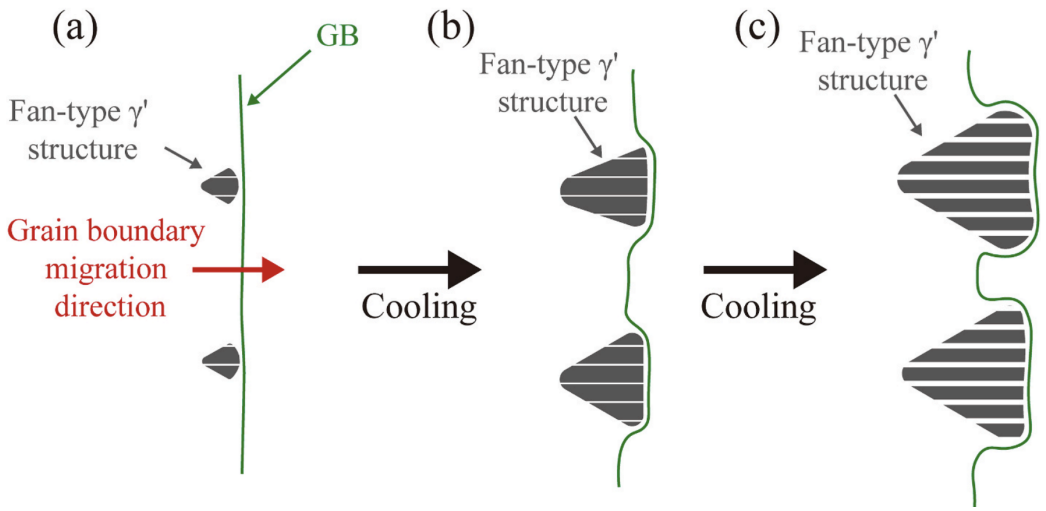


Figure 1.5: Relationship between fan-like gamma prime precipitation and grain boundaries serration [28].

Taken together, these studies indicate that grain boundary serration is a complex phenomenon governed by alloying, $\gamma'$ morphology, processing conditions, and service environment. Understanding their interplay is essential for designing Ni-based superalloys with superior creep resistance and microstructural stability at elevated temperatures.

# Chapter 2

# Materials and methodology

## 2.1 Initial status and work strategy

The SAM alloy project, at the start date of March 2025, had reached the important milestone of demonstrating the material's printability, without extensive defects such as hot cracking during printing (related to the thermal input) or strain age cracking (SAC), which occurs during the first heat treatment step after building the component. However, the mere survival of the samples after the heat treatment trial is not sufficient. As mentioned in 1.4, it is crucial to tailor a suitable heat treatment for material processed via the PBF technique. The aim of this thesis is to identify an appropriate solution treatment.
To understand the material's behavior and the influence of its chemistry on equilibrium phases and the onset of incipient melting phenomena, a campaign of simulations using ThermoCalc software was conducted, which also aided in setting up the Design of Experiments (DoE) for the solution trials.
The approach is to first understand the material's high-temperature behavior, which requires "freezing" the microstructure by air quenching after soaking in a furnace for a fixed time. The material used for the solution trials is in the as-built condition, not HIPed. This choice was made for two reasons: the limited availability of HIPed samples and the fact that pressure has no effect on recrystallization and grain growth [29]. All solution trials will be characterized to establish relationships between processing temperature and material properties, with particular focus on recrystallization, carbide precipitation, and grain boundary morphology.

## 2.2 SAM alloy – preliminary heat treatment

The material object of this work of thesis is nickel based superalloy SAM®, provided by Siemens Energy AB. The powder was produced and characterized by VDM Metals; the chemical composition of the analyzed samples is found to be inside the request window but is not possible to provide detail on the exact values.
The SAM cubes and cylinders used for the experimental part are produced by Siemens

Energy AB by means of PBF-LB through EOS M290, the printing parameters are reported in Table 2.1; scanning strategy and influence of printing paramenters is not investigated in this thesis work.
The preliminary heat treatment, set as a standard, was performed by PresX (Reggio Emilia, Italy), and the parameters are reported in Table 2.1. The material, after these treatment can be considered the *initial status*, as starting point to understand what can be improved for the SAM alloy.

Table 2.1: Process parameters to print the SAM alloy.

| **Laser power (W)** | **Scan speed (mm/s)** | **Layer thickness (mm)** | **Hatch spacing (mm)** | **Volumetric Energy Density ($J/mm^3$)** |
|---|---|---|---|---|
| 195 | 1200 | 0.04 | 0.06 | 67.71 |

Table 2.2: Preliminary Heat treatment steps for the alloy.

| Step | **Temperature (ºC)** | **Pressure** | **Time (hours)** | **Heating rate* (ºC/min)** | **Cooling rate* (ºC/min)** |
|---|---|---|---|---|---|
| HIP | 1180 | 100 MPa (Argon) | 4 | 3–10 | $< 10$ |
| Solution | 1170 | Vacuum | 4 | 15–30 | 20/40 |
| Aging | 1000 | Vacuum | 4 | 15–30 | 20/40 |

** The values of heating and cooling rate for all the steps are reported by PresX as range and no raw data are provided for a detailed evaluation.*

## 2.3 Materials for comparison: IN939-IN738-STAL-15

Siemens Energy provided samples of three different superalloys that can be considered competitors of the SAM. These alloys—Inconel 939, Inconel 738, and STAL-15—were used as reference materials for comparison in the hardness tests (HV10). Each alloy was supplied in both the as-built and heat-treated conditions. Although the specific parameters of the additive manufacturing process and subsequent heat treatments were not disclosed, they are to be considered fully optimized for all three alloys.

## 2.4 Tensile test

Tensile tests were carried out in accordance with ISO 6892-1 using a Schenck Trebel RSA100 testing machine, equipped with a Schenck Trebel 100 kN load cell. Test specimens were obtained by machining both the as-built (AB) material and the fully heat-treated (FHT; HIP + solution + aging) condition. For each condition, samples were prepared with orientations of 0° and 90° with respect to the build direction.
According to the reference standard, a minimum of three specimens should be tested for each case (AB–0°, AB–90°, FHT–0°, FHT–90°). However, due to lack of material, only a single specimen per case could be tested. Consequently, no statistical analysis or error estimation could be performed, and the results presented should be considered as indicative trends rather than statistically validated values.

The mechanical properties extracted from the tests include the ultimate tensile strength (UTS), the 0.2% proof strength (Rp0.2%), strain, and the elastic modulus ($E$), the latter evaluated from the linear region of the stress–strain curve between 30% and 70% of Rp0.2%.

## 2.5 Hardness test – HV10

The hardness test was performed according to ASTM – E18 with DuraSacan50-70-80 G5 hardness machine. For each sample, five measurement where performed, with a spacing between imprint of one millimeter. This test was performed to have a rapid overview of the mechanical properties, since tensile test is time and material consuming. There is a direct proportion between the yield strength and the hardness value, so hardness test was performed for all steps of the preliminary heat treatment, and then for all the steps of the . Also, it is noticed that alloys that present lower hardness at the AB state are found to be easier to print, due to a higher ductility at high temperature, so a comparison of hardness at the as built state was performed between SAM, IN939, IN737 and STAL-15.

## 2.6 Metallographic preparation

The provided samples were supplied in the form of either cubes or cylinders; however, no differences in printing parameters are associated with the two geometries. All specimens were sectioned along the build direction using an automatic saw at a cutting speed of 0.045 mm/s. After the cut the samples are embedded in a conductive resin and then polished, starting from a 500 SiC paper to a CHEM OPS step. A detailed resume of the polishing strategy is reported in Table 2.3, with paper, suspension, rpm and time. Note: the last step of fine polishing was done with Chem OPS suspension, that provide a slight etching and give a better contrast of grain boundaries during analysis with electron microscope, but for the analysis with the optical one the polishing was stopped at the previous step.

Table 2.3: Polishing steps and parameters.

| Step | Suspension | Lubricant | Time (min) |
|---|---|---|---|
| SiC foil-120 | / | water | 1 |
| SiC foil-500 | / | water | 1 |
| Largo | DiaP. All/Lar.9 | / | 3 |
| Floc | DiaP. Floc3 | / | 3 |
| Nap | DiaP.Nap-B1 | / | 3 |
| Nap | DiaP.Nap1/4 | / | 4 |
| Chem | OP-S | / | 1 |

## 2.7 Optical Microscopy

The optical microscope was employed, at first to characterize the as built material and detect defects. That was essential to verify that the HIP step in the preliminary heat treatment resulted in an almost defect-free material, or at least in a defect density acceptable according to Siemens Energy's internal standards. This was necessary since the solution heat treatment trials will be performed on as built sample. The model of optical microscope used is the Nikon EclipseLV150N.

## 2.8 Electron Microscopy and Energy Dispersive X-Ray Spectroscopy

After the final polishing step using CHEM OPS, the samples were examined with a Zeiss GEMINI 450 scanning electron microscope equipped with EDS Oxford Instruments X-Max or Thermo Fisher Noran systems detectors. Images were acquired in both secondary electron (SE) and backscattered electron (BSE or AsB as labelled in the pictures) modes to highlight the surface morphology and the phase changes of the material, respectively. Magnifications ranged from 1 Kx, to provide an overview of the material, through 5 Kx ,10 Kx ,and 30 Kx ,up to 100 Kx when a detailed examination of the $\gamma'$ (gamma prime) morphology was required. To obtain an overview of the chemical composition of the different phases, an EDS (Energy-Dispersive X-ray Spectroscopy) detector was employed.

## 2.9 Electron Backscatter Diffraction

Electron Backscatter Diffraction (EBSD) is a scanning electron microscopy (SEM)–based technique that enables quantitative crystallographic characterization at the microscale. It relies on the formation of diffraction patterns (Kikuchi patterns) from a tilted crystalline sample when irradiated by a focused electron beam.
When the electron beam impinges on the surface of a tilted crystalline sample—at an angle of 70°—the electrons are incoherently and quasi-elastically scattered in all directions from a small, point-like interaction volume within the crystal (on the order of tens of nanometres, which determines the spatial resolution of the technique). Some of these backscattered electrons strike sets of atomic lattice planes at angles that satisfy the Bragg condition:

$$n\lambda = 2d\sin\theta$$

where n is the diffraction order, $\lambda$the electron wavelength, d the interplanar spacing, and $\theta$ the Bragg angle. For each diffracting lattice plane, electrons are scattered into a pair of large-angle cones. The intersection of these cones with the EBSD detector's phosphor screen produces bright Kikuchi bands, each corresponding to a specific family of planes. The intensity of each band depends on the atomic scattering factors of the atoms in the unit cell and the relative geometry of the diffracting planes. While the complete description of band profiles involves complex many-beam dynamical simulations, a simpler kinematical model—using structure factor calculations—remains sufficient for routine indexing. In standard EBSD workflows, the positions of Kikuchi bands are identified using the Hough transform, and only planes with intensities above a set threshold are included in the indexing process.
EBSD provides a detailed two-dimensional mapping of grain orientation, phase distribution, and crystallographic texture, with a spatial resolution that ranges from 10 to 200 nm and a precision of orientation measurement of 0.05 to 0.1° . From the collected data, it is possible to extract grain size statistics, misorientation distributions, boundary character information, and pole figures. Since EBSD patterns originate from only a few tens of nanometres below the surface, high-quality sample preparation is critical. Measurements were conducted using a Zeiss GEMINI 450 SEM equipped with the EBSD detector Symmetry 2. The sample was tilted to 70°, and acquisition parameters were optimized for pattern clarity (accelerating voltage  20 kV, working distance 15 mm, beam current adjusted to maximize signal  6.2 pA). Post-processing involved noise reduction, refinement of orientation data, and the extraction of microstructural parameters relevant to the studied alloy (done automatically by the software).
Through this methodology, EBSD provided high-fidelity crystallographic data, enabling the possibility to trace the grains evolution through the different temperatures of the solution heat treatment trials.

## 2.10 Gamma prime volume fraction evaluation

The standard method for measuring the volume fraction of a reinforcing phase such as $\gamma'$ in Ni-based superalloys is described in ASTM E562-08 (grid method). However, it is generally reported that this approach tends to overestimate the actual phase fraction. To evaluate the possible error associated with the standard method, a comparison was carried out with the results obtained through image analysis using ImageJ software. Micrographs were acquired with the BSE detector and subsequently processed in ImageJ. Each image (Figure 2.1 as example) was first converted to 8-bit, after which the threshold was adjusted to selectively highlight the $\gamma'$ phase. In cases where carbides were present, masks were applied over them, as their higher brightness compared to $\gamma'$ in BSE images made threshold adjustment more challenging. Once the images were converted to binary, additional processing steps were applied: the “Fill Holes” function was used to ensure that each $\gamma'$ particle was represented as a solid feature, while the “Watershed” function was employed to separate touching particles (occasionally supported by manual corrections). Finally, the "Analyse Particles" function provided quantitative data for each detected feature, including particle size and morphology, as well as the total area fraction, which was taken as the volume fraction of the $\gamma'$ phase; Figure 2.2.

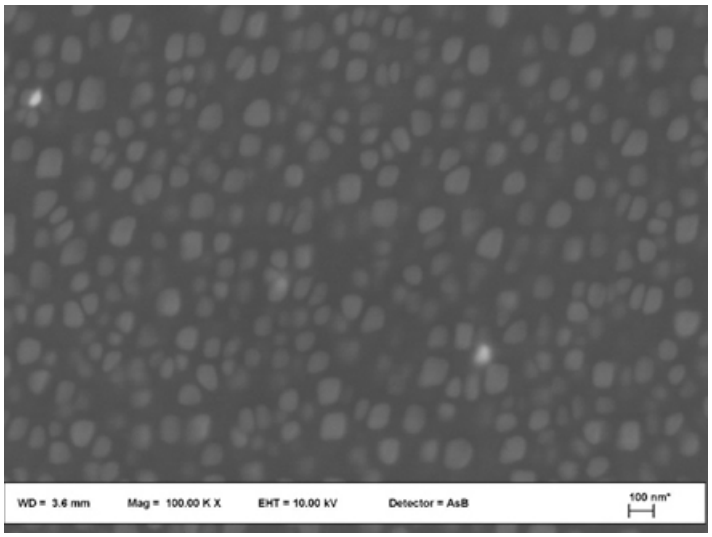


Figure 2.1: Example of BSE image for gamma prime evaluation.

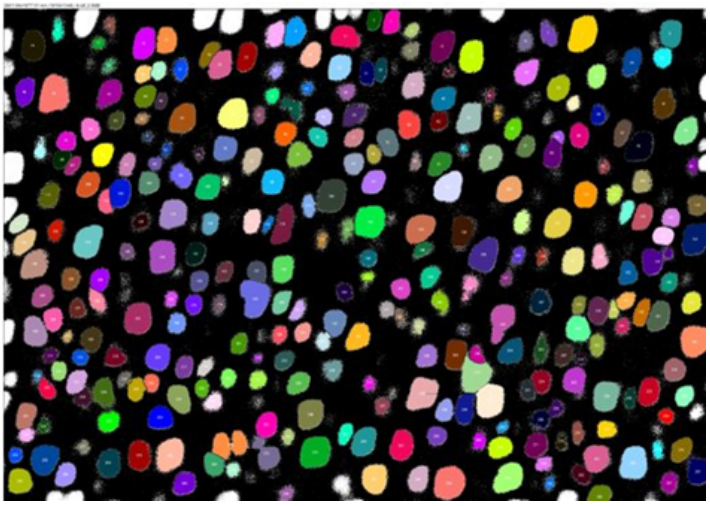

Figure 2.2: Example of result after using analyse particle tool on ImageJ.

## 2.11 Differential Scanning Calorimetry

Differential Scanning Calorimetry (DSC) is a technique that measures the difference in heat flow between a sample and an inert reference when both are subjected to a controlled heating or cooling program. The resulting curve allows the identification of thermal events such as phase transformations, precipitation, and dissolution phenomena. In superalloys, DSC is particularly valuable for detecting the dissolution of strengthening phases ($\gamma'$ and carbides), the precipitation of secondary phases, recovery or recrystallization events, and the onset of melting. In the DSC trace, endothermic peaks correspond to phase dissolution or melting, while exothermic peaks are associated with precipitation or ordering reactions. The temperatures at which these transformations occur provide useful reference points for the optimization of solution and aging heat treatments. In the present work, DSC analysis was performed on the as-built material of the SAM superalloy, with the aim of identifying its characteristic transformation temperatures and providing baseline data for the design of subsequent heat-treatment cycles. This test was performed by Professor Emilio Bassini inside Polytechnic of Turin's facility. Both the heating and cooling steps were performed changing the rate in the region close to the expected temperatures of the main thermodynamic events, with the goal of having precise values. It is noticed, in literature, that there is a strong influence of the heating rate on the result of a DSC test for different superalloys, and this is mainly related to micro-segregation phenomena, that can be eliminated with slow heating rate.

## 2.12 Setup for the solution heat treatment

The solution heat treatment was carried out in the laboratories of Siemens Energy using a muffle furnace model LT 9/14-Nabertherm , a high-temperature resistance furnace without a controlled atmosphere chamber or an integrated rapid cooling unit. The specimens consisted of small cylinders with a diameter of 15 mm and an approximate length of 25 mm. The purpose of this treatment was to investigate the microstructural evolution with the changing of the temperature and subsequently "freeze" the microstructure by applying a rapid air quench directly from the solution temperature. After placing the samples inside the furnace, heating was performed to the target temperature, followed by a soaking period of four hours, consistent with the preliminary heat-treatment procedure. At the end of the holding stage, the furnace was opened and the operator manually removed the specimens, which were placed on a perforated steel sheet to promote airflow. An additional air convection tube was positioned above the samples to further accelerate cooling. The furnace can provide temperature monitoring during heating and soaking; however, no direct information on the actual cooling rate of the specimens was available in this way. To address this limitation, each test sample was bonded with platinum wire (inert at the treatment temperature) to a dummy specimen in which a hole had been drilled to insert a type N thermocouple. This configuration allowed continuous recording of the temperature profile both inside and outside the furnace during the heating and then cooling step. The type N thermocouple was selected due to its excellent stability, reduced drift, and high resistance to oxidation, making it particularly suitable for high-temperature applications up to 1300 °C. The thermocouple was positioned at the centre of the dummy sample to provide the most accurate measurement of the cooling history, which would not have been possible if the thermocouple had been simply attached to the surface of the test specimens. To better understand the set up of the heat treatment a resume is provided in Figure 2.3.

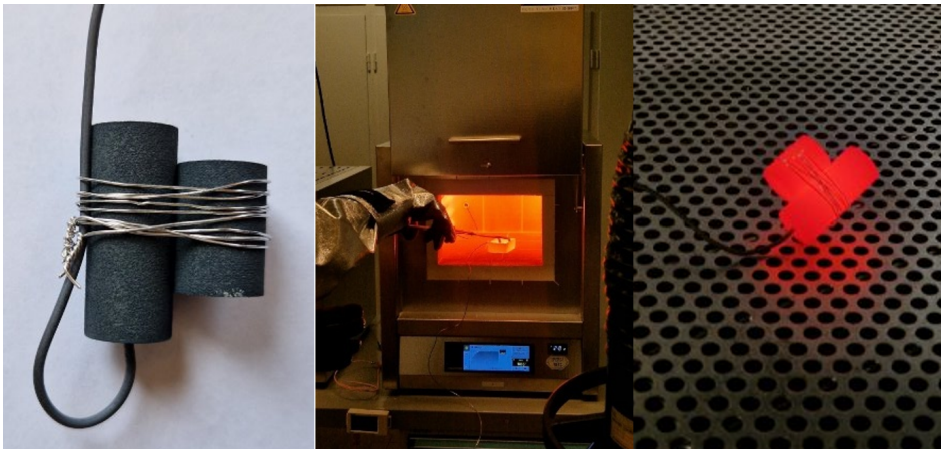

Figure 2.3: Setup of the solution HT, from left to right: sample bonded to the dummy one used for reference with Pt wire, frame of the removal of the sample after the soaking and the cooling on a pre-forated grid.

# Chapter 3

# Results and discussion

## 3.1 ThermoCalc simulations: Chemistry influence on HT window

The first set of results is about the outcome of the ThermoCalc simulations, which aimed to predict the variability of the material's behavior within the specified chemistry tolerance window. The initial strategy was to simulate three cases: the target composition, the limit case where all elements are at the lower bound of the specification, and the limit case where all elements are at the upper bound. This approach aimed at determining the temperature window for the solution stage of the heat treatment, considered as the range between the solvus of the gamma prime phase, or any other undesired phase like the TCP, and the presence of incipient melting phenomena. The results of these simulation are presented in Table3.1, where are reported: the volume fraction of the gamma prime phase, volume fraction of carbides, solvus temperature of gamma prime, formation temperature of the liquid phase, solvus temperature of ETA phase, and lastly it is possible to predict a possible window for the heat treatment. The experimental part of the thesis was performed with a particular powder lot, and its chemistry was also simulated to have a better comparison between the laboratory results and the thermodynamic simulations, result is showed in 3.2.

The results indicate that the $\gamma'$ volume fraction remains constant, whereas the $\gamma'$ solvus temperature increases and the liquidus temperature decreases when moving from the lower to the upper limit of the alloying elements. For the specific powder lot under consideration, all elemental concentrations fall within the specified range. Consequently, the software predicts a material behavior comparable to that of the target composition.

At the start of the project the only tool available to create a Doe (Design of Experiment) for the solution heat treatment step was ThermoCalc. Based on the results previously mentioned this was the proposed DoE, illustrated in Table3.3.

Table 3.1: ThermoCalc results for lower, target, and upper chemistry conditions.

| **Parameter** | **Lower** | **Target** | **Upper** |
|---|---|---|---|
| $\gamma'$ phase (%) | $\sim 38$ | $\sim 40$ | $\sim 39$ |
| Carbides (%) | $\sim 0.11$ | $\sim 0.43$ | $\sim 0.60$ |
| Solvus $\gamma'$ (ºC) | 1041 | 1058 | 1067 |
| Liquidus (ºC) | 1183 | 1167 | 1146 |
| Solvus ETA (ºC) | 1110 | 1130 | 1141 |
| Heat Treatment Window (ºC) | **73** | **37** | **5** |

Table 3.2: ThermoCalc results for powder lot chemistry.

| **Parameter** | **Powder chemistry** |
|---|---|
| $\gamma'$ phase (%) | $\sim 39$ |
| Carbides (%) | $\sim 0.39$ |
| Solvus $\gamma'$ (ºC) | 1057 |
| Liquidus (ºC) | 1171 |
| Solvus ETA (ºC) | 1120 |
| Heat Treatment Window (ºC) | **51** |

Table 3.3: Summary of preliminary heat treatment runs.

| Run | Temp (°C) | Soak time (h) | Expected phases (ThermoCalc) |
|---|---|---|---|
| 1 | 1050 | 4 | Onset $\gamma'$ |
| 2 | 1075 | 4 | $\gamma + \gamma'$ (increase) |
| 3 | 1100 | 4 | $\gamma + \gamma'$ (increase) |
| 4 | 1125 | 4 | Onset $\eta$ |
| 5 | 1150 | 4 | $\gamma + \gamma' + \eta$ |
| 6 | 1175 | 4 | Incipient melting |

### 3.1.1 Effect of Carbon and carbides composition

A second set of simulations was carried out to investigate the effect of carbon on the alloy. In previous work conducted on the material (before the kick off of this thesis project), a low fraction of carbides had been observed, making it necessary to understand whether this was due to a lack of carbon or to a deficiency of carbide-forming elements such as Ta and Hf. These two elements are considered as carbide formers since the Thermo-Calc software predicted a possible carbide composition, as shown in Figure 3.1. An initial presence of HfC carbides is observed around 500 °C; however,

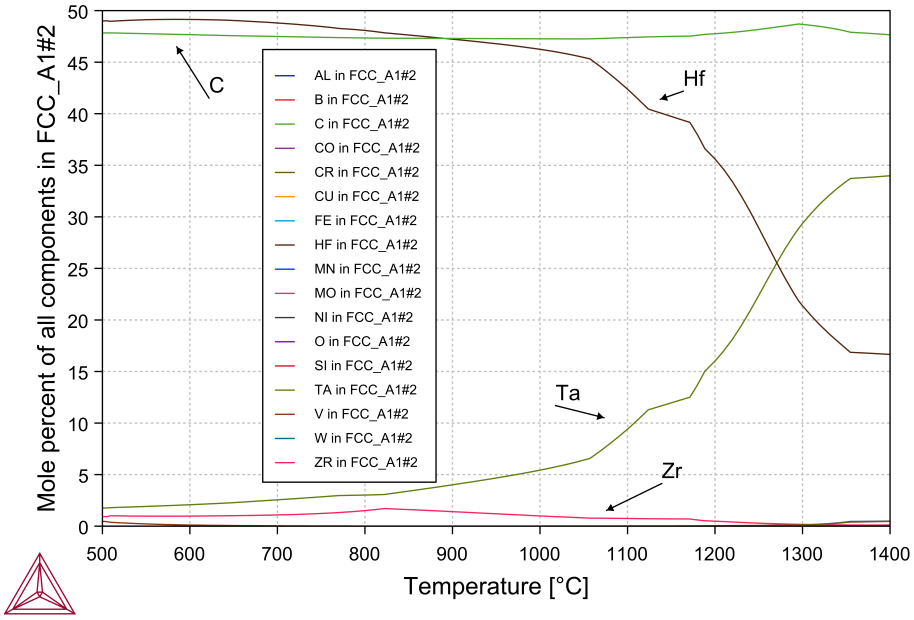


Figure 3.1: MC carbide composition according to ThermoCalc software.

as the temperature increases, there is an increase of TaC respect to HfC, while ZrC is in minority respect to the others. The temperature stability range of these carbides extends beyond the onset of the liquid phase of the SAM alloy, and they remain stable up to about 1300 °C. This behavior is even more evident in Figure 3.2, which shows a magnified view of the SAM composition in the temperature vs. molar fraction diagram. In this figure, the range 0–10% is highlighted to better visualize the phases present in low fractions. As mentioned previously, during the early stages of the design of this novel alloy it was of particular interest to assess whether modifications of the chemical composition could still be beneficial. In particular, the carbon content appeared to be rather low. More precisely, the volume fraction of carbides in the alloy was found to be limited, and therefore insufficient to provide the desired strengthening mechanisms previously discussed, namely the pinning effect and the associated phenomenon of grain boundary serration.
Simulation results showed that increasing only the carbon content leads to a corresponding rise in the carbide fraction. Specifically, a progressive addition of 0.01 vol.% C results in an approximate increase of 0.1 vol.% in carbides. These simulations were performed starting from the target composition of 0.025 vol.% C up to 0.8 vol.% C.

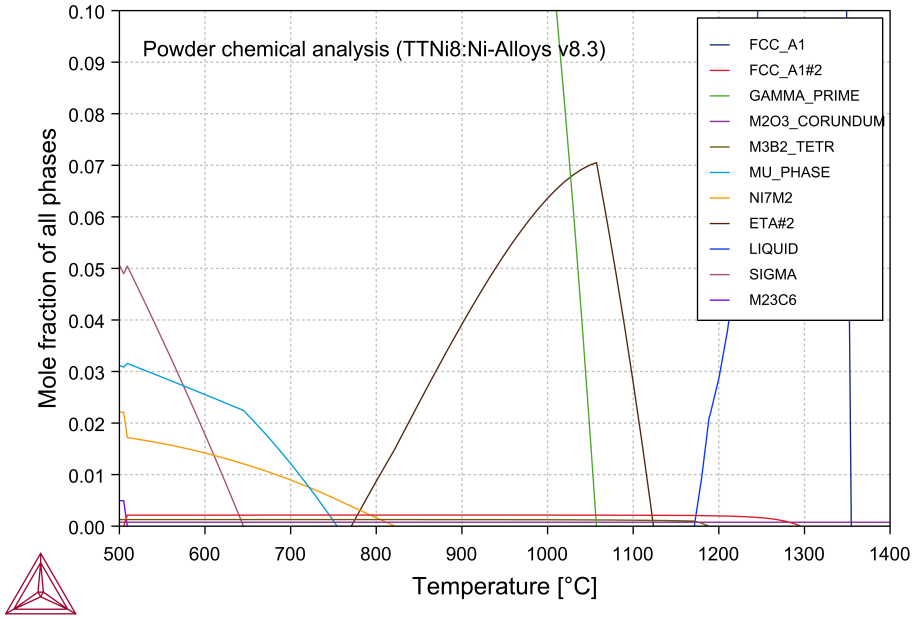


Figure 3.2: Magnification of the 0.1 molar fraction of the SAM alloy according to ThermoCalc software.

Further increases were not considered useful, since an excessive carbon fraction would have detrimental effects on corrosion resistance, which would be unacceptable for the intended application of the alloy.
Figure 3.3 illustrates this behavior, highlighting not only the steady increase in carbide fraction with increasing carbon content, but also the relatively constant stability range of these carbides across the investigated conditions. This observation confirms that the optimization of the carbon level plays a critical role in balancing the beneficial effects of carbides (grain boundary strengthening and pinning) with the need to avoid undesirable drawbacks in terms of corrosion performance.

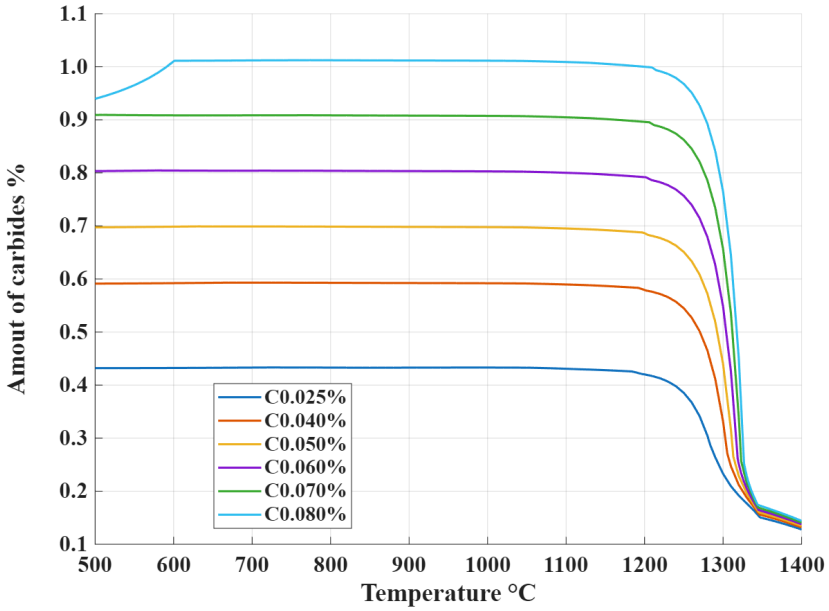


Figure 3.3: Carbides fraction as function of carbon content.

## 3.2 ThermoCalc simulations: Scheil Simulations

Scheil simulations are a powerful tool to predict the temperature range over which an alloy solidifies and to analyze the evolution of the chemical composition of the liquid phase, allowing identification of elements with a higher tendency to segregate. In Figure 3.4, the plot for the full solidification range is shown; from the legend, the co-presence of multiple phases in the solid state can be observed. This occurs because the simulation assumes equilibrium-like constraints. However, the process we are considering—PBF-LB—involves steep thermal gradients and rapid solidification, which drive the system far from equilibrium conditions. Thermo-Calc software allows the simulation of additive manufacturing processes, but for the SAM alloy, the software was unable to provide results due to the limited database available for this simulation. As mentioned previously, Scheil simulations can still be useful to trace the chemical composition of the remaining liquid phase. Typically, the last 15–20% of liquid, according to Scheil theory, represents the fraction that remains interconnected. Figure 3.5 illustrates this behavior, and we can also evaluate the temperature range at which the solidification is completed, around 300°C.

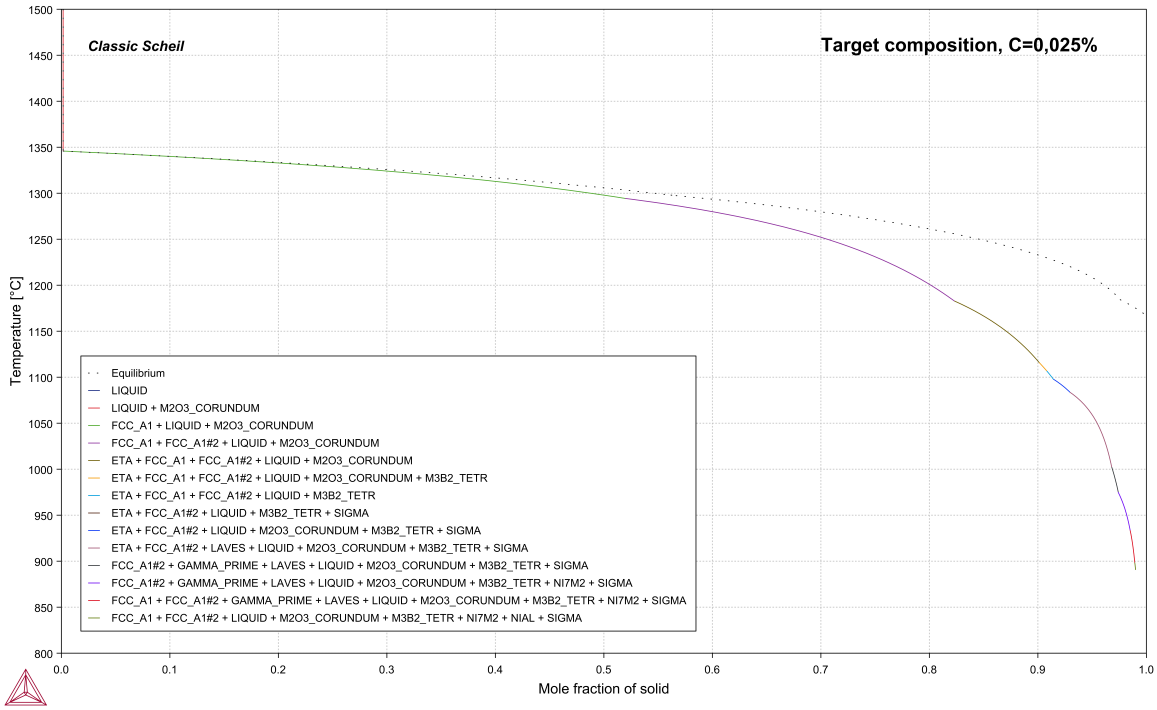


Figure 3.4: Scheil simulation under equilibrium conditions

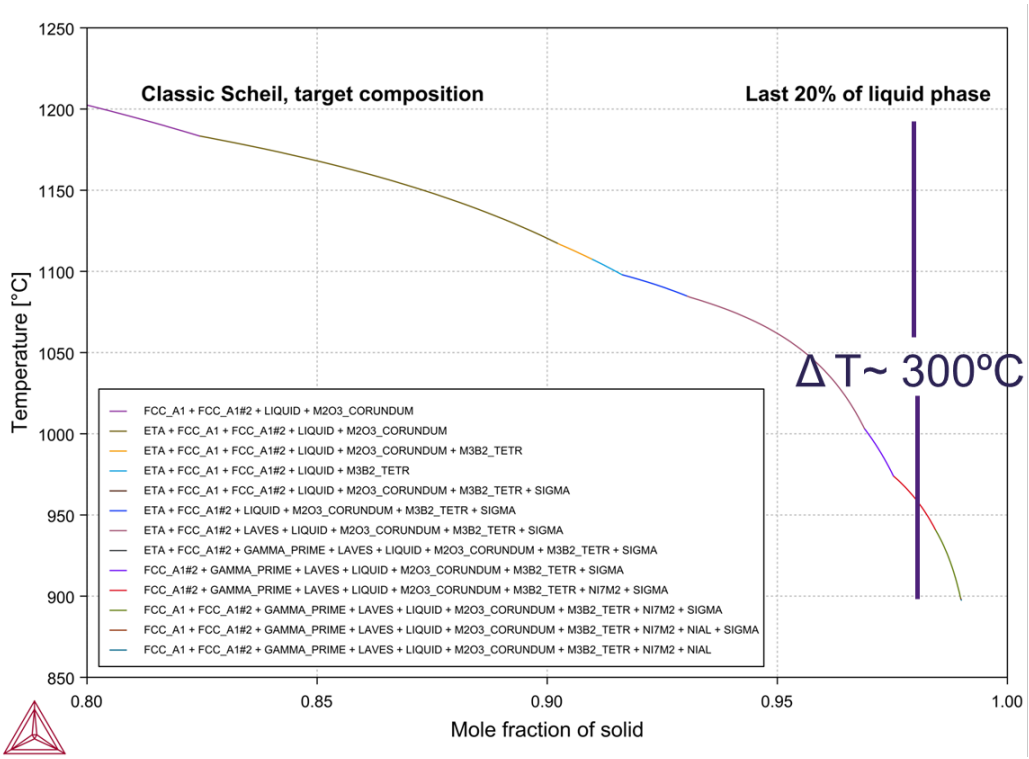


Figure 3.5: Scheil simulation under equilibrium condition, last 20% of liquid phase

## 3.3 Preliminary Heat Treatment characterization

### 3.3.1 As built

The analysis of the XZ plane, parallel to the building direction and observed with an optical microscope, highlighted the presence of residual defects typical — and inevitable — of the PBF process: porosity, liquation cracking, gas porosity and lack of fusion. Figure 3.6 clearly shows porosity and lack of fusion. The largest detected defect has a Feret diameter of 75 $\mu$m, while the total porosity (LOF and gas porosity) is about 0.26%. The average diameter of the porosity is $8.7 \pm 1.8\,\mu$m.

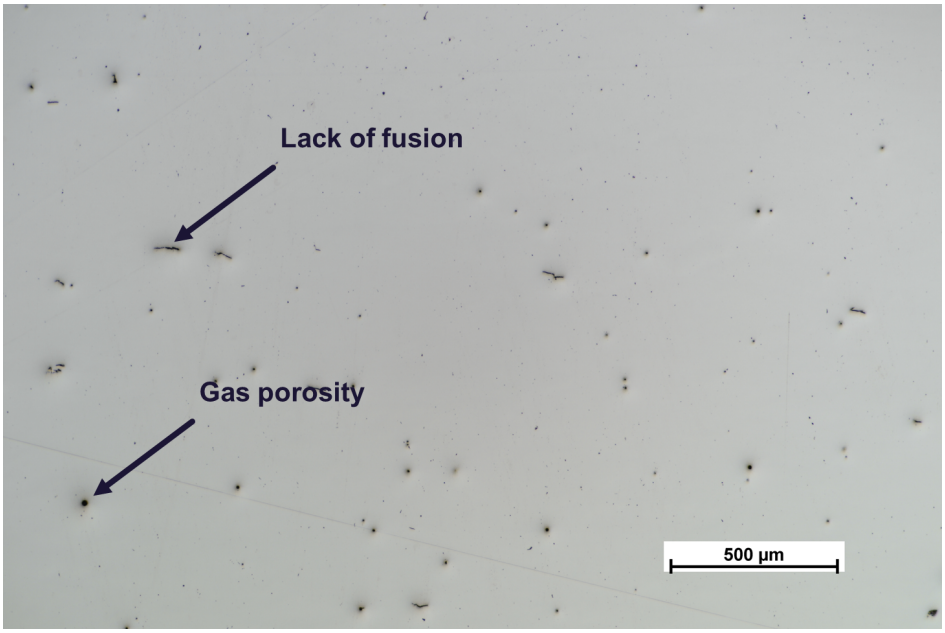


Figure 3.6: LOM image of the as-built sample without etching; residual defects are detected.

A closer examination of the microstructure, as shown in Figure 3.7-A, reveals the presence of primary dendrites; in the image the contrast between the grains and dendrites arises from different crystallographic orientations. The contrast inside the interdendritic region is attributed to the Z-contrast (atomic number contrast, Figure3.7-B), where the bright particles are attributed as MC-type primary carbide, common phase formed during the solidification process. This phase looks enriched mostly of hafnium and tantalum, beside carbon, but at this stage of the analysis it was not possible to provide a reliable EDS mapping because of the really small dimension of the carbide particle. In Figure3.8 is possible to have a closer look of these carbide with higher magnification; their dimension is, as average $114 \pm 54$nm, with biggest particle around 253 nm.
No other phase is evident in this step of the process, no $\gamma'$ or borides are visible. In Figure3.7-C is also visible a particular defect, attributed as *Liquation cracking*, this phenomena mainly depends on the stability of the liquid film of the melt pool and local stress concentration [30].

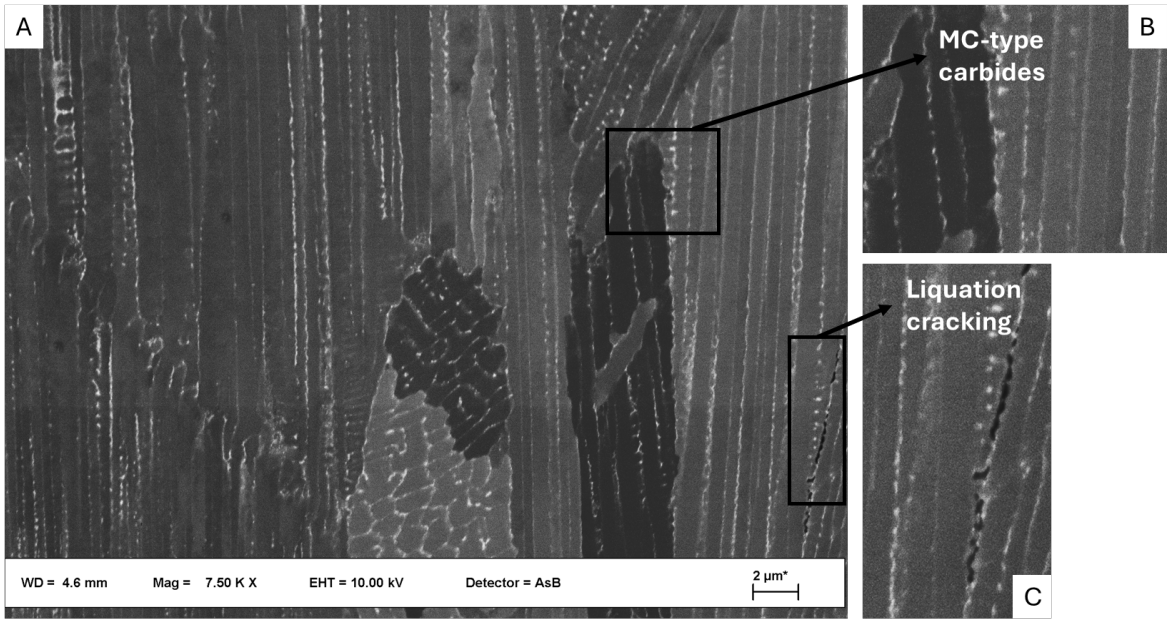


Figure 3.7: BSE micrograph of the as built sample, A-highlight of the cellular microstructure; B-MC-typer carbides in the inter-dendritic regions C-Liquation cracking defect .

Grain size evaluation, performed with EBSD analysis, give us, at first, a better look of the pronounced columnar microstructure orientated along the crystallographic direction, as showed in Figure3.9, where the Inverse Pole Figure (IPF) is reported, again for the plane XZ and in Z direction.
In addition to grain morphology, Kernel Average Misorientation (KAM) maps were analyzed to provide information on the local lattice distortion associated with dislocation length. The as-built condition exhibits an average KAM value of approximately 2.2°, which indicates a high local dislocation density. This observation is consistent with the rapid solidification and residual stresses commonly reported for PBF-LB processed Inconel 718 [31, 32]. Measures based on the fitted ellipse major diameter reveal that approximately 60% of the grains fall within the range 20–50 µm, with larger grains reaching up to 270µm. The aspect ratio, defined as the ratio between the fitted major and minor diameters, indicates that about 65% of the grains lie in the range 2-5, while the remaining grains exhibit higher aspect ratios, up to 16. The distribution of the aspect ratio and the major diameter of the fitted ellipse are represented in Figure3.10
These results suggest a strong tendency toward the formation of fine, elongated columnar grains. This microstructural characteristic is probably driven by epitaxial growth and promoted by the steep thermal gradients characteristic of the PBF-LB process [33, 34].
Table 3.4 provides a resume of the main findings for the as-built condition of the SAM alloy.

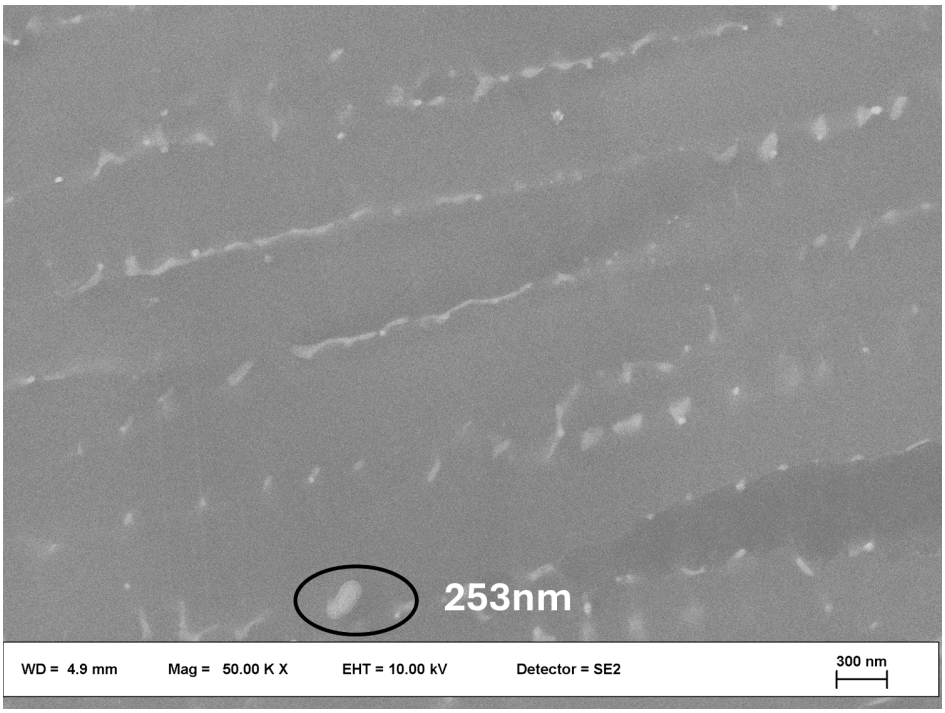


Figure 3.8: BSE image at high magnification; evidence of carbides inside inter-dendritic region in the as built sample.

Table 3.4: Main results after characterization of the as built sample.

| State | % vol porosity | Avg FEMD (nm) | Avg AR | % vol carbides | Carbide type |
|---|---|---|---|---|---|
| As-built | 0.26 | 8.7 | $3.8 \pm 2.2$ | N.A. | MC |

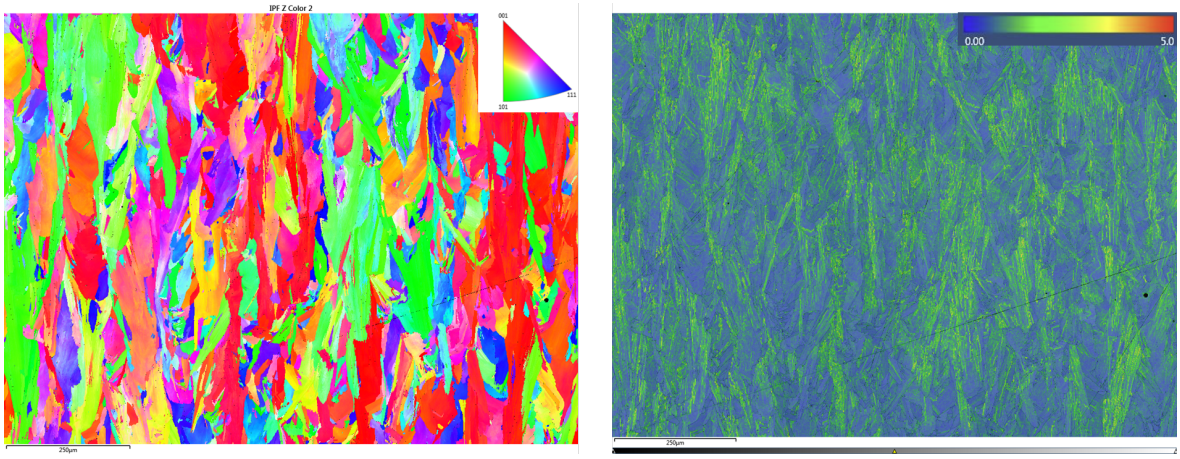


Figure 3.9: Left: EBSD orientation map in IPF representation for the as built sample; IPF along building direction. Right: Kernel Average Misorientation map as additional result of the EBSD mapping.

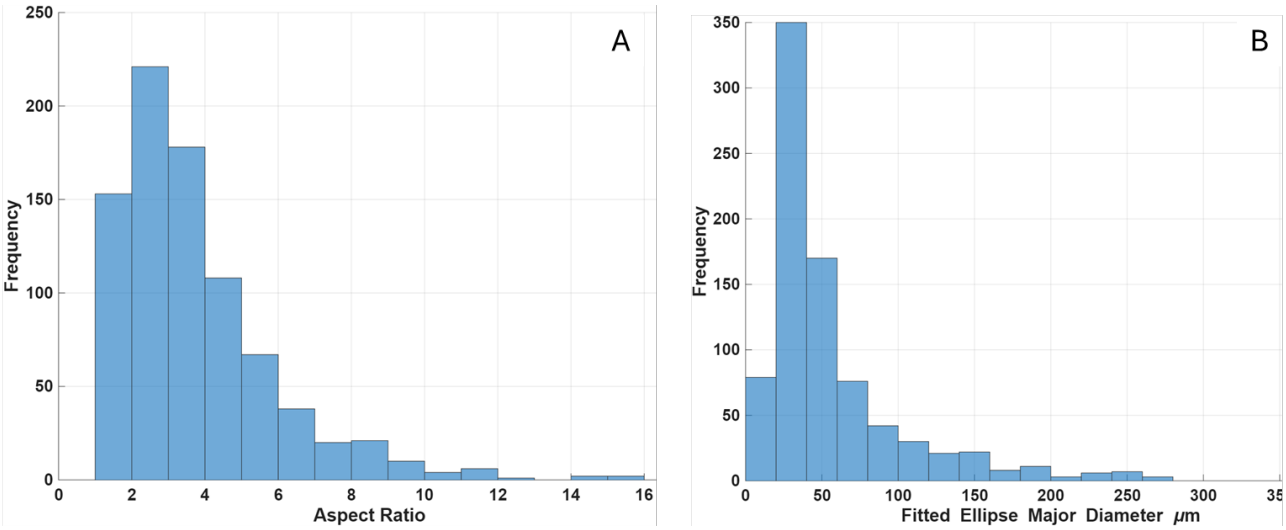


Figure 3.10: A- distribution of the aspect ratio and B- the fitted ellipse major diameter resulting from the EBSD analysis for the as built sample

### 3.3.2 Hot Isostatic Pressing

After the HIP treatment, performed at 1180 °C and 100 MPa for four hours, the microstructure exhibited significant modifications. Optical microscopy revealed that HIP was highly effective in eliminating the defects typical of the as-built condition, resulting in an almost defect-free component.
After etching the surface, further observations with the optical microscope provided important insights into the grain boundary morphology. In Figure 3.11, the coexistence of serrated and straight grain boundaries can be observed. In the case of serrated grain boundaries, a variation in the amplitude of the serrations is noticeable. This statement, however, is qualitative, it was not possible to quantify the serration amplitude, and only a subjective assessment is provided.

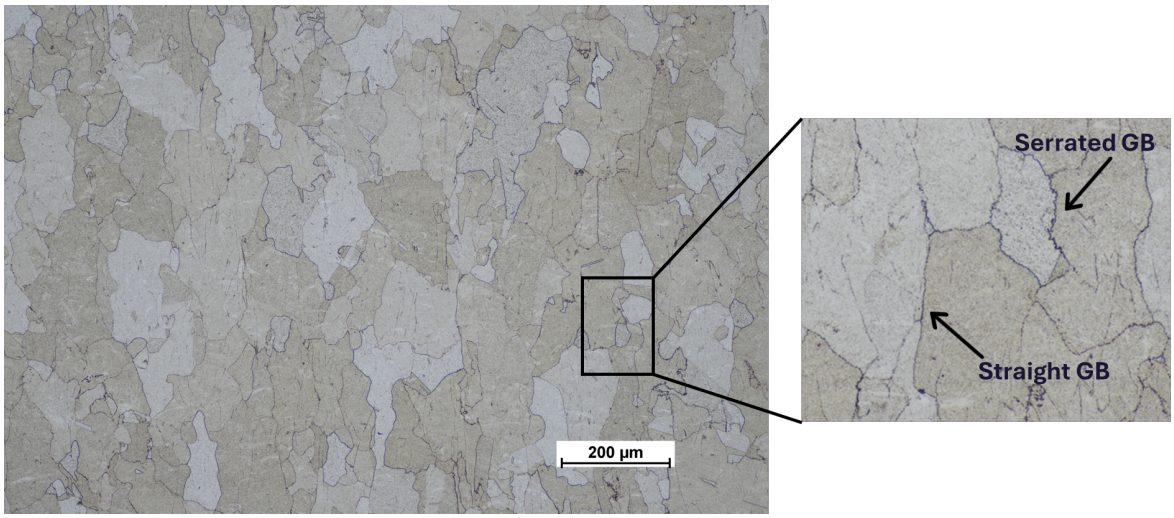


Figure 3.11: Overview of the etched surface along building direction; magnification of GB details, to highlight presence of serrated and straight gain boundaries.

The serration of grain boundaries is typically associated with the presence of precipitates at the grain boundaries, which exert a pinning effect on the boundary segments during high-temperature migration. This phenomenon, often referred to as Zener-drag effect, restricts grain boundary motion and can significantly influence recrystallization and grain growth kinetics. Therefore, it is essential to analyze grain boundaries at higher magnification using electron microscopy to identify the particles responsible for serration and to clarify the underlying mechanism when this phenomenon occurs.
In Figure3.12 is provided a high magnification image of the grain boundary that presents a certain degree of serration. It is evident the presence of larger gamma prime phase precipitated at GB, that in multiple points creates a waviness in the GB path.
No carbide particle has been observed in the GB location, or, if present there, it does not influence the serration mechanism.

Concerning the carbides, an evolution has been observed with respect to the as-built

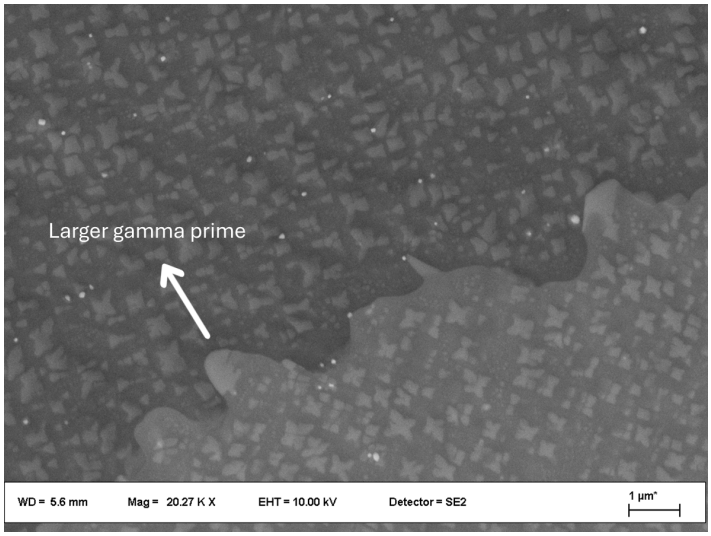


Figure 3.12: SE micrograph of the HIP sample, highlight of the grain boundary serration generated by precipitation of larger gamma prime.

state. They are still identified ad MC-type carbide due to their morphology, shape and dimension, but they are bigger respect to the previous state, with average dimension of $253 \pm 78$nm. Their distribution mirrors is mainly in strides as a residual of the printing process.
In Figure 3.13, a closer view of the carbides is provided, along with a clear visualization of the $\gamma'$ morphology and size distribution. The $\gamma'$ phase exhibits a very broad size distribution, which makes a meaningful statistical analysis impractical. The smallest observed precipitates are approximately 30 nm in size, whereas the largest exceed 500 nm The EBSD mapping provided a detailed analysis of the crystallographic texture, revealing a significant recovery of the columnar grain structure observed in the as-built sample. Recrystallization and grain growth resulted in a coarser grain structure, with most grains exhibiting a fitted ellipse major diameter around XXµm. Figure 3.15 shows the Inverse Pole Figure (IPF) obtained from the EBSD mapping.
A reduction in texture intensity is clearly observed after the HIP treatment, although a certain degree of grain elongation along the building direction is still present. The aspect ratio distribution indicates a significant change compared to the as-built condition: after HIP approximately 50% of the grains fall within a moderate aspect ratio range of 1.2–2.1. This suggests that recrystallization and grain growth promoted the development of a more equiaxed grain structure, even though a residual anisotropy is still retained.
Another strong indication of recrystallization is provided by the reduction in the number of grains per unit area. While in the as-built state a total of 890 grains were counted in the analyzed region, this number decreases to 294 after HIP.
The statistical distributions of both the aspect ratio and the fitted ellipse major diameter are shown in Figure 3.14. The aspect ratio distribution exhibits a narrower spread compared to the as-built condition, pointing to a homogenization of grain morphology. Meanwhile, the distribution of the major diameter is shifted toward higher values, consistent with the overall grain coarsening process.

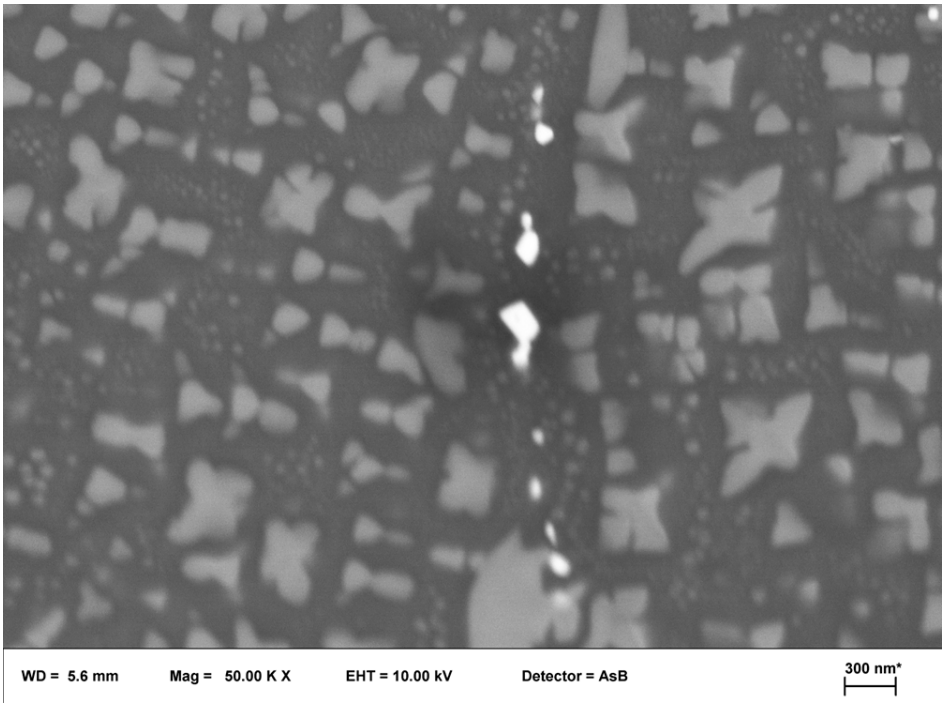


Figure 3.13: High magnification BSE image, MC-type carbides and gamma prime morphology and distribution are evident.

On the right of Figure 3.15, the Kernel Average Misorientation (KAM) map from the EBSD analysis is presented. It clearly demonstrates the effectiveness of the HIP stage in reducing the local misorientation and relieving residual stresses induced during the PBF process.
These observations are consistent with reports in the literature, where HIP at high-temperature post-processing promote recrystallization, grain coarsening, and a reduction of internal residual stresses in additively manufactured Ni-based superalloys.[35].
At this stage of the work, 1180°C is the maximum temperature tested for the SAM alloy. However, literature indicates that higher heat treatment temperatures can enhance recrystallization and grain growth, leading to improved creep resistance. For instance, studies have shown that increasing the heat treatment temperature promotes dynamic recrystallization and grain coarsening in various alloys, which are beneficial for high-temperature applications [36, 37].
Therefore, exploring higher heat treatment temperatures for the SAM alloy could potentially enhance its microstructural stability and creep performance. In Table3.5 is provided a resume of the main findings after the characterization of the HIPed sample, in terms of: aspect ratio, FEMD, % vol of carbides and type of carbide and some notes.

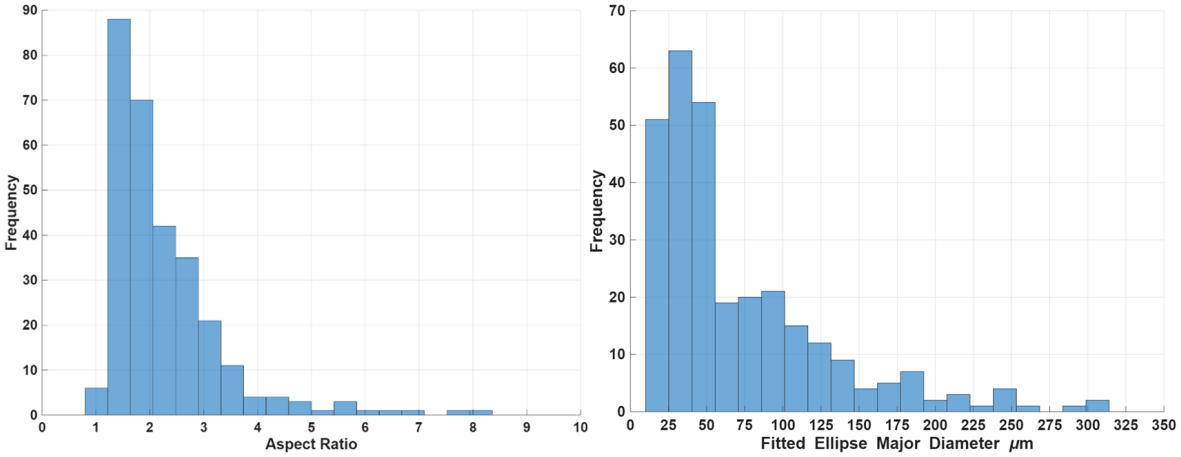


Figure 3.14: Distribution of aspect ratio and fitted ellipse major diameter for the HIP sample.

Table 3.5: Main results after characterization of the HIPed sample.

| State | % Avg. AR | Avg FEMD (µm) | Avg AR | % vol carbides | Carbide type | Notes |
|---|---|---|---|---|---|---|
| HIP | $2.28 \pm 1.24$ | $82.4 \pm 68.9$ | $3.8 \pm 2.2$ | 0.2 | MC | Wide distribution of $\gamma'$; larger $\gamma'$ at grain boundaries give rise to serration |

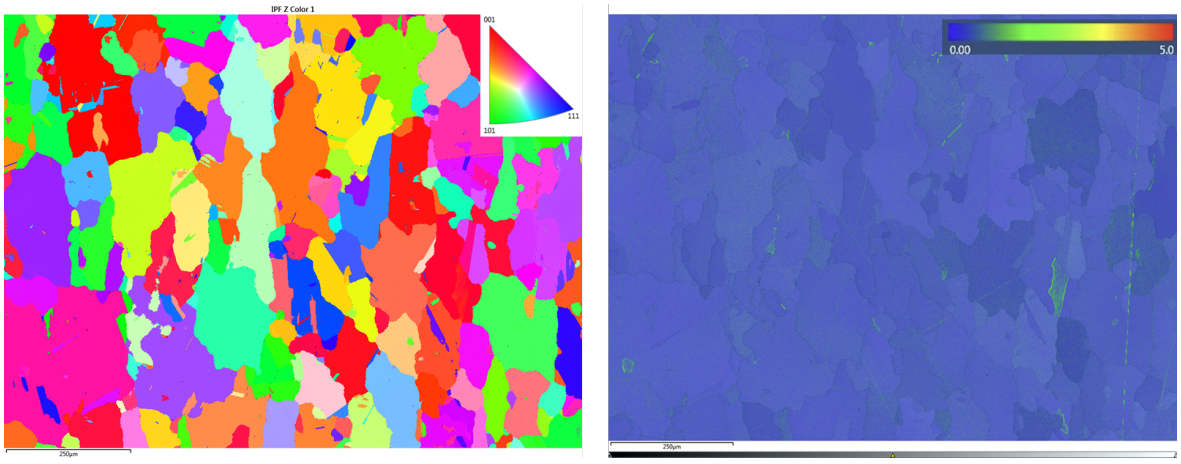

Figure 3.15: Left: EBSD orientation map in IPF representation for the HIPed sample; IPF along building direction. Right: Kernel Average Misorientation map as additional result of the EBSD mapping.

### 3.3.3 Solution step

The first observations on the solutioned sample were carried out using optical microscopy. One of the main points of interest was to verify whether thermally induced porosity occurred during this heat treatment step; however, no evidence of pore formation was detected.
After chemical etching, the grain boundaries became visible, allowing a preliminary assessment of the grain morphology. At first sight, the overall texture appears comparable to that observed after the HIP stage; in Figure 3.16, elongated grains along the building direction are clearly visible.
A closer inspection of the grain boundaries, however, suggests a reduction in the intensity of serration compared to the HIP-treated condition. It is important to underline that this statement is currently based on qualitative assessment only, as no quantitative measurements have been performed to confirm this impression.

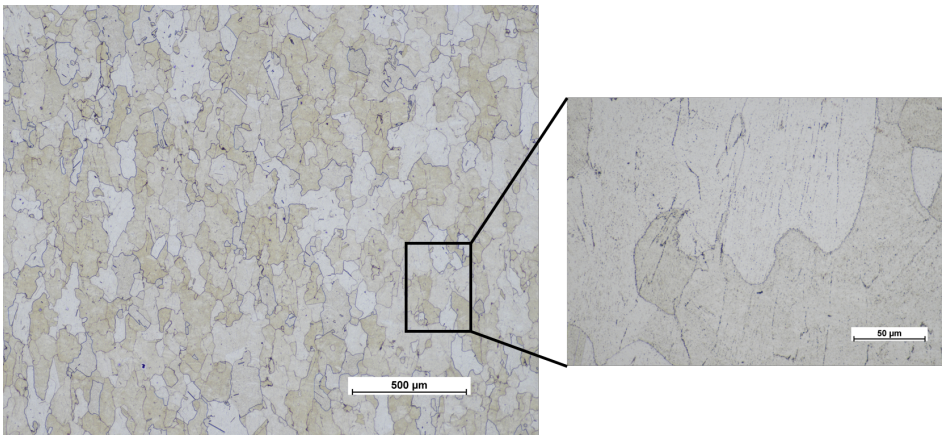


Figure 3.16: LOM image with overview of the surface after etching on the left and closer look of grain boundaries; solutioned sample.

After the HIP and solution treatments, the microstructure of the SAM alloy shows interesting changes in the grain boundary serration, $\gamma'$-precipitate morphology, and their interrelations. Figure 3.17 is particularly informative in this respect. On the left, there is a grain boundary (GB) with a clear degree of serration, which appears associated with large $\gamma'$ precipitates decorating, or pinning, the boundary. These particles exert drag on migrating boundary segments, leading to the characteristic wavy or serrated profile.
On the right of the image, however, a triple point is shown where the grain boundaries appear nearly straight. In this region, $\gamma'$ precipitates at the grain boundaries have a planar / film-like morphology rather than large, discrete particles. In other words, instead of isolated, coarse boundary precipitates, there is a more continuous, planar layer (or at least precipitates whose dimensions parallel the boundary are large relative to their thickness). Where this planar $\gamma'$ morphology exists, the serration is essentially absent. It's reasonable to think that some boundary $\gamma'$ precipitates may coarsen, dissolve, or transform into more planar films, reducing their ability to pin

boundary movement locally. In Figure 3.17,it's also evident the presence of a bright

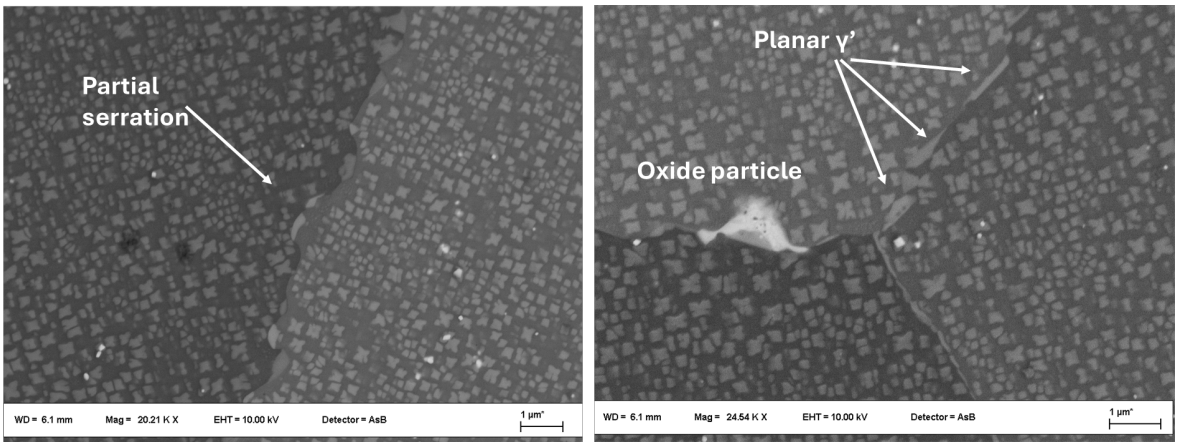


Figure 3.17: BSE images of the solutioned sample; on the left presence of globular/fan like gamma prime phase and consequent GBS. On the right planar gamma prime and so straight GB. Also visible an oxide particle.

phase with a relatively large size, on the order of 3ţm. In order to clarify its chemical nature, a line analysis was carried out using the EDS detector. It should be noted that, due to the working principle of EDS, light elements such as carbon and oxygen are not reliably quantified; nevertheless, in Figure 3.18 signals corresponding to both are visible. Considering the overall morphology, the phase is more likely to be an oxide particle enriched in hafnium and tantalum rather than a carbide. This interpretation is supported by two observations: (i) the relatively large size of the particle, and (ii) its very low frequency in the analyzed microstructure, both of which are atypical for oxides in this alloy system. The EDS spectra of the alloy also revealed signals in the energy range where both Hf and Ta characteristic peaks are expected. However, due to their close proximity in the periodic table, the characteristic X-ray emission lines of Hf and Ta occur at nearly identical energies (for example, the L-$\alpha$ lines at approximately 7.9–8.1 keV). Considering that the typical energy resolution of an EDS detector is on the order of 120–130 eV at Mn K-$\alpha$, the peaks of Hf and Ta cannot be unambiguously separated. As a result, the apparent signal in this region must be interpreted with caution, and the identification of Hf versus Ta should be regarded as qualitative rather than quantitative.

With regard to the carbide population, the situation appears essentially unchanged compared to the previous processing step. Only MC-type carbides were detected, with an average size of $229.5 \pm 63.7$ nm. Given the relatively wide size distribution and the associated variability, it is reasonable to conclude that no significant evolution of the carbide morphology occurred after the HIP stage. In particular, neither the appearance of secondary carbide types nor evidence of substantial coarsening, dissolution, or re-precipitation was observed within the analyzed microstructural regions.This stability suggests that the HIP treatment mainly acted on the matrix and grain boundary structure, without markedly affecting the existing carbide population.
Again, the carbides are present in strides as consequence of segregation after the print-

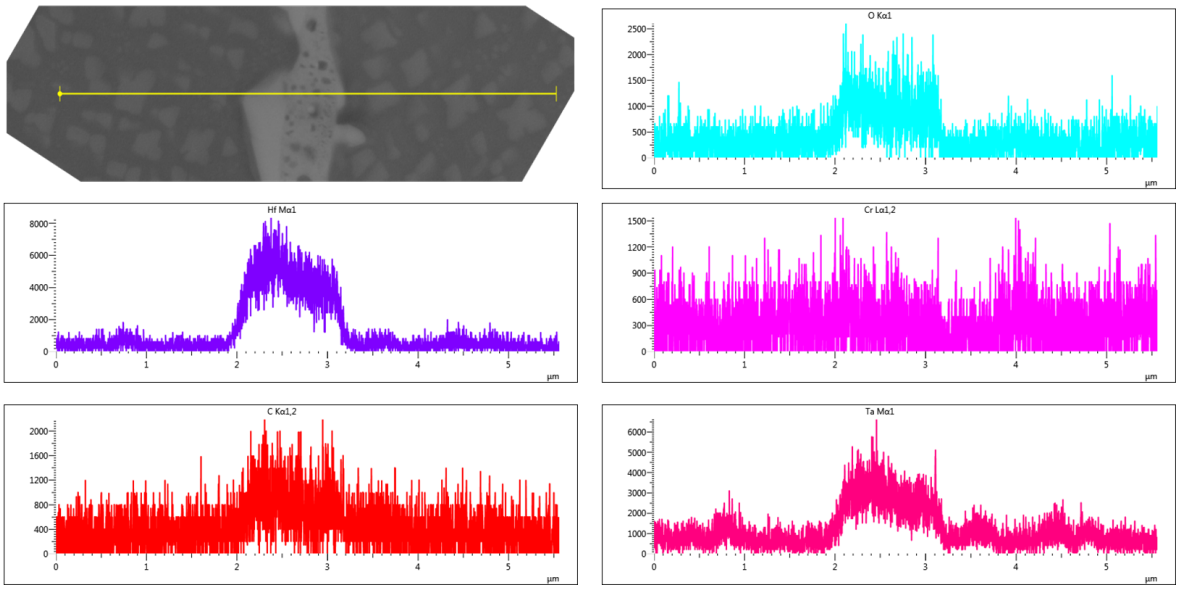


Figure 3.18: Result of line EDS analysis across the phase located at grain boudary; most probably ad oxide particle.

ing process, as it's possible to notice in the Figure3.19. In this case also and EDS mapping was performed, to cofirm the presence of hafnium and tantalum enriched carbide; also tungsten is present but the peak has low intensity. The same consideration done previously about the Hf and Ta overlap are still valid, and so the analysis is just qualitative and not quantitative.

From Figure 3.19, on the right, it is also possible to evaluate the evolution of the $\gamma'$ morphology. At this stage, the strengthening phase exhibits a more regular and homogeneous distribution compared to the HIP condition. The precipitates appear better defined in shape and slightly more uniform in size, which suggests that the thermal exposure during the solution treatment has promoted a partial reshaping of the $\gamma'$ phase. Nevertheless, the morphology cannot yet be considered fully optimized, as the precipitates still deviate from the ideal cuboidal form typically desired for maximizing high-temperature strength. But it's important to state that this heat treatment step does not aim to reach already the optimal $\gamma'$ distribution, this is the goal of the aging step.

Subsequent to the HIP treatment, the solution step does not appear to introduce substantial modifications in terms of grain morphology. The grains maintain a similar elongated shape and aspect ratio distribution, indicating that the main recrystallization and coarsening processes already occurred during HIP. In other words, the solution treatment primarily serves to homogenize the microstructure and dissolve residual secondary phases, without significantly altering the overall grain geometry. Further confirmation of this stability is provided by the EBSD analysis: the Inverse Pole Figures (IPF) (Figure 3.20) reveal a texture comparable to that observed after HIP, with no clear evidence of additional recrystallization. Likewise, the statistical evaluation of aspect ratio and fitted ellipse diameters (Figure 3.21) demonstrates only minor variations, remaining within the same range measured in the HIP state. These observations

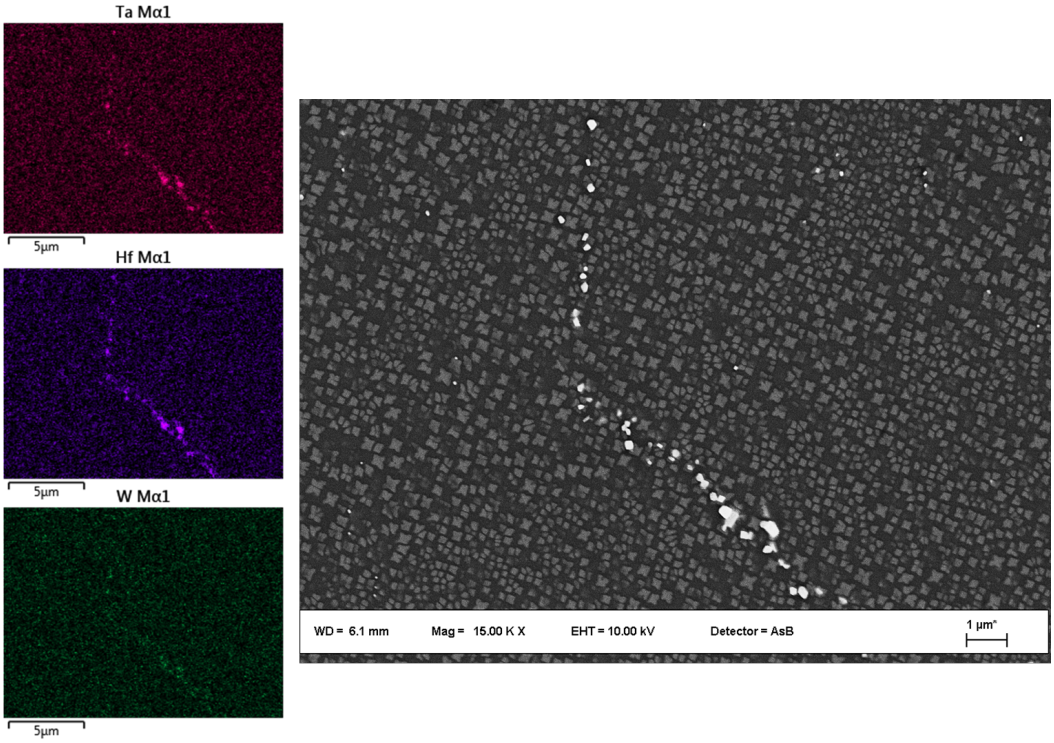


Figure 3.19: BSE image with high contrast to highlight the carbide presence, along with main results of the EDS scanning

suggest that, once the HIP stage has reduced the as-built anisotropy, the subsequent solution treatment has no driving force for further grain structure evolution.

Table3.6provides a resume of the main findings for the solutioned condition of the SAM alloy.

Table 3.6: Main results after characterization of the solutioned sample.

| State | % Avg. AR | Avg FEMD (µm) | Carb. dim (nm) | % vol carbides | Carbide type | Notes |
|---|---|---|---|---|---|---|
| Solution | $2.23 \pm 1.21$ | $84.3 \pm 64.9$ | 229.5±63.7 | 0.2 | MC | Planar $\gamma'$ at GB; no serration. |

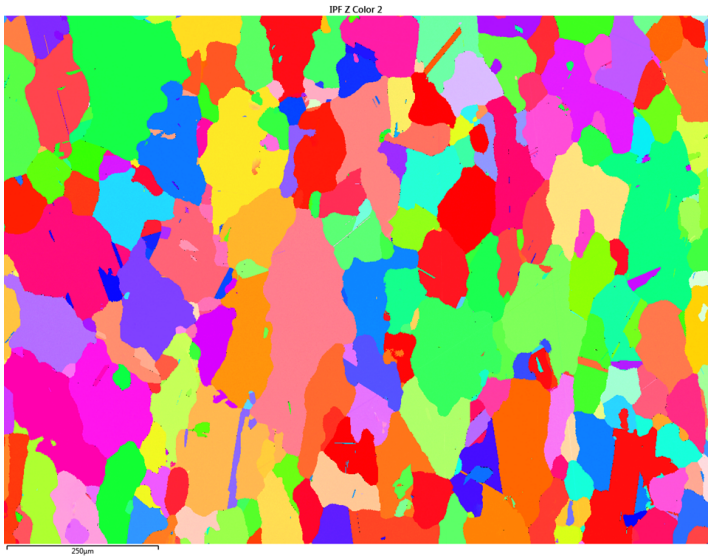


Figure 3.20: EBSD orientation map in IPF representation for the solutioned sample; IPF along building direction.

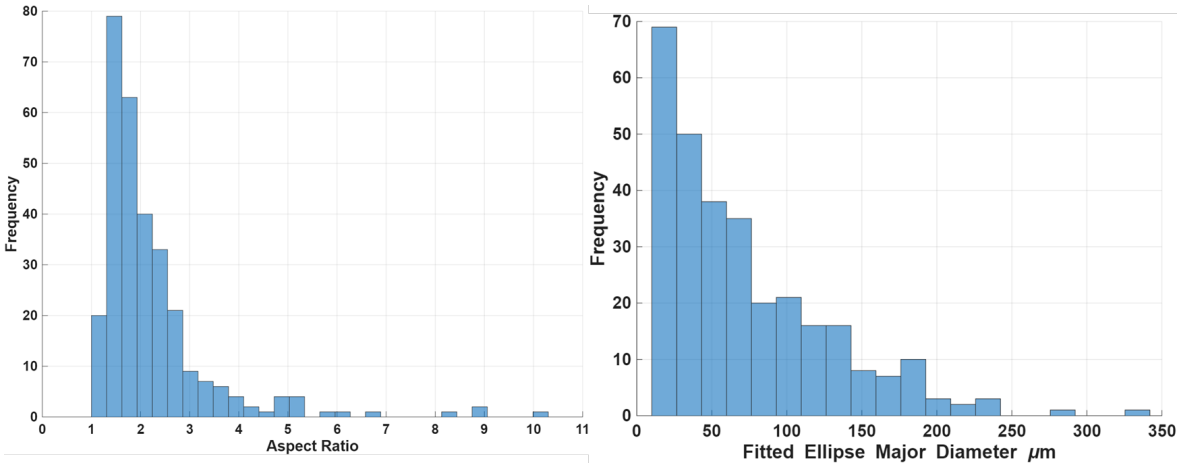


Figure 3.21: Distribution of aspect ratio and fitted ellipse major diameter for the solutioned sample.

### 3.3.4 Aging step

The aging step was performed at 1000°C, with the aim of reaching an optimal morphology and distribution of $\gamma'$, together with a more homogeneous microstructure. This treatment is designed to promote the controlled precipitation and coarsening of the $\gamma'$ phase, allowing the particles to evolve toward a stable cuboidal morphology and a uniform distribution. Such conditions are essential to maximize the strengthening effect of $\gamma'$ by impeding dislocation motion, while also ensuring long-term stability of the microstructure during high-temperature service.
The characterization strategy adopted for the aged sample follows the same approach as for the previous conditions, starting with optical microscopy after etching the surface. An overview of the microstructure is provided in Figure 3.22, where elongated grains along the building direction are visible. A closer inspection of the grain boundaries is required to evaluate whether serration, which was already partially reduced after the solution step, is still present at this stage. Based on optical microscopy observations, it is possible to state—with the necessary caution—that serration appears to be completely lost after aging. Figure 3.23 provides a higher magnification of a representative grain boundary, where only straight boundaries are observed.
It is important to underline that the assessment of grain boundary serration in this work is qualitative in nature, relying on the authors' visual inspection of micrographs rather than on quantitative measurements.

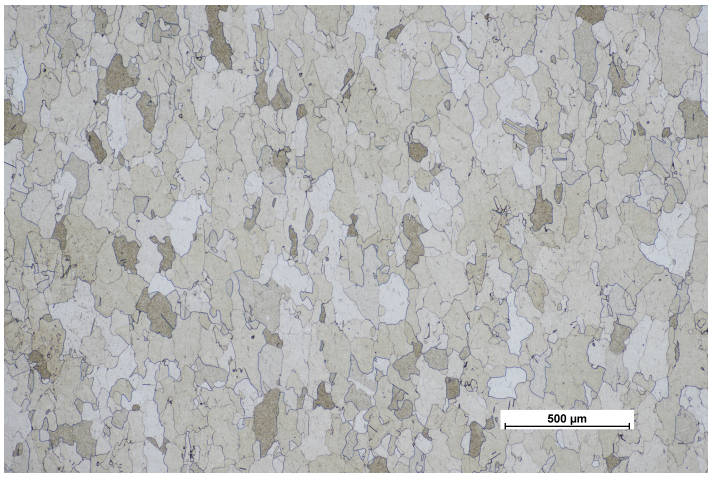


Figure 3.22: Overview of the aged sample after etching; LOM image

To better understand the causes behind the loss of grain boundary serration, a more detailed investigation using electron microscopy is required. Optical microscopy alone, while useful for a first overview, is not sufficient to reveal the fine-scale interactions between grain boundaries and boundary-precipitated phases.
Figure 3.24 provides an overview of the microstructure after aging, where grain boundaries appear predominantly straight and linear, with no evidence of the waviness that was clearly visible in the HIP condition and only partially retained after the solution treatment. Whereas in the previous stages it was frequent to observe the precipitation of larger $\gamma'$ particles decorating the grain boundaries, at this point such features are much less common. The concurrent absence of serration suggests that the boundaries

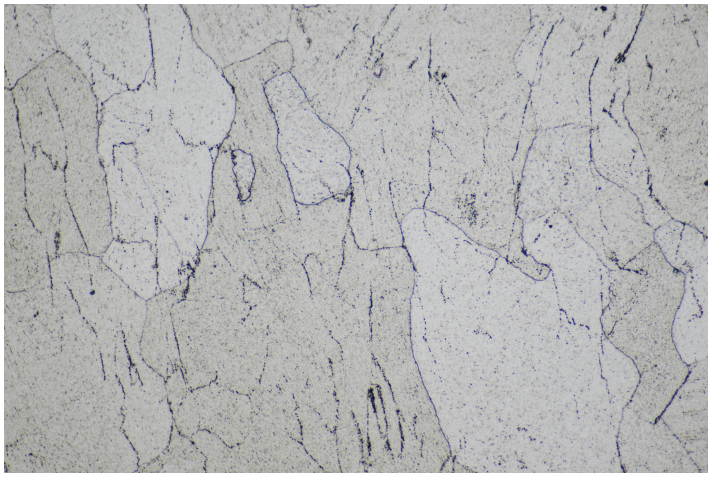

Figure 3.23: High magnification with optical microscope of the aged sample; details of the grain boundaries.

still possess sufficient mobility, but, in the absence of boundary-precipitated phases capable of exerting a pinning effect, the serrated morphology is no longer sustained. This interpretation is consistent with the hypothesis that the morphology and distribution of $\gamma'$ strongly influence the stability of serrated boundaries.
Figure 3.25 illustrates the most representative example: in the center of the image, a grain boundary can be discerned, although it is barely visible and exhibits very low contrast with the surrounding matrix. The flatness and indistinct appearance of this boundary reinforce the conclusion that grain boundary serration has been completely suppressed after aging, leaving behind straight, energetically minimized interfaces.

As mentioned, the main goal of the aging step is to achieve a suitable distribu-

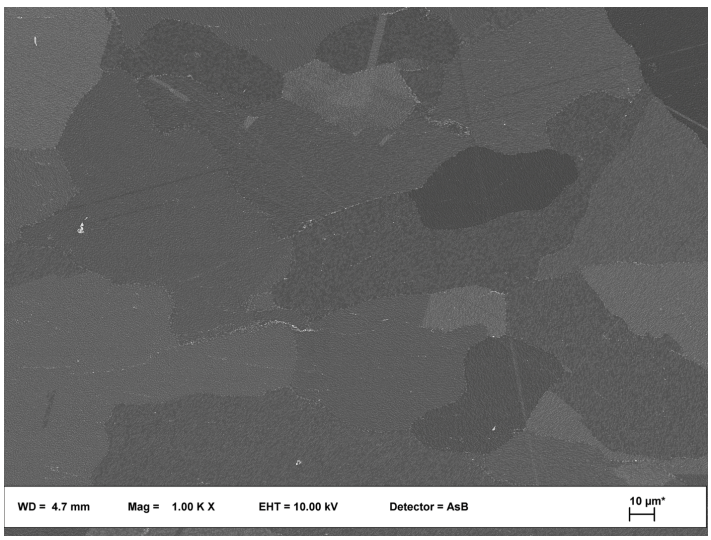


Figure 3.24: BSE image to provide an overview of the grain boundaries of the aged sample.

tion, morphology, and size of the $\gamma'$ phase. A peculiarity of this material under the present processing conditions is the coexistence of different $\gamma'$ morphologies within the

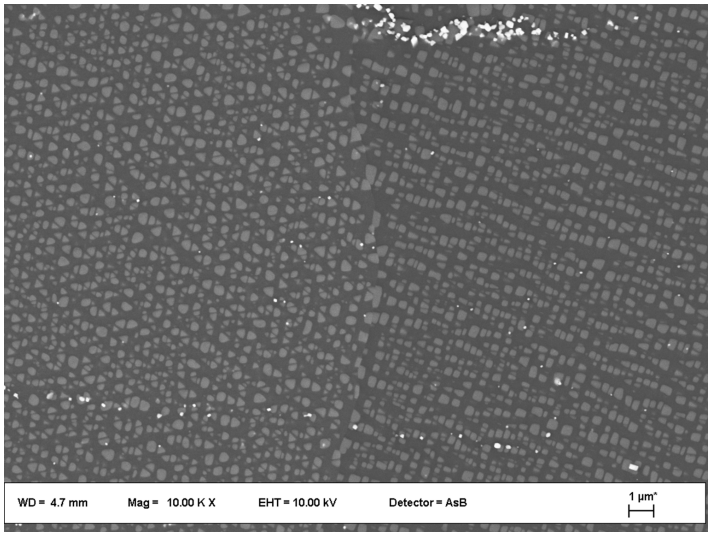


Figure 3.25: High magnification of a grain boundary with BS electrons; aged sample.

same sample, sometimes even in directly adjacent grains, as shown in Figure 3.26. In fact, neighboring grains can exhibit markedly distinct $\gamma'$ shapes, ranging from regular cuboidal precipitates to triangular or even rounded ones. The triangular features, visible in Figure 3.26-C, could be attributed to a cutting-direction artifact, whereas the rounded or irregular precipitates appear unrelated to the other morphologies. These observations clearly indicate that, under the current conditions, the material does not achieve the desired uniformity in $\gamma'$ distribution and morphology. Therefore, further refinement of the aging step is necessary. Carbides, as characterized in the previous stages, appear unchanged, with an average size of $249 \pm 82$ nm. Their distribution still reflects the solidification conditions of the printing process, with only a low frequency of localized clusters, as shown in Figure 3.27. Table3.7 provides a resume of the main finding after the characterization of the aged sample.
It should be noted that, since no significant changes in grain size or morphology were observed after the solution step, performing an additional EBSD analysis on the aged sample was considered unnecessary. This technique is delicate and time-consuming, and given that the aging treatment was carried out at lower temperatures compared to the solution step, no grain growth was expected.

Table 3.7: Main results after characterization of the aged sample.

| State | % Avg. AR | Avg FEMD (µm) | Carb. dim (nm) | % vol carbides | Carbide type | Notes |
|---|---|---|---|---|---|---|
| Aging | N.A. | N.A. | $249 \pm 82$ | 0.2 | MC | Lost of serration. |

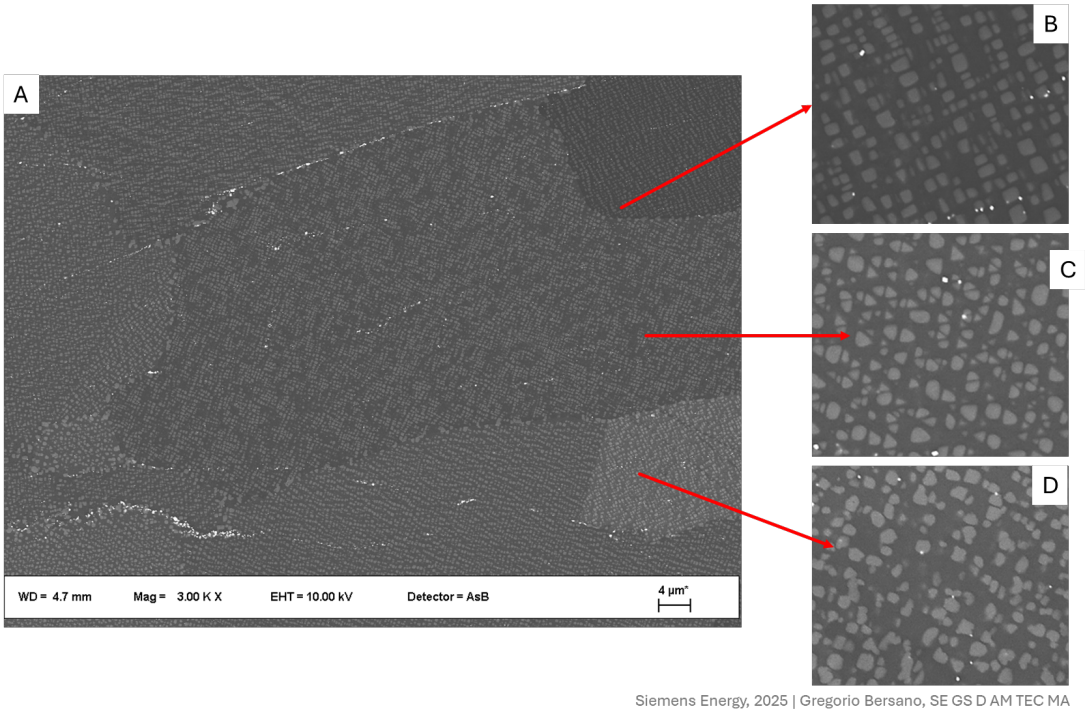


Figure 3.26: BES images that show: A-overview of adjacent grains; B-detail of a cuboidal gamma prime morphology; C-detail of a triangular gamma prime and D-rounded and more irregular gamma prime morphology.

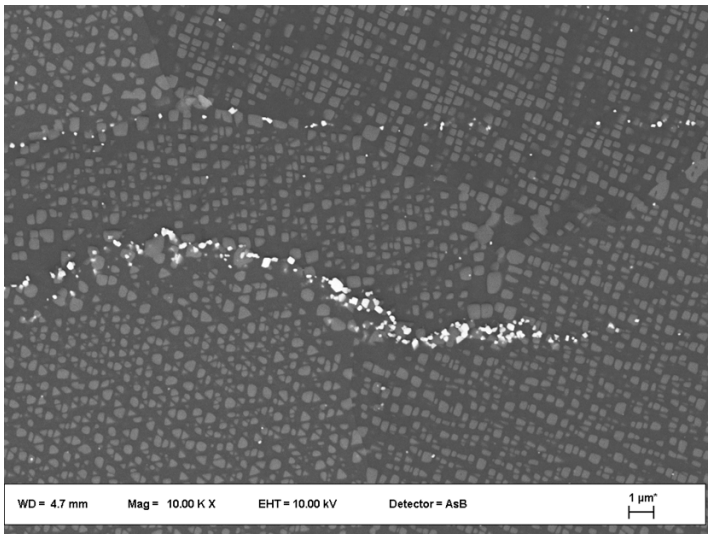


Figure 3.27: BSE image shows a cluster of carbides.

### 3.3.5 Summary of the main findings after the preliminary heat treatment

The characterization of the SAM alloy across the different processing steps (as-built → HIP → solution → aging) highlights the following microstructural trends:

- **As-built:** Columnar grains with strong texture along the building direction. High dislocation density (KAM $\sim 2.2°$), fine dendritic structure, and presence of MC-type carbides ($\sim$114 nm). Typical PBF defects (LOF, gas porosity $\sim 0.26\%$).
- **HIP:** Almost complete removal of porosity/defects. Recrystallization and grain coarsening, with reduced texture intensity. Serrated grain boundaries induced by coarse $\gamma'$ precipitates at GB. Carbides coarsen ($\sim$254 nm). Broad $\gamma'$ size distribution, up to 500 nm.
- **Solution:** Grain morphology largely unchanged from HIP (main recrystallization already occurred). Serration intensity decreases: planar $\gamma'$ films at GB reduce pinning. MC-type carbides remain stable ($\sim$229 nm), with no new carbide types. $\gamma'$ distribution becomes more homogeneous, though not yet cuboidal.
- **Aging:** Grain boundaries appear straight, serration completely lost. $\gamma'$ evolves toward more regular morphology, but uniform cuboidal distribution is not fully achieved (coexistence of cuboidal, triangular, rounded shapes). Carbides remain essentially unchanged ($\sim$249 nm). No grain growth expected; therefore EBSD analysis was not repeated.

The SAM alloy shows a clear microstructural evolution: (i) HIP is the dominant step for recrystallization, grain coarsening and defect removal, (ii) solution treatment partially stabilizes the microstructure and reshapes $\gamma'$, but does not push forward the recrystallization and grain growth, (iii) aging improves $\gamma'$ morphology but further optimization is required to obtain a uniform cuboidal distribution and to retain beneficial grain boundary serration.

In Table 3.8 a summary of the main findings from the characterization of the preliminary heat treatment is presented. The data are reported in terms of $\gamma'$ volume fraction, carbide type, average size, and volume fraction. A nearly constant volume fraction $\gamma'$ is observed in all steps (besides the as built where no $\gamma'$ is present); however, as shown in the micrograph discussed above, an evolution can be clearly distinguished in the size, shape and morphology of the strengthening phase. With regard to the carbides, when considering the uncertainty associated with the imaging analysis, it's possible to state that solution and aging do not affect their fraction and dimension.

Table 3.8: Microstructural features at different heat treatment steps.

| **Step** | **$\gamma'$ vol.%** | **Carbide vol.%** | **Carbide size [nm]** | **MC carbides** | **$M_{23}C_6$ carbides** |
|---|---|---|---|---|---|
| HIP | 31 | 0.2 | 253 ± 78 | Yes | No |
| Solution | 30 | 0.2 | 229 ± 64 | Yes | No |
| Aging | 31 | 0.2 | 249 ± 82 | Yes | No |

### 3.3.6 Crystallographic evolution during preliminary heat treatment

The evolution of grain morphology and crystallographic texture during the preliminary heat treatments was analyzed by EBSD, as illustrated in Figure 3.28.

In the as-built condition, the IPF maps reveal a strong preferential orientation along the building direction, with columnar grains elongated through the building direction. This anisotropic structure is reflected in the aspect ratio (AR) distribution, which shows a significant fraction of grains with AR $> 2.5$, confirming the presence of highly elongated grains. The fitted ellipse major diameter (FEMD) distribution is narrow, consistent with the relatively fine microstructure resulting from rapid solidification.
After the HIP treatment, a marked change is observed. The texture intensity decreases, and the IPF maps show more randomly oriented grains, indicating partial recrystallization. The AR distribution shifts toward lower values, with approximately half of the grains within the range 1.2–2.1, confirming a reduction of grain elongation. At the same time, the FEMD distribution becomes broader, with an overall increase in the average grain size. The lower number of grains per unit area further supports this interpretation.
Subsequent solution treatment does not significantly alter the grain morphology. Both the AR and FEMD distributions remain essentially unchanged compared to the HIP condition, suggesting that the main recrystallization and coarsening processes already occurred during the HIP stage.
All these results are clear in Figure3.29 were are reported the cumulative distribution functions for the aspect ratio and the fitted ellipse major diameter.

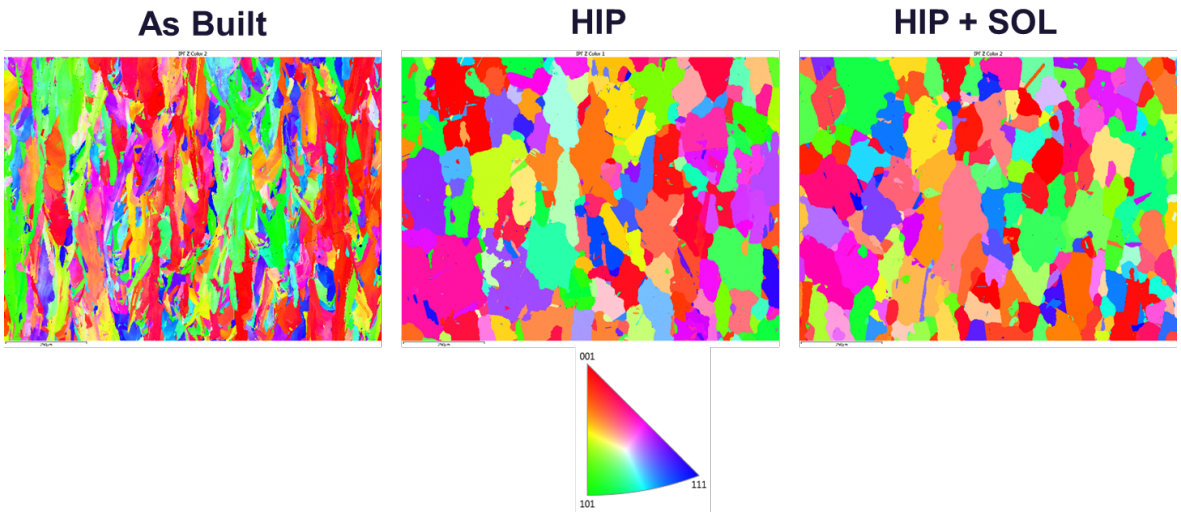


Figure 3.28: Crystallographic evolution showed with the IPF; legend of the bottom

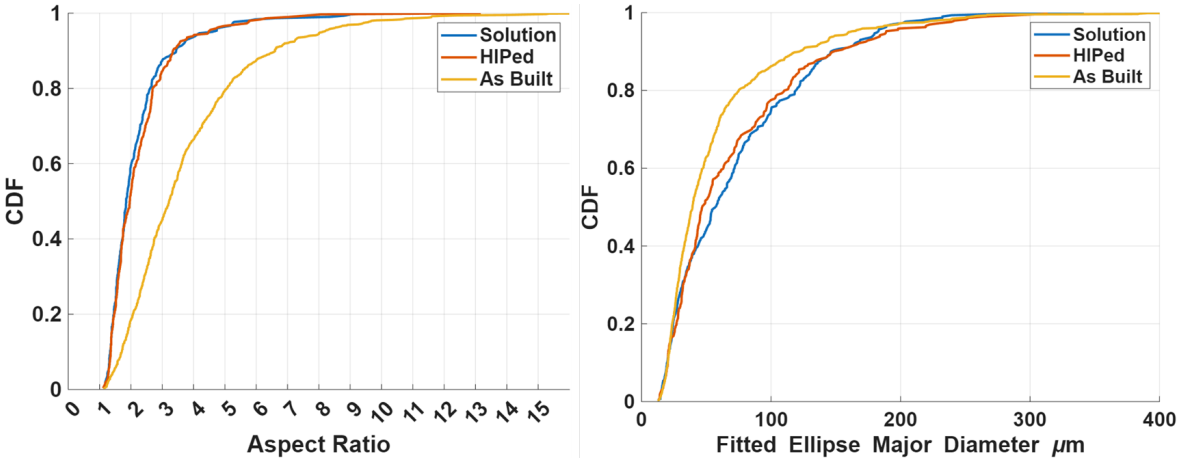


Figure 3.29: CDF distribution to resume the results of the preliminary heat treatment in terms of AR and FEMD evolution.

### 3.3.7 Tensile test

During the development of the SAM material project, it was never performed an evaluation of the mechanical properties, in particular regarding the tensile test properties. It was done a campaign of tensile tests to have a reference for this material and creating a benchmark. Since this material is design to be processed by means of PBF-LB the products of this process are affected by high anisotropy. To evaluate this phenomena the as built sample has been tested along building direction (0°) and perpendicular to building direction (90°). In the same way, also the full heat treated sample has been tested in both direction, to asses the effectiveness of the heat treatment in reducing the anisotropy. As mentioned in Chapter2, due to lack of material, it was possible to perform just one test for each condition, and not three as for reference standard. In particular, four test were performed, two for the as built condition and two for the full heat treated condition (HIP + solution+ aging). The plots of the stress strain curves are represented in Figure3.30, while the numeric results are reported in Table3.9.

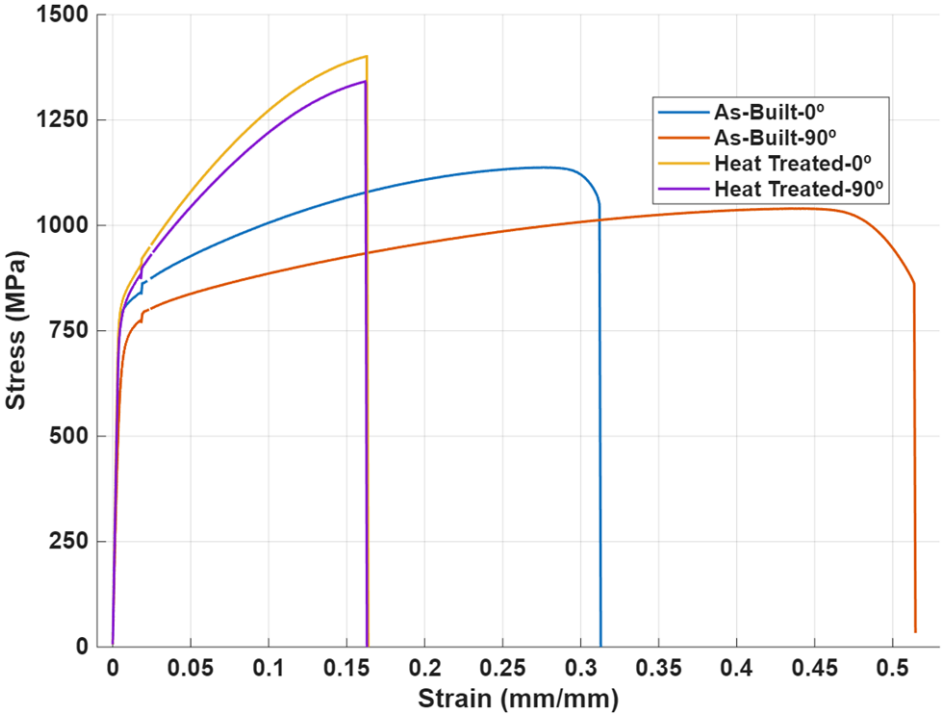


Figure 3.30: Stress strain plot of the tensile test for the 0° and 90° sample tested in the as build condition and after the full heat treatment

For the as-built condition, a clear anisotropy is observed. Specifically, the Young's modulus ($E$) is significantly lower in the 90° direction (144 GPa) compared to the 0° direction (191 GPa), while similar trends are visible for the yield strength ($R_{p0.2}$) and ultimate tensile strength (UTS). This difference between BD-parallel and BD-perpendicular directions is consistent with previous studies on PBF-LB Ni-based superalloys, where columnar grain growth lead to direction-dependent mechanical properties [32, 34].
After the heat treatment (HT), the anisotropy is reduced. Both $E$ and strength val-

ues become closer between the 0° and 90° directions (e.g., $E$ increases to 195 GPa in 90° and 215 GPa in 0°). This improvement indicates the effectiveness of the post-processing treatment in homogenizing the microstructure, likely via recrystallization and reduction of texture intensity that was demonstrated after the HIP and solution treatment.

Comparing the as-built and fully heat-treated (FHT) conditions, it is evident that the heat treatment leads to a significant increase in strength (e.g., UTS rises from 1040–1137 MPa in AB to 1341–1401 MPa in HT) while reducing ductility, as shown by the decrease in elongation at 50% area ($A_{50\%}$) and reduction in area (Z). This behavior is typical for Ni-based superalloys, where the formation and coarsening of $\gamma'$ precipitates during heat treatment increase yield and ultimate strength, but with loss of plasticity [1].

Table 3.9: Tensile test results for the samples in as-built (AB) and heat-treated (HT) conditions, both tested in parallel and perpendicular direction respect to the BD.

| **Sample** | **AB_90** | **HT_90** | **AB_0** | **HT_0** |
|---|---|---|---|---|
| $E$ (GPa, 30/70*) | 144 | 195 | 191 | 215 |
| $R_{p0.2}$ (MPa) | 683 | 780 | 795 | 813 |
| UTS (MPa) | 1040 | 1341 | 1137 | 1401 |
| $A_{50\%}$ (%) | 37.6 | 15.7 | 36.5 | 16.7 |
| Z (%) | -36.7 | -9.8 | -29.5 | -9.1 |

* The elastic modulus was evaluated in the linear part of the plot, particularly between 30% and 70% yield strength.

### 3.3.8 Hardness test, evolution and comparison with competitive alloys

Table 3.10 an Figure3.31 presents the average and standard deviation values of HV10 hardness for various alloys in both as-built (AB) and heat-treated (HT) conditions. The data highlight several important observations:

- **As-Built Condition**: The SAM alloy exhibits a hardness of 339 HV10, which is lower than that of other alloys such as STAL15 (360 HV10) and IN738 (354 HV10). This lower hardness is indicative of a more ductile microstructure, beneficial for the printability of the alloy. A more ductile material can better accommodate the thermal stresses and distortions inherent in the additive manufacturing process, leading to improved printability [14].
- **Heat-Treated Condition**: After heat treatment, the SAM alloy's hardness increases to 411 HV10, surpassing STAL15 (FHT-STAL15, 374 HV10) and approaching that of IN939 (FHT-IN939, 469 HV10). This increase is attributed to

the precipitation of strengthening phases (e.g., $\gamma'$), which enhance strength but reduce ductility.

- **Comparison with Other Alloys**: The hardness evolution in SAM is comparable to IN939, which also shows significant hardening post-heat treatment. However, the lower as-built hardness of SAM suggests a favorable balance between printability and mechanical properties.

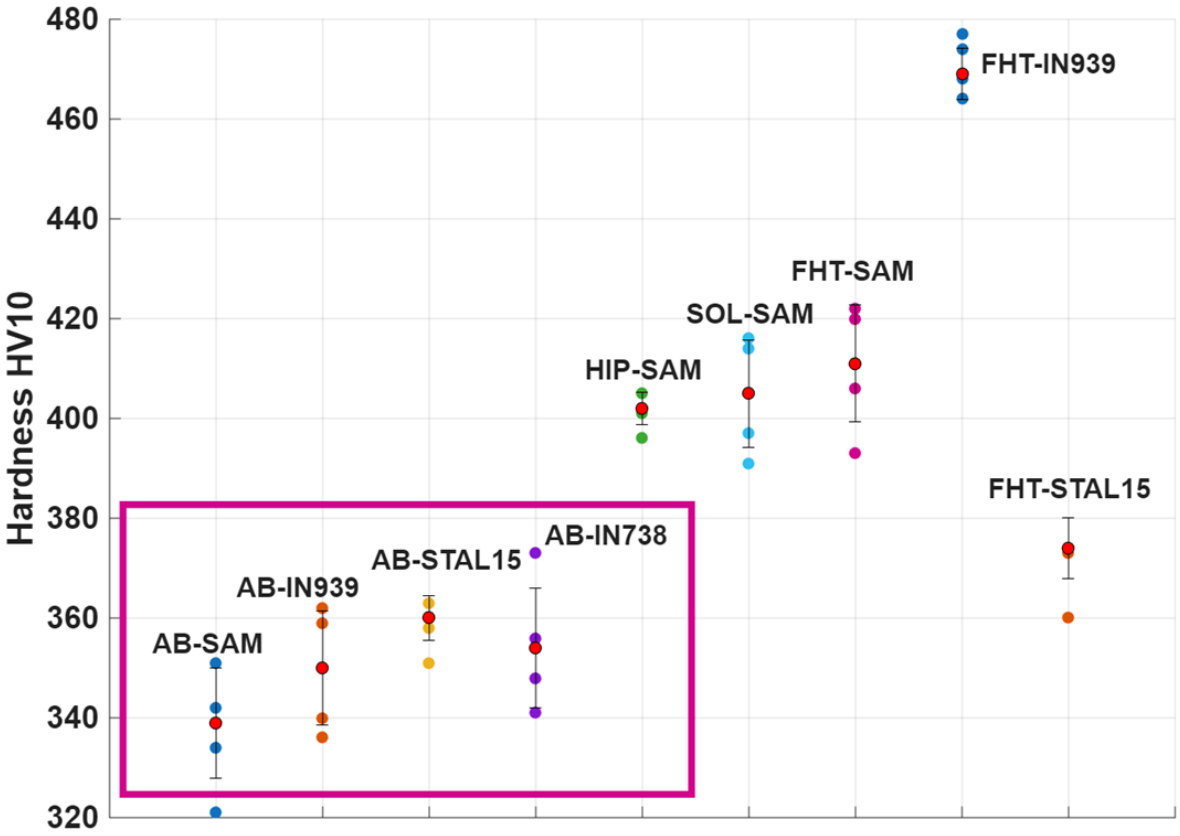


Figure 3.31: Scatter plot with error bar of the HV10 measurements; comparison between SAM and competitive alloys

Table 3.10: Average and standard deviation values of hardness (HV10) for different samples,; SAM alloy against competitive alloys.

| Sample | Average | Standard deviation |
|---|---|---|
| AB-SAM | 339 | 11.06 |
| AB-939 | 350 | 11.39 |
| AB-STAL15 | 360 | 4.51 |
| AB-IN738 | 354 | 11.93 |
| HIP-SAM | 402 | 3.27 |
| SOL-SAM | 405 | 10.74 |
| FHT-SAM | 411 | 11.72 |
| FHT-IN939 | 469 | 5.13 |
| FHT-STAL15 | 374 | 6.16 |

## 3.4 Solution heat treatment trials

The solution heat treatment trials were carried out in the range from 1180°C to 1280°C, in contrast to the initial Design of Experiments (DoE) based on the ThermoCalc predictions. According to the simulations, incipient melting was expected around 1175°C. However, since the HIP stage had already been successfully performed at 1180°C without any evidence of melting, this discrepancy raised doubts about the reliability of the predicted results. For this reason, the experimental campaign was designed to start from 1180°C and proceed with increments of 20°C, in order to better define the actual melting onset and to validate the process window.
It's important to highlight, that at this stage of the thesis work, no DSC data were still available, otherwise it could have been easier to find the best temperature for the solution heat treatment step.
All the solution heat treatment runs were carried out directly on the as-built material, deliberately skipping the HIP stage. The choice was motivated by the fact that HIP has already been demonstrated to be highly effective in closing the defects introduced during the printing process, as shown in the previous section. Consequently, in the following characterization, no specific defect analysis is reported, since the defects observed are expected to correspond to those retained from the additive manufacturing process. The focus is therefore placed on the microstructural evolution induced by the solution treatments, rather than on defect healing mechanisms already addressed through HIP.

### 3.4.1 Time temperature plots

In Figure3.32, the time–temperature profiles for all the performed runs are reported. The heating process can be divided into two distinct stages: an initial rapid increase up to 700°C with a rate of approximately 30°C/min, followed by a slower ramp of about 6°C/min until the soaking temperature was reached.
After four hours at the target temperature, the subsequent cooling stage is clearly visible. The plots highlight the high consistency of the heat treatment set-up, which allowed for the reproduction of comparable thermal conditions across the runs. Two exceptions can be noted: the test performed at 1240°C, which shows a significantly slower cooling rate down to 700°C, and the run at 1260°C, for which no cooling data were recorded due to thermocouple failure during furnace removal. Nevertheless, based on the consistency of the preceding results, the cooling rate in this case can be reasonably estimated to fall within the range of 300–370°C/min. The planned trials of the solution heat treatment are resumed in this design of experiment, Table 3.11, in which are reported: target temperature, soaking time, cooling rate, maximun temperature reached during the run and the furncace error. In particular, the cooling rate has been evaluated between soak temperature and 800 °C, at which no more microstructural changes are expected.

Table 3.11: Experimental heat treatment runs and main parameters.

| **Run** | **Temp (°C)** | **Max T reached (°C)** | **Soak Time (hours)** | **Cooling rate* (°C/s)** | **Furnace Error (±°C)** | |
|---|---|---|---|---|---|---|
| 1 | 1180 | 1186 | 4 | 309 | +6 | |
| 2 | 1200 | 1206 | 4 | 370 | +5 | |
| 3 | 1220 | 1224 | 4 | 367 | +6 | |
| 4 | 1240 | 1244 | 4 | 5 | +4 | |
| 5 | 1240 | 1244 | 2 | 370 | +3 | |
| 6 | 1260 | 1264 | 4 | ND** | +4 | |
| 7 | 1280 | 1286 | 4 | 336 | +6 | |

** The cooling rate is evaluated between the soaking temperature and 800 °C*
*** During this trial the thermocouple broke during removal from the furnace*

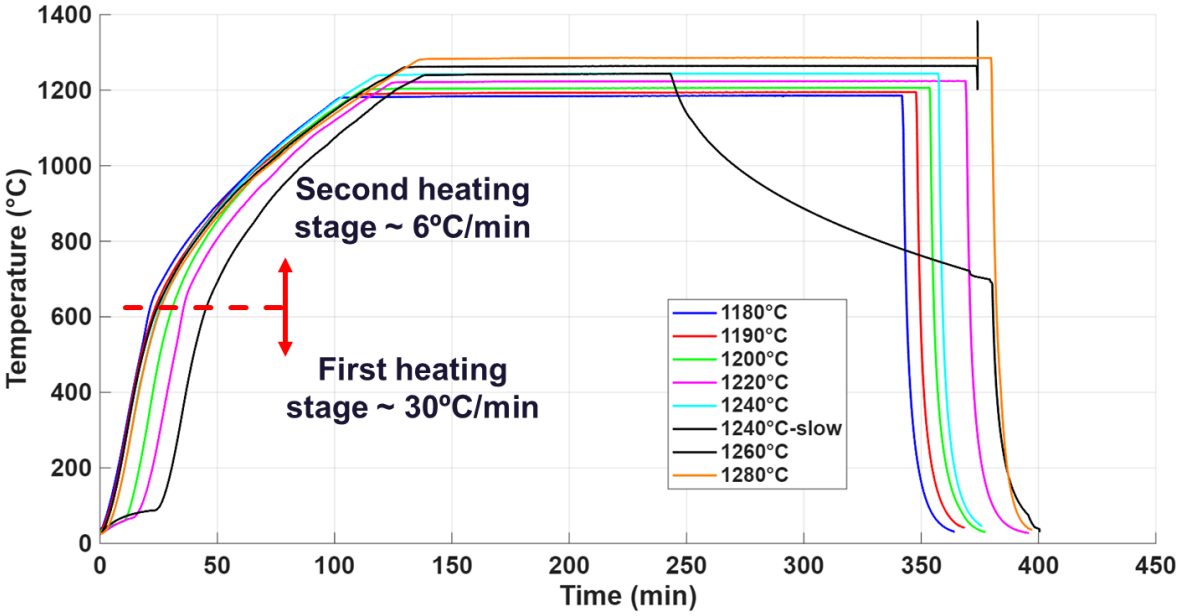


Figure 3.32: Time-temperature plots of all solution heat treatment trials

### 3.4.2 Run – 1180°C - characterization

As a first run, the same temperature used during the HIP step was repeated, in order to both verify the effectiveness of the present experimental setup and to investigate the influence of the cooling rate at this temperature. According to the data provided by the company that carried out the HIP treatment, the applied cooling rate was below 10°C/min, whereas in the present trials, as previously mentioned, the cooling rate exceeded 300°C/min. Such a significant difference offers the opportunity to explore the role of cooling kinetics on the resulting microstructure. In the literature, several investigations on different alloys—for instance the study by Martelli *et al.*—highlight that the applied pressure during HIP has only a negligible effect on densification and grain coarsening [29]. Repeating the solution treatment at the same temperature provides the possibility to validate and complement these findings, while also clarifying the effect of cooling conditions.
A first observation with the scanning electron microscope provides insight into the microstructure at higher magnification, with particular attention to grain boundary morphology and the distribution of associated precipitates. Figure 3.34 shows a BSE image acquired at 20KX magnification. Thanks to the strong Z-contrast, it is possible to clearly distinguish the carbides, enabling a direct characterization of their distribution. The average size is $85.4 \pm 25.6$ nm, which is noticeably shifted toward smaller dimensions compared to the carbides observed in the HIP sample. This reduction in size provides evidence of the influence of the faster cooling rate, while the overall volume fraction remains approximately constant at 0.2%.
In Figure 3.33, a triple point is shown, allowing the simultaneous observation of three grain boundaries. In all cases, relatively larger $\gamma'$ precipitates can be seen decorating the grain boundaries. However, this phenomenon is not always directly associated with

the development of serrations: while in the right-hand and the bottom one boundaries serration features are visible, the top-left boundary appears straight, despite the presence of coarse $\gamma'$ particles.
In the same figure is also possible to do a first evaluation of the $\gamma'$ distribution and morphology, with some cuboidal particles dispersed in the matrix and some others that are finer and more rounded. It is noted that the space around the bigger cuboidal particles is "empty", ar at least with a lower concentration of fine $\gamma'$.

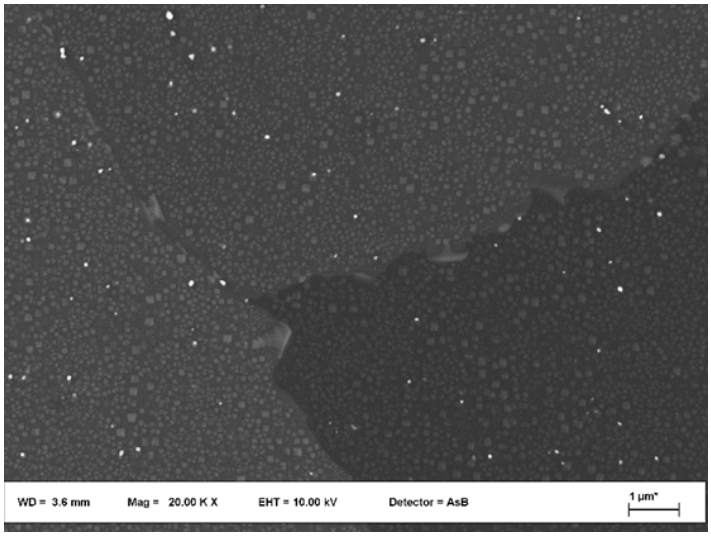


Figure 3.33: BSE image at 20 KX magnification to highlight grain boundaries; 1180°C sample

In Figure3.34 is provided a 100KX magnification of the sample, useful for a deep look at the $\gamma'$ morphology and distribution, since this phase is really fine.

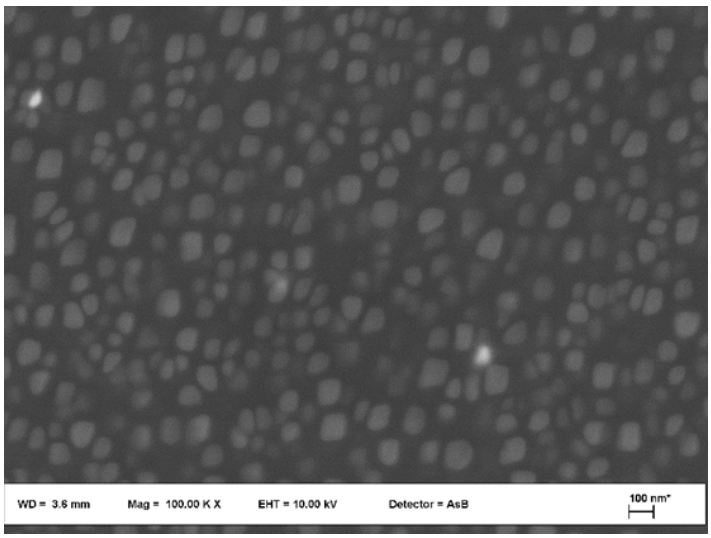


Figure 3.34: BSE image at 100 KX magnification to highlight $\gamma'$; 1180°C sample

To complete the characterization, Figure 3.35 reports the results from EBSD mapping and the Kernel Average Misorientation (KAM) map. As for the HIPed material, this temperature is enough to relief the residual stresses in the material, i.e. decrease of the KAM as shown in Figure3.35.

The IPF maps indicate a partial recovery from the as-built condition, with the average

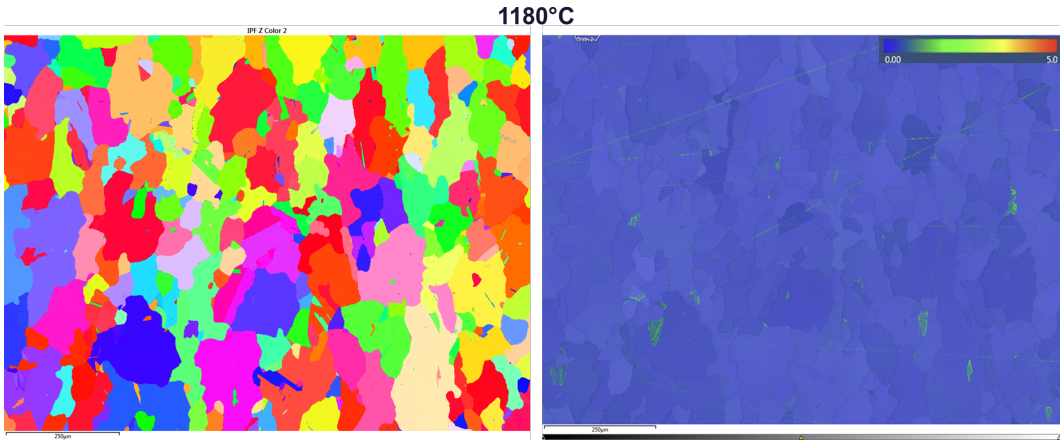


Figure 3.35: On the left the EBSD mapping in Inverse Pole Figure, on the right the KAM map;1180°C sample

grain dimension, expressed as FEMD, of $69.7 \pm 52.5$ µm. The aspect ratio distribution, shown together with the FEMD distribution, in Figure 3.35, exhibits an average value of $2.1 \pm 1.0$, with 66% of the grains falling within the range 1.1–2.0. This suggests a tendency towards equiaxed grain morphologies compared to the columnar structure of the as-built state. In combination with the SEM observations, these results highlight the role of solution heat treatment in promoting grain boundary mobility and local recrystallization.

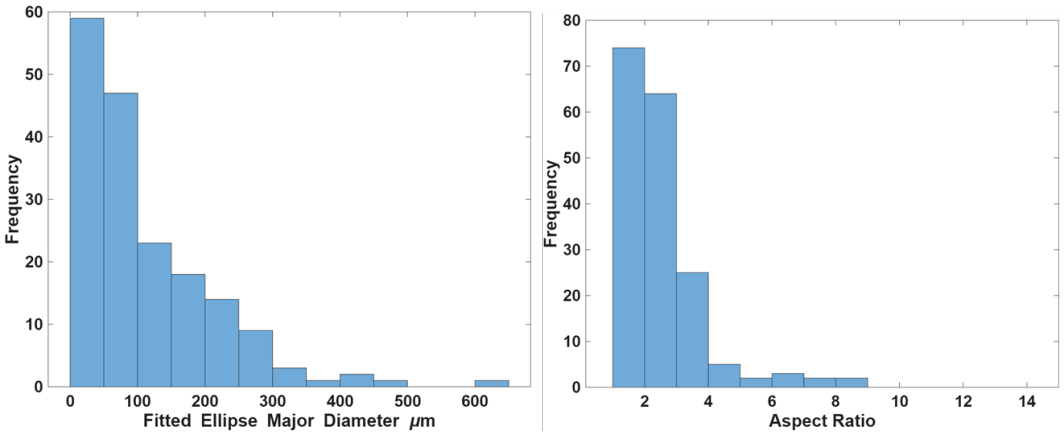


Figure 3.36: Distribution of the Fitted Ellipse Major Diameter and Aspect Ratio; .

### 3.4.3 Run – 1200°C - Characterization

The second run was carried out at 1200°C, with the furnace reaching a maximum temperature of 1206°C. As in the previous case, the first step of the characterization was performed with the scanning electron microscope, focusing on the morphology of the grain boundaries, the distribution of carbides, and the evolution of the $\gamma'$ precipitates. Figure 3.37 reports two representative BSE images that highlight some peculiar features of the microstructure.
In the left image, a grain boundary is visible: initially it runs parallel to the building direction and then turns perpendicular. The parallel segment appears relatively straight and is decorated by both carbides and coarser $\gamma'$ precipitates, which are larger than those observed within the grain interiors. In contrast, the perpendicular segment of the boundary exhibits a certain degree of serration, which appears to be associated with the presence of $\gamma'$ precipitates arranged in a fan-like morphology, or alternatively, with the formation of coarser $\gamma'$ particles localized along the boundary. Notably, in this serrated region no carbides are detected.
The right image in Figure 3.37 shows a straight grain boundary that deviates from its path only in the presence of a much larger $\gamma'$ particle, visible at the bottom of the micrograph. In this case, the carbides appear aligned in stripes along the building direction, suggesting that their distribution is mainly driven by solidification dynamics rather than by an interaction with the grain boundaries.

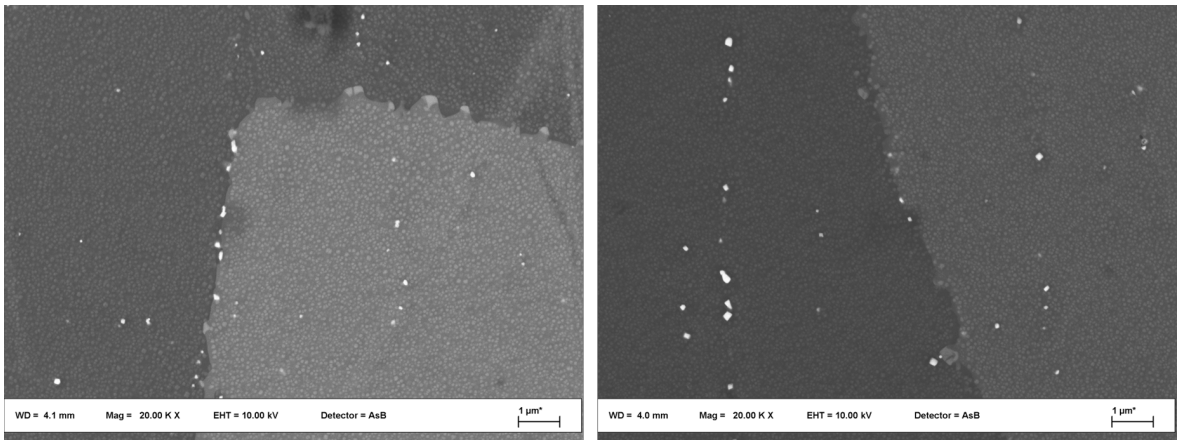


Figure 3.37: BSE images at 20 KX magnification to highlight grain boundaries; 1200°C sample

The average size of the carbides is $102.9 \pm 43.6$nm, while the volume fraction remains between 0.2% and 0.3%, although with a marked dependence on the specific location within the microstructure.
Again, the $\gamma'$ dimension is really fine, and to have a correct evaluation of the volume fraction is useful an image at high magnification, so is reported Figure3.38 with a 100KX magnification. The result, after imaging analysis with ImageJ software is a volume fraction of $\gamma'$ of 38%.

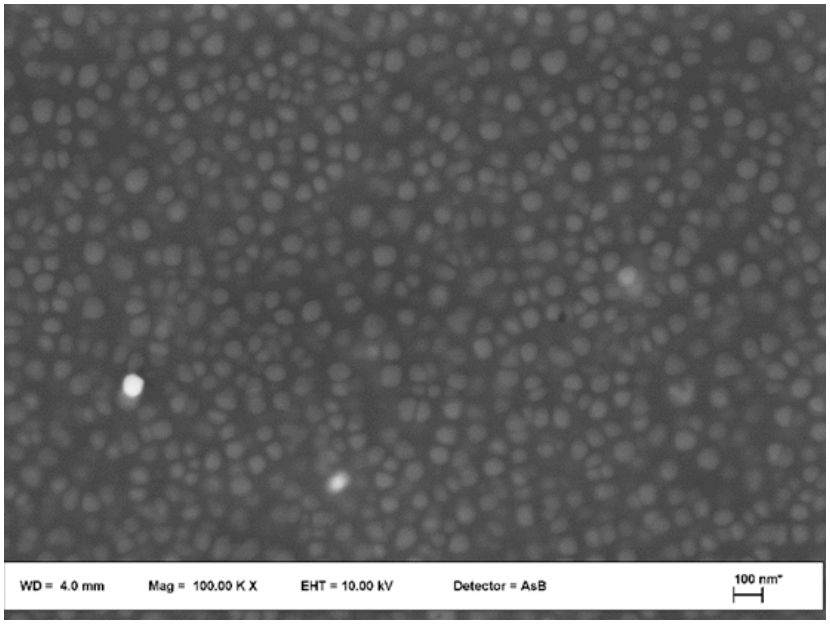


Figure 3.38: BSE image at 100 KX magnification to highlight $\gamma'$; 1200°C sample

Figure 3.39 reports the results from EBSD mapping of the 1200°C run. The average grain dimension, expressed as FEMD, is $96.9 \pm 83.1$ µm, with 51% of the grains falling within the range 30–100 µm; and the biggest grain has a FEMD of 543µm. The aspect ratio distribution shows an average value of $2.6 \pm 1.7$, with 46% of the grains lying in the range 1.1–2.1. Compared to the 1180°C condition, these results indicate a tendency towards coarser and more elongated grains, with a wider distribution of both FEMD and aspect ratio values. The increase in FEMD suggests a higher degree of grain growth promoted by the elevated soaking temperature, while the broader aspect ratio distribution points to a less uniform microstructural evolution. This condition may partially reduce the microstructural homogeneity achieved at 1180°C, and it indicates that grain boundary mobility becomes more pronounced at 1200°C.

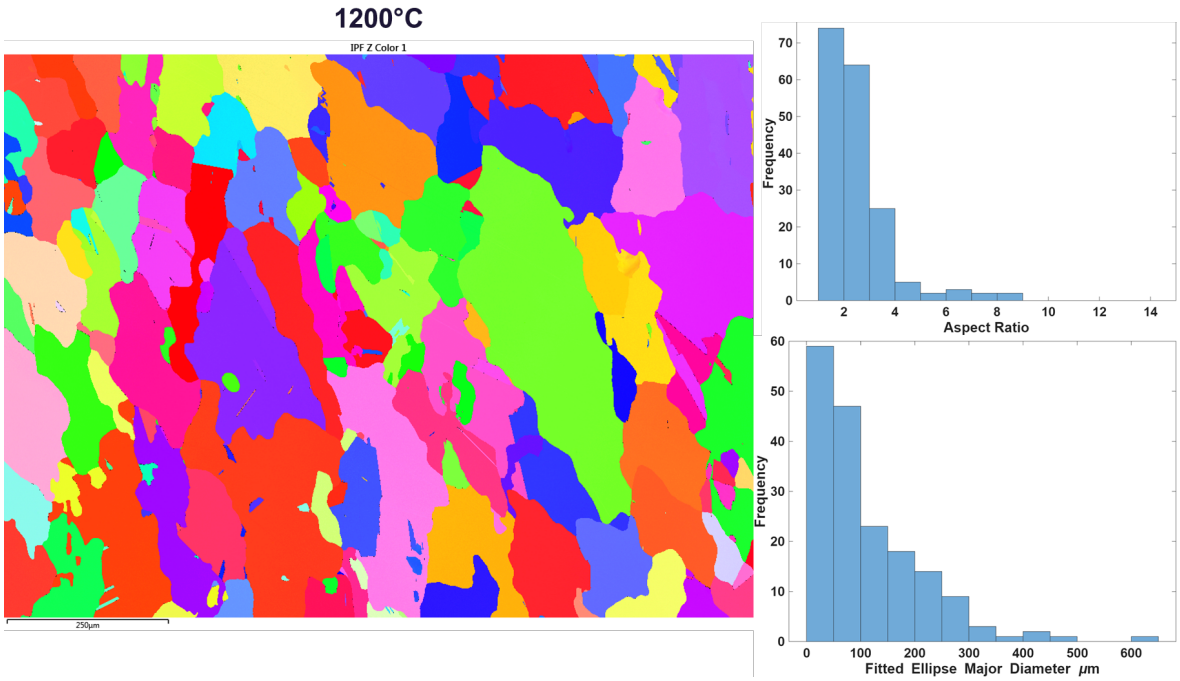


Figure 3.39: On the left the EBSD mapping in Inverse Pole Figure; on the top right the distribution of the Aspect Ratio and below the Fitted Ellipse Major Diameter distribution; 1200°C sample.

### 3.4.4 Run – 1220°C - Characterization

The third run was performed at 1220°C, with a maximum furnace temperature of 1224°C. The characterization strategy followed the same approach as in the previous runs, starting with imaging analysis using the SEM. Figure 3.40 shows two grain boundary at 20KX magnification, where both straight and serrated morphologies are visible.
The grain boundary on the right appears straight, without the presence of larger $\gamma'$ precipitates or carbides that could promote serration. In contrast, the boundary on the left exhibits deviations from a linear path, i.e., serration, which coincides with the presence of coarser $\gamma'$ particles. This observation reinforces the trend already noted for the SAM alloy: under these experimental conditions, serration is closely associated with the presence of larger $\gamma'$ precipitates, while carbides do not seem to play a significant role.
It is also worth noting that this sample underwent air quenching after solution annealing, with a cooling rate of approximately 367°C/min. The occurrence of serration is possible even under such rapid cooling conditions and that $\gamma'$ coarsening at the grain boundary is sufficient to trigger boundary segmental motion.
For what concerns the carbides the average dimension is found to be $158.8 \pm 59.0$.

To complete the characterization, EBSD mapping was carried out on the 1220°C sample (Figure 3.41). The inverse pole figure (IPF) maps show a further recovery from the as-built condition, with a grain structure comparable in morphology to the lower

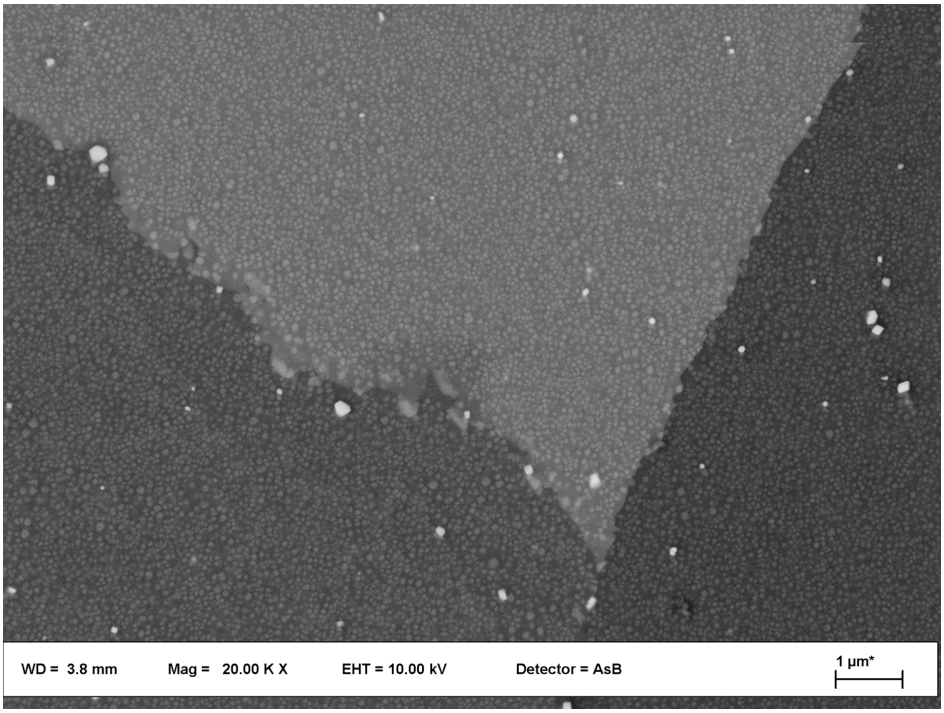


Figure 3.40: BSE image at 20 KX magnification to highlight grain boundaries; 1220°C sample

temperature runs but with slightly different statistical parameters. The average grain size, expressed as FEMD, is $81.5 \pm 63.0$ µm, with the largest detected grain reaching 367 µm. The distribution indicates that 52% of the grains fall within the range 30–100 µm, while a more detailed analysis shows that 21% are concentrated in the narrower 30–50 µm interval. This suggests that, compared with the 1200°C condition, the grain size distribution is somewhat less skewed towards very large grains, but still broader than at 1180°C. The aspect ratio distribution presents an average value of $2.4 \pm 1.6$, with 58% of grains lying between 1.1 and 2.1. Compared with the 1180°C sample ($2.1 \pm 1.0$), the values point to a slight increase in elongation, although the fraction of nearly equiaxed grains remains significant. Relative to the 1200°C condition ($2.6 \pm 1.7$), the 1220°C sample shows a moderate reduction of the average AR and a higher proportion of grains in the low-AR interval, suggesting that grain growth is not strictly monotonic with temperature, but affected by local variations and competitive growth processes.

The $\gamma'$ precipitates at this stage remain very fine, making high-magnification imaging necessary for a reliable evaluation of their volume fraction. For this purpose, Figure 3.42 reports a micrograph acquired at 100KX magnification. Image analysis performed with the *ImageJ* software provides a $\gamma'$ volume fraction of approximately 39%, it has be be stated that the resolution of the image is not optimized for imaging analysis and the result could be over-estimated.

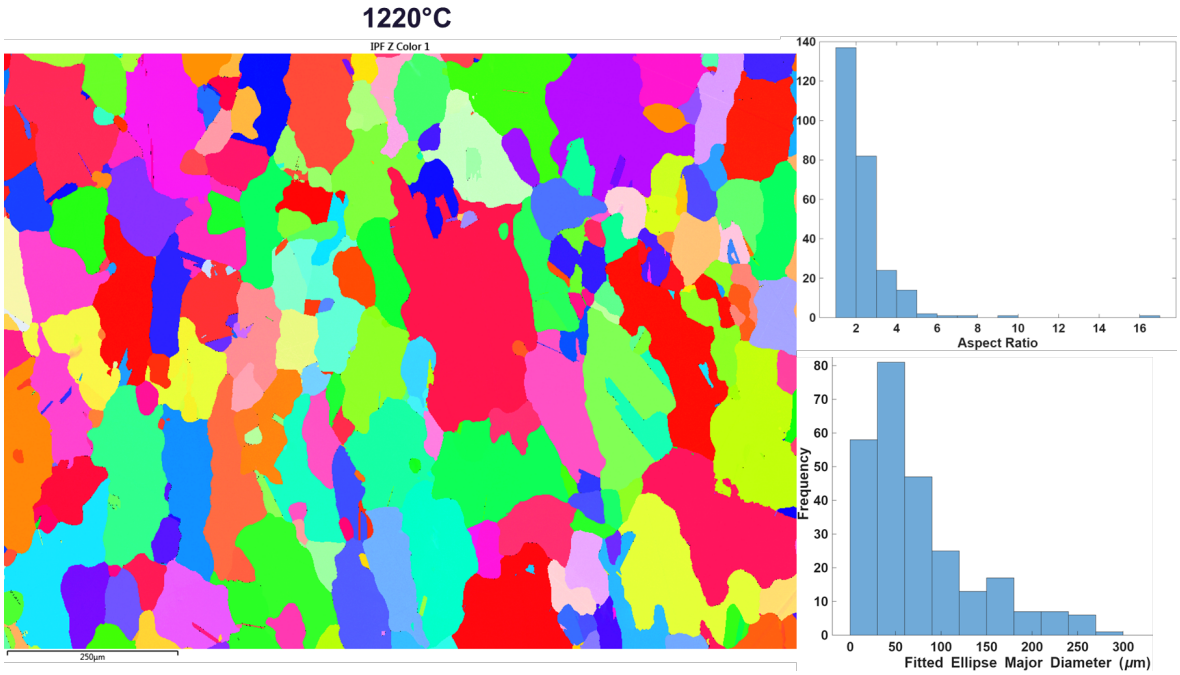


Figure 3.41: On the left the EBSD mapping in Inverse Pole Figure; on the top right the distribution of the Aspect Ratio and below the Fitted Ellipse Major Diameter distribution; 1220°C sample.

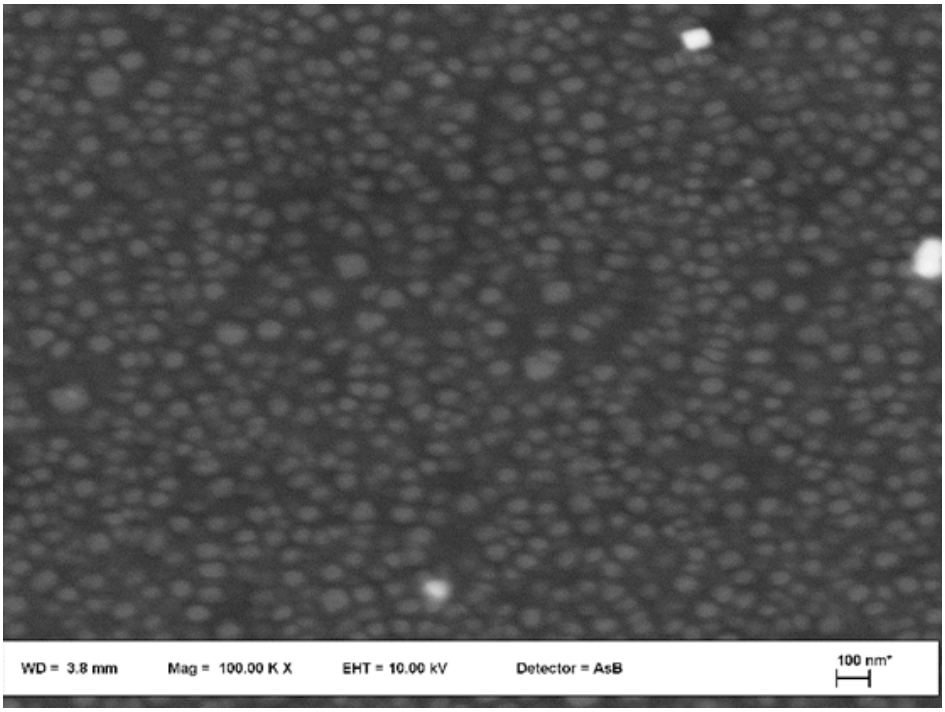


Figure 3.42: BSE image at 100 KX magnification to highlight $\gamma'$; 1220°C sample

### 3.4.5 Run – 1240°C – fast cooling - Characterization

The fourth run was conducted at 1240°C, with a maximum furnace temperature of 1244°C. The characterization strategy again started with SEM imaging, allowing a direct comparison with the previous heat treatments and highlighting the combined effects of high-temperature solutioning and the subsequent air quench.
In Figure 3.43, an overview of the surface at 1KX magnification is shown, where a bright phase, mainly located at the grain boundaries is immediately visible. This feature was not observed in the earlier runs and represents a peculiarity that requires a deep investigation.

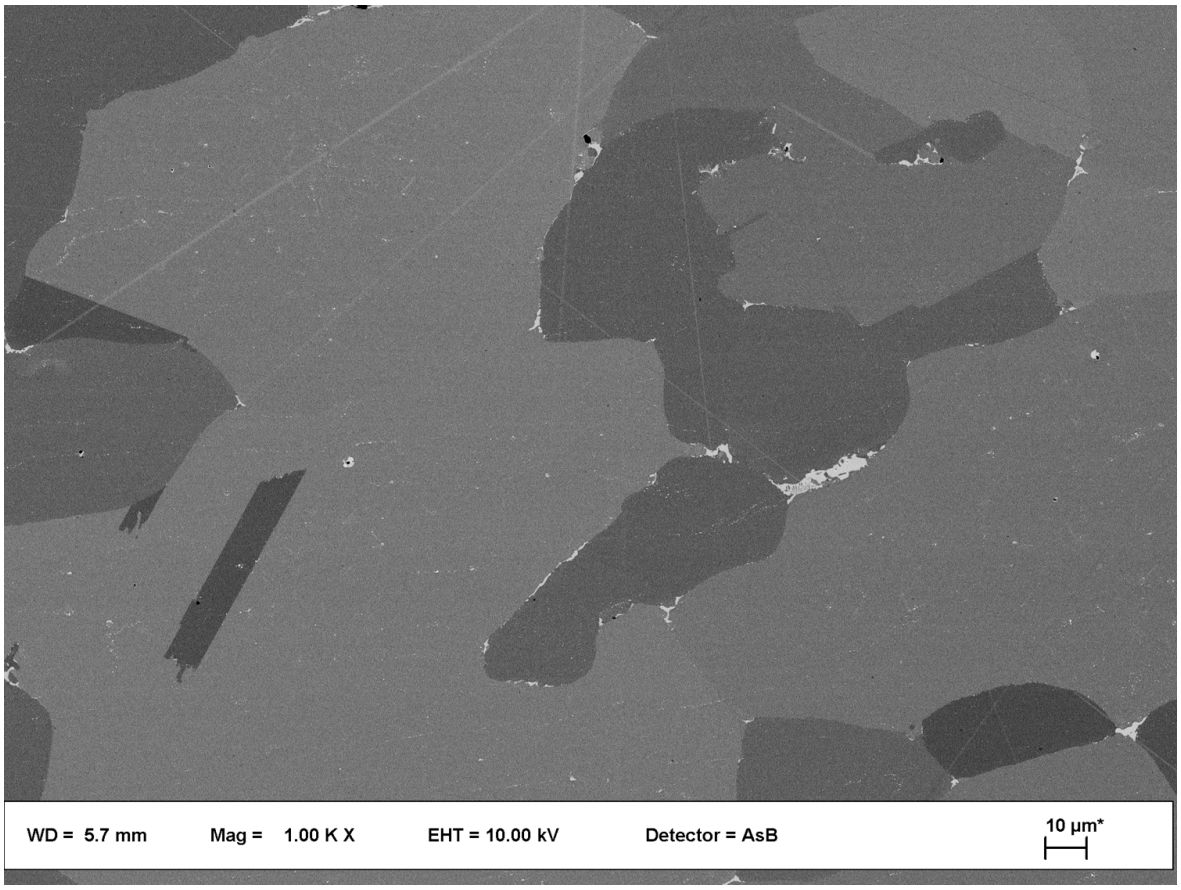


Figure 3.43: Overview of the surface at 1KX magnification with BSE to highlight the Z-contrast.

Figure 3.44 presents four examples of the different morphologies exhibited by this new, previously unreported phase (note that the magnifications differ among the images; each is indicated in the figure caption).Figure 3.44-A shows a "block" morphology with a length of 23µm, located between two grains. In Figure 3.44-B, the morphology appears as a continuous film along the grain boundary, with a total length of 48µm. Figures 3.44-C and D provide two additional examples of more complex morphologies, suggesting an intricate 3D structure within the material.

At higher magnification, additional features around this phase become visible, as shown in Figure 3.45. Here, a peculiar morphology of $\gamma'$ (or presumed $\gamma'$) is evident. In multiple locations, always surrounding the new unknown phase, a "dendritic-like" shape of $\gamma'$ is observed, indicating it may have formed through partial local melting and subsequent solidification. This finding suggest, as first instance a possible phenomena of incipient melting in the material (IM). The hypothesis of incipient melting (IM)

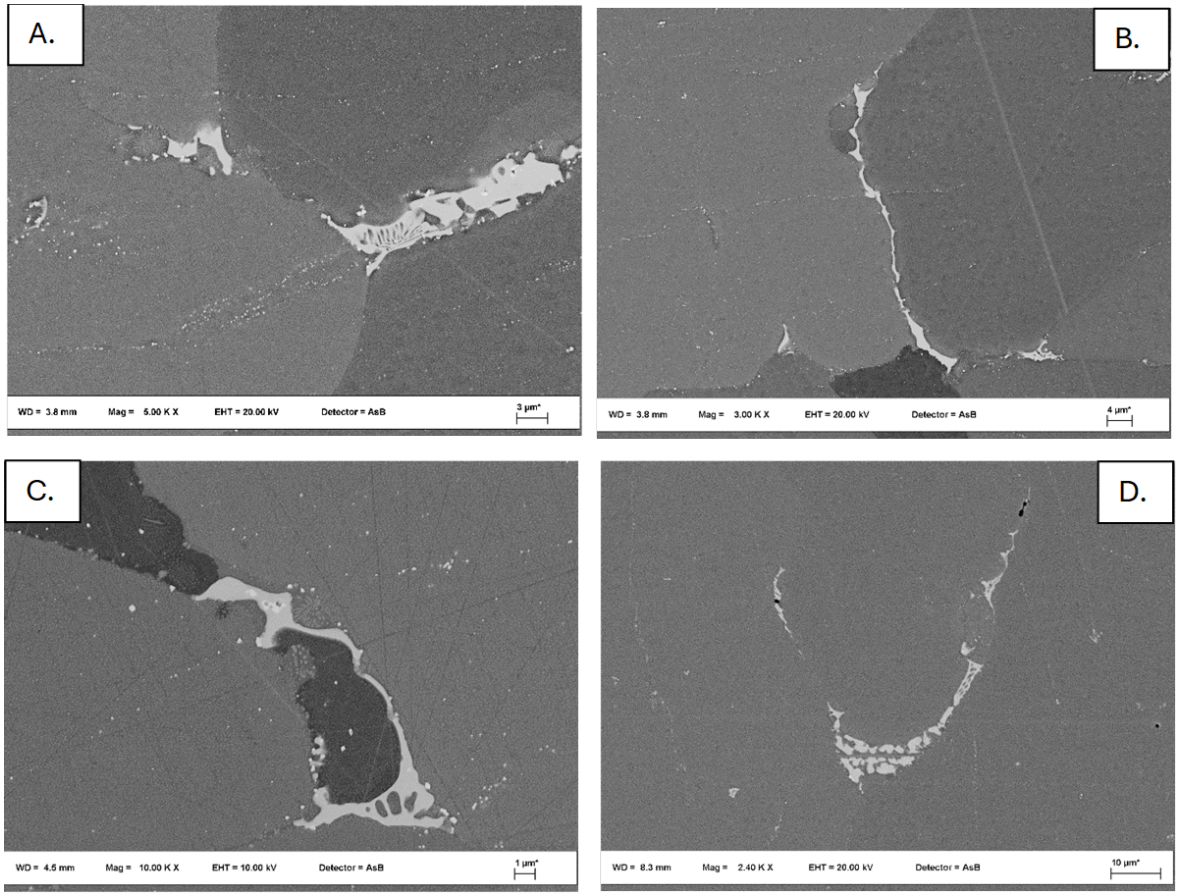


Figure 3.44: Unknown phase appeared at 1240°C in fast cooling condition, in A-B-C-D are provided some example, at different magnification, all with BSE detector.

is reinforced by the observation of porosity at grain boundaries, particularly at triple junctions. Two representative examples are shown in Figure 3.46, where pores are clearly visible at grain boundary intersections. In both cases, the porosity is partially surrounded by the newly identified phase, suggesting that liquid formation occurred locally during the high-temperature exposure and was subsequently trapped during cooling.

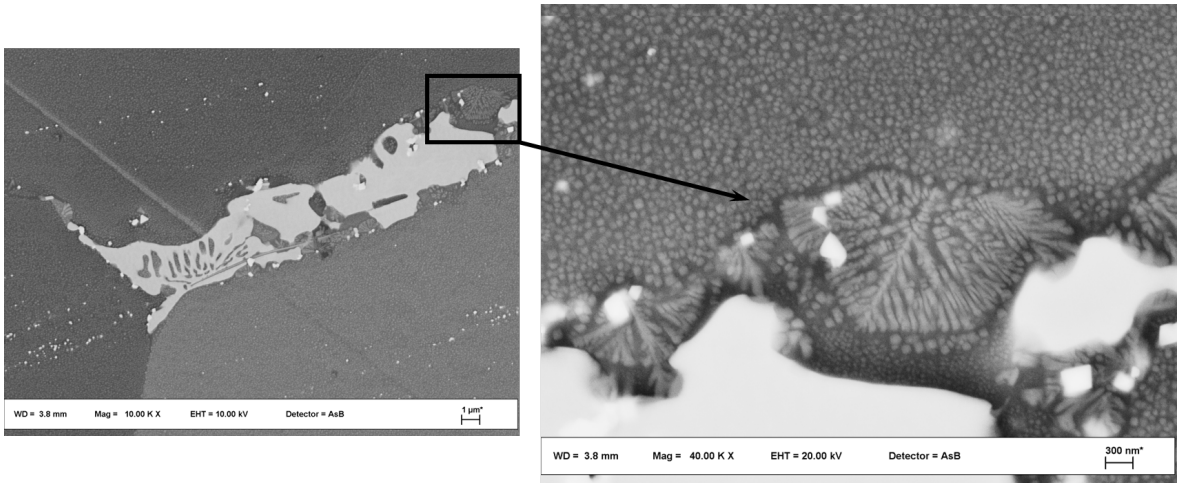


Figure 3.45: Dendritic shape of, presumed gamma prime phase around the unknown phase

It should be noted that the material subjected to the solution heat treatment was taken directly from the as-built condition, and therefore already contained a considerable amount of defects and porosity. This represents a limitation in the present analysis, since the pores observed at the grain boundaries could either be inherited from the building process, or alternatively result from incipient melting. A further possibility is that pre-existing porosity acted as preferential sites for the onset of localized melting, thereby coupling the two phenomena. To clearly uncouple these effects, additional dedicated investigations are required.

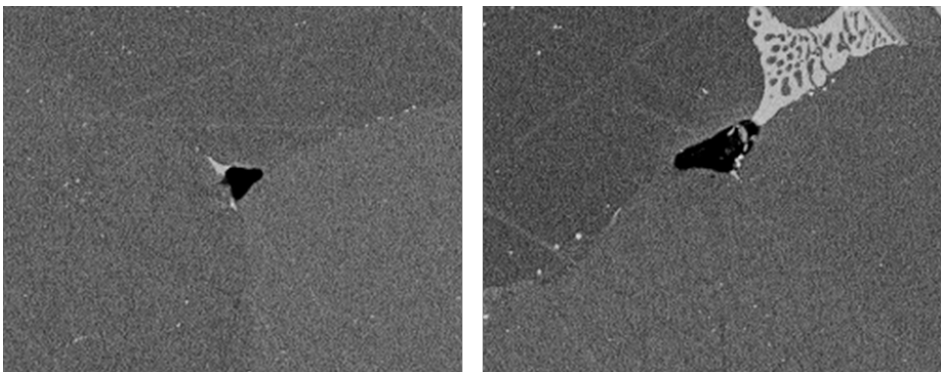

Figure 3.46: Presumed incipient melting phenomena at grain boundary triple point.

All previous images were taken with back scattered electrons, that present a contrast (Z-contrast) that is proportional to the atomic number. The fact that the new-phase is much brighter that the surrounding matrix suggest a big presence of element with high atomic number like hafnium and tantalum. A preliminary, and just qualitative EDS mapping was performed, and the result, showed in Figure3.47, suggest that the phase is enriched in nickel and hafnium.

Just looking at the image contrast in Figure**??**, is possible to notice a different shade of gray between the "dendritic" region and the $\gamma'$ phase inside the grain (likely not effected by the unknown phase). To better understand this variability in the composition in different point, a mapping in precise regions were performed with EDS detector, in particular in Figure3.48 are reported the precise sites of mapping. "*Site14*" is referred to the unknown phase, "*Site15*", "*Site16*" and "*Site18*" are related to the dendritic region, and "Site17" is inside the grain "far" from the new phase. The result of the chemical mapping are reported in Table3.12.

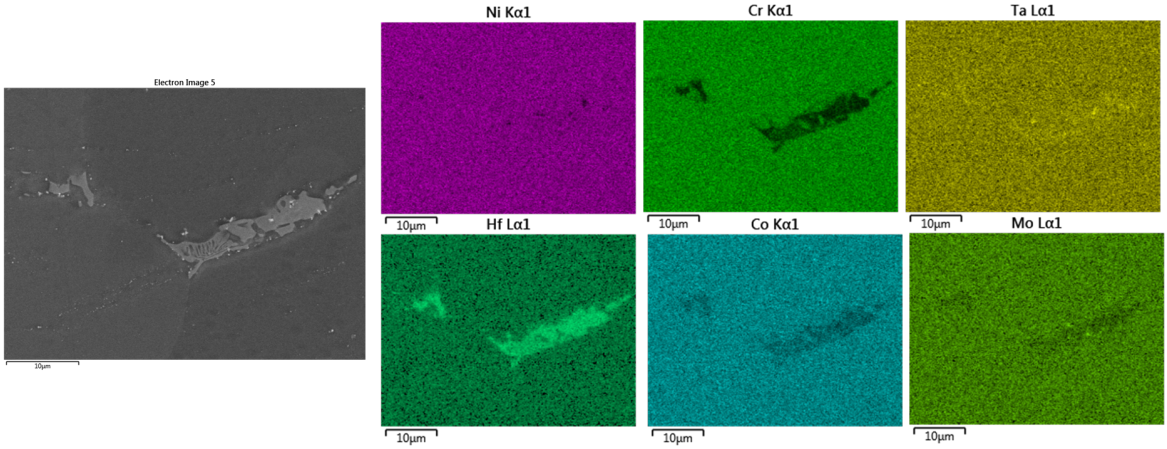


Figure 3.47: EDS mapping of a location with a block morphology of the bright phase; main elements are reported.

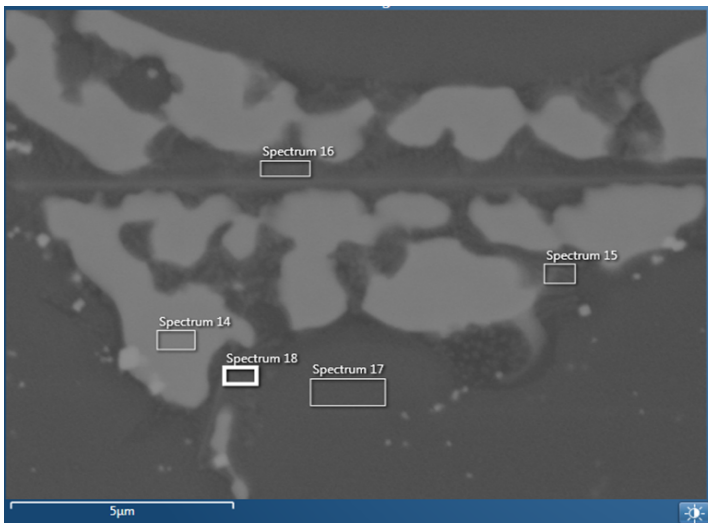


Figure 3.48: Particular of the unknown phase with labels of the sites where the EDS analysis was performed.

The current EDS mapping identifies a Hf-rich grain boundary phase that is chemically distinct from both matrix and interdendritic material. However, because of EDS limitations (peak overlap Hf/Ta, poor sensitivity to C and O and interaction-volume

Table 3.12: EDS composition mapping (wt.%) of different regions: new phase (Spec 14), matrix (Spec 17), and dendrites (Spec 15/18). Values are normalized to 100 wt.%.

| **Element** | **Spec 14 (new phase)** | **Spec 17 (matrix)** | **Spec 15/18 (dendrites)** |
|---|---|---|---|
| Ni | 39.55 | 42.93 | 42.74 |
| Hf | 27.83 | 1.82 | 14.20 |
| Ta | 10.16 | 9.74 | 9.46 |
| Co | 9.48 | 16.57 | 12.24 |
| C | 9.41 | 8.46 | 8.75 |
| Cr | 2.69 | 11.97 | 6.70 |
| Al | 0.72 | 2.74 | 2.82 |
| O | 0.16 | 0.23 | / |
| W | / | 3.22 | 1.35 |
| Mo | / | 2.31 | 1.75 |

mixing), the precise nature of this phase cannot be unambiguously determined from SEM-EDS alone; but is correct to state that the phase is likely to be an intermetallic phase enriched in Ni and Hf with traces of other elements.
The previous hypothesis of a different composition between the dendritic region and the matrix looks correct, with bigger discrepancy for the Hf content.

Despite the presence of the newly formed phase, EBSD mapping was nonetheless performed in order to assess whether recrystallization and grain growth were influenced by its occurrence at high temperature and subsequent retention after the air quench. Figure 3.49 shows, as in the previous cases, the EBSD results in Inverse Pole Figure (IPF) representation together with the distributions of aspect ratio and fitted ellipse major diameter (FEMD). It should be noted that, due to a positioning error of the specimen during acquisition, the building direction appears horizontal in this dataset. The statistical analysis indicates an average aspect ratio of 2.2±1.0, with approximately 60% of the grains lying between 1.1 and 2.2. The Fitted Ellipse Major Diameter distribution has an average grain size of $95.7 \pm 75.9\,\mu m$, with 43% of the grains falling within the 30–100 µm range. Compared to the previous solution treatments (1180–1220°C), the 1240°C condition does not show a a big deviation in average grain morphology, despite the higher temperature.

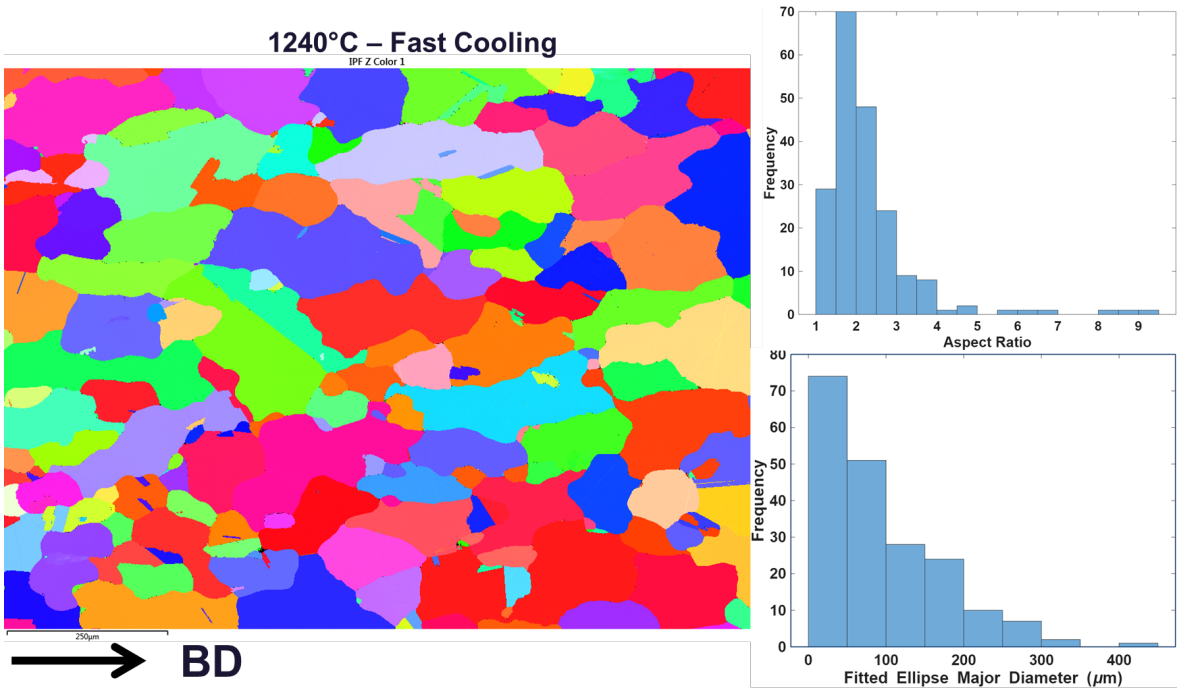


Figure 3.49: On the left the EBSD mapping in Inverse Pole Figure; on the top right the distribution of the Aspect Ratio and below the Fitted Ellipse Major Diameter distribution; 1240 ∘ C- Fast Cooling sample

### 3.4.6 Run – 1240°C – slow cooling - Characterization

To further investigate the nature and stability of the newly formed phase observed after the 1240°C solution with fast cooling, a second run was performed at the same temperature, but applying a slow cooling rate of approximately 5°C/min by switching off the furnace and leaving the sample inside. The objective of this test was to assess whether the phase could still be retained at room temperature under near-equilibrium cooling conditions. The overview of the surface at 1KX magnification (Figure 3.50) clearly shows that the phase is no longer present. This indicates that the compound forms at high temperature but is unstable at room temperature unless preserved through air quenching. Under fast cooling, the phase was retained in significant amounts and thus appears metastable, whereas during slow cooling it dissolves back into the matrix during the prolonged exposure to intermediate temperatures. This behavior strongly suggests that the phase is a transient high-temperature intermetallic, whose retention depends on kinetic constraints. In agreement with this interpretation, ThermoCalc equilibrium simulations did not predict its formation, reinforcing the hypothesis that the observed compound is a metastable product of non-equilibrium solidification/precipitation conditions. On the right side of Figure 3.50 is possible to notice the presence of ponderosities, in particular, ad in detail in Figure3.51 it' possible to see two different kinds of porosity; A-C are porosity at triple points, similar to those observed in the fast cooling conditions, while C, with a more rounded shape is probably a defect retained after the building process.

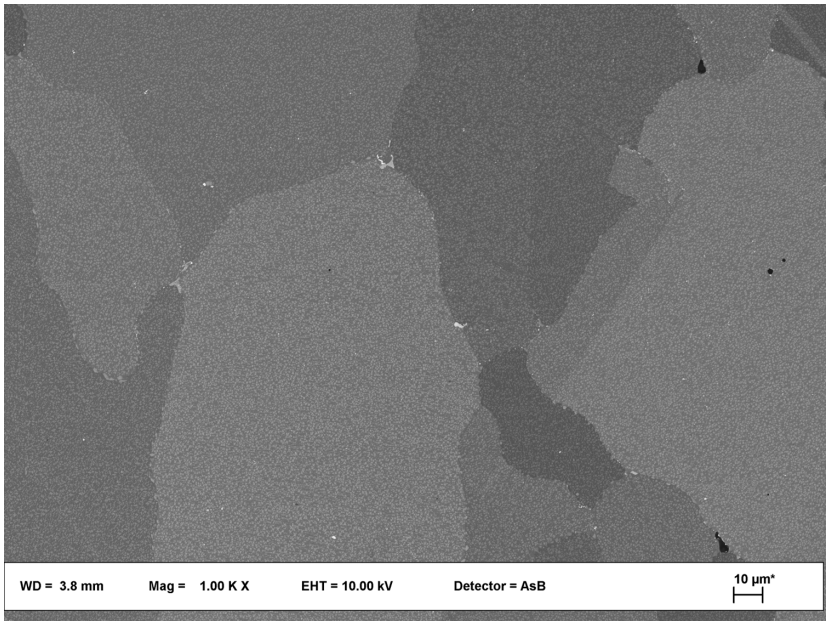


Figure 3.50: Overview of the material that went under slow cooling after the soaking at 1240°C.

The persistence of similar porosity under both fast and slow cooling conditions suggests that, at high temperature, a compound enriched in Ni and Hf forms, probably at grain boundaries and is directly associated with incipient melting phenomena. Under slow cooling conditions, however, there is sufficient time for solid-state diffusion to occur, allowing this transient phase to dissolve back into the surrounding matrix, which explains its absence at room temperature. ThermoCalc simulations indicate that among the principal alloying elements, hafnium exhibits the slowest diffusion kinetics. This statement, since the error related to TC simulations for this material must be supported by literature and is found that Hf is the element with highest tendency to segregate in the Ni-based materials i.e. slow diffusion rate [38].
Since the slow cooling conditions do not affect only the metastable compound but other features in the material, we expect other differences respect to the previous runs. Figure3.52 provides two example of grain boundaries found in the material, in the A image is clear the presence of larger $\gamma'$ particles, and related serration of the GB (low degree of serration but still present), while in the B image there is not a big difference in the $\gamma'$ dimension and the result is a straight GB.
An interesting feature is found in the Figure3.56 where, thanks to the Z-contrast is possible to notice a phase with a different gray shade respect to carbides and $\gamma'$. The hypothesis, likely not supported by an EDS mapping, is that it could be a M23C6-type carbide, something that was never noticed before.

To complete the characterization, EBSD mapping was also performed for this trial at 1240°C under slow cooling conditions, in order to evaluate potential differences in grain size and aspect ratio distribution. Figure 3.54 reports the Inverse Pole Figure (IPF) map together with the distributions of aspect ratio and Fitted Ellipse Major Diameter (FEMD).

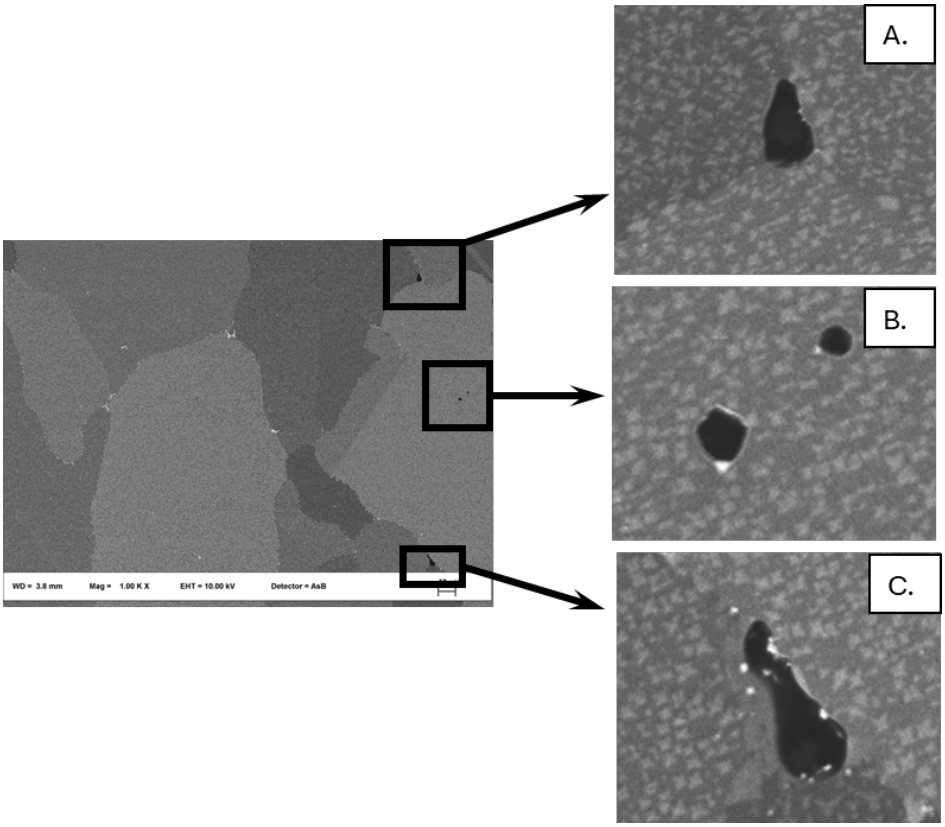


Figure 3.51: Details of different types of porosity reported in these conditions; A-C are related to Incipient Melting, B is retained from the printing process.

The average aspect ratio is $2.1 \pm 1.4$, with 68% of the grains falling in the range 1.1–2.1. The FEMD distribution shows an average value of $76.1 \pm 57.8$ $\mu$m, with 43% of the grains below 50 $\mu$m and 53% within the range 30–100 $\mu$m. The relatively high fraction of small grains, clearly visible also in the IPF map, suggests that the aspect ratio distribution in the lower range is strongly influenced by their presence, rather than being the result of a complete recovery process.

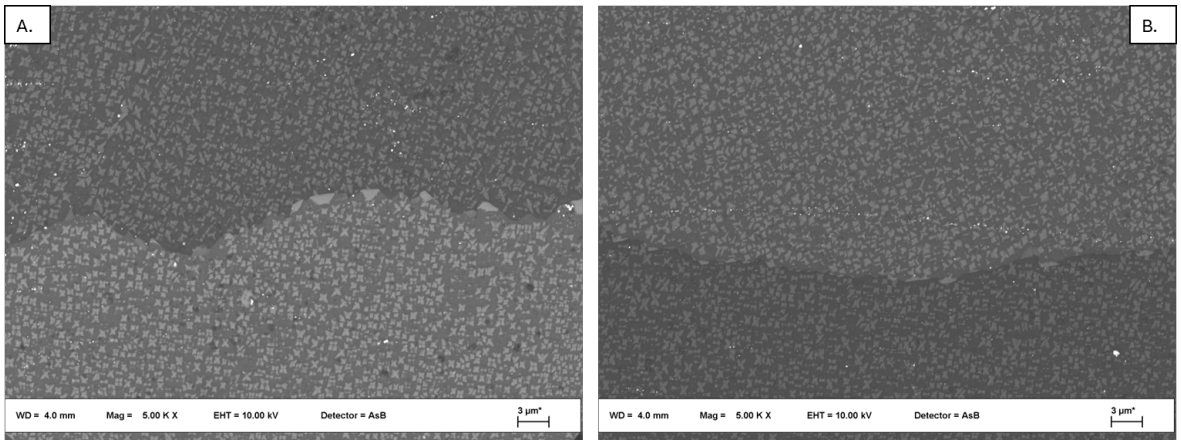


Figure 3.52: A and B are two examples of grain boundaries with different paths; BSE images of the 1240°C sample that went under slow cooling conditions.

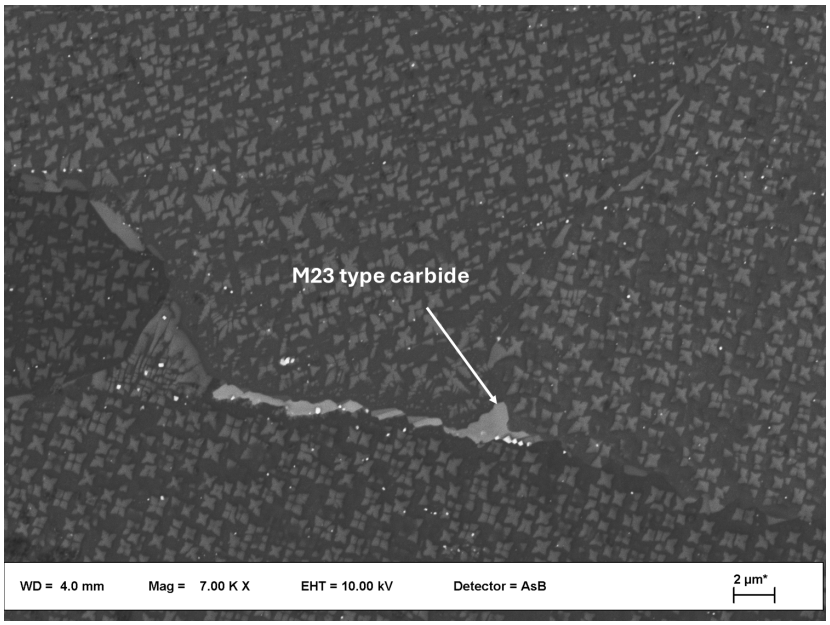


Figure 3.53: BSE image to highlight the different shades of gray and so the presence of a M23 carbide type.

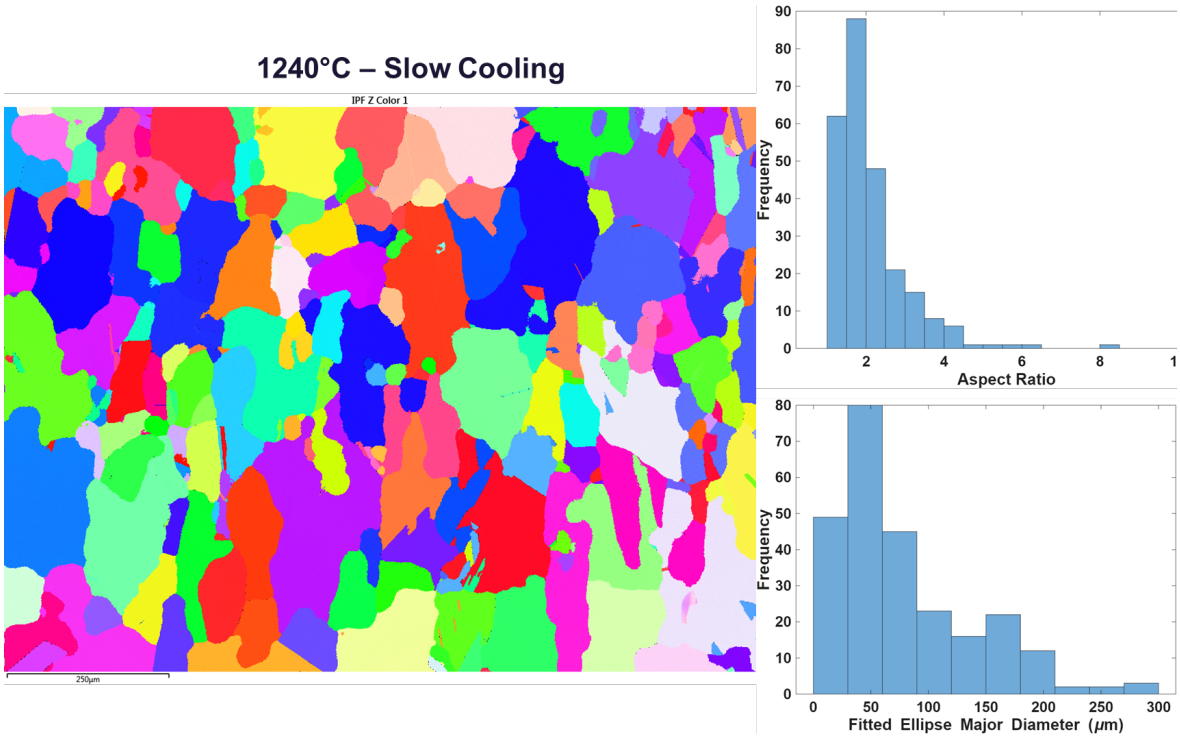


Figure 3.54: On the left the EBSD mapping in Inverse Pole Figure; on the top right the distribution of the Aspect Ratio and below the Fitted Ellipse Major Diameter distribution; 1240 ◦ C- Slow Cooling sample.

### 3.4.7 Run – 1260°C - Characterization

This temperature trial was repeated with the original setup, i.e. applying a fast cooling rate. Based on the results of the previous runs, a similar condition to the 1240°C fast-cooled treatment was expected. As shown in Figure3.55, this assumption is confirmed: the presence of the intermetallic compound is evident, even more pronounced than in the earlier trial, together with typical signatures of incipient melting, such as the dendritic morphology of the $\gamma'$ phase and porosity located at triple junctions.

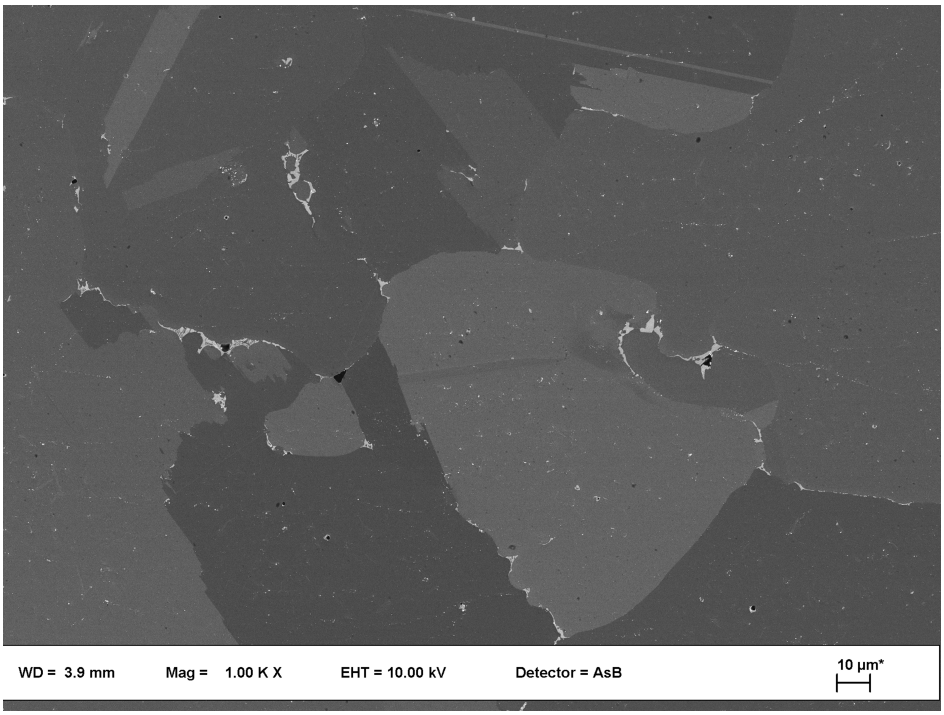


Figure 3.55: Overview of the material solutioned at 1260°C; presence of the intermetallic compound stable at high temperature.

In this case, despite the presence of incipient melting porosity, the EBSD run was performed anyway, to evaluate whether the temperature was sufficient to trigger extensive recrystallization. Figure **??** reports the Inverse Pole Figure (IPF) map together with the distributions of aspect ratio and Fitted Ellipse Major Diameter (FEMD).

The average aspect ratio is $2.2 \pm 1.0$, with 65% of the grains falling in the range between 1.1 and 2.1, indicating that the majority of grains remain relatively equiaxed. For the FEMD, the average value is $97.0 \pm 76.4\, \text{ţ}m$, with 48% of grains in the 30–100 µm range and 34% below 50 µm. This distribution suggests a heterogeneous grain size population, where a significant fraction of fine grains coexist with larger ones, consistent with partial recrystallization and grain growth processes at this high temperature.

It's worth to note that, after the removal of the sample from the furnace, it looked shiny respect to the previous runs where the external layer was opaque (Figure3.57. In this case the oxide layer looks thicker and easily spall off the sample while at lower temperature treatments the oxide was more "consistent". This thesis work did not focused on oxidation properties of the SAM alloy so this is just reported as an observation.

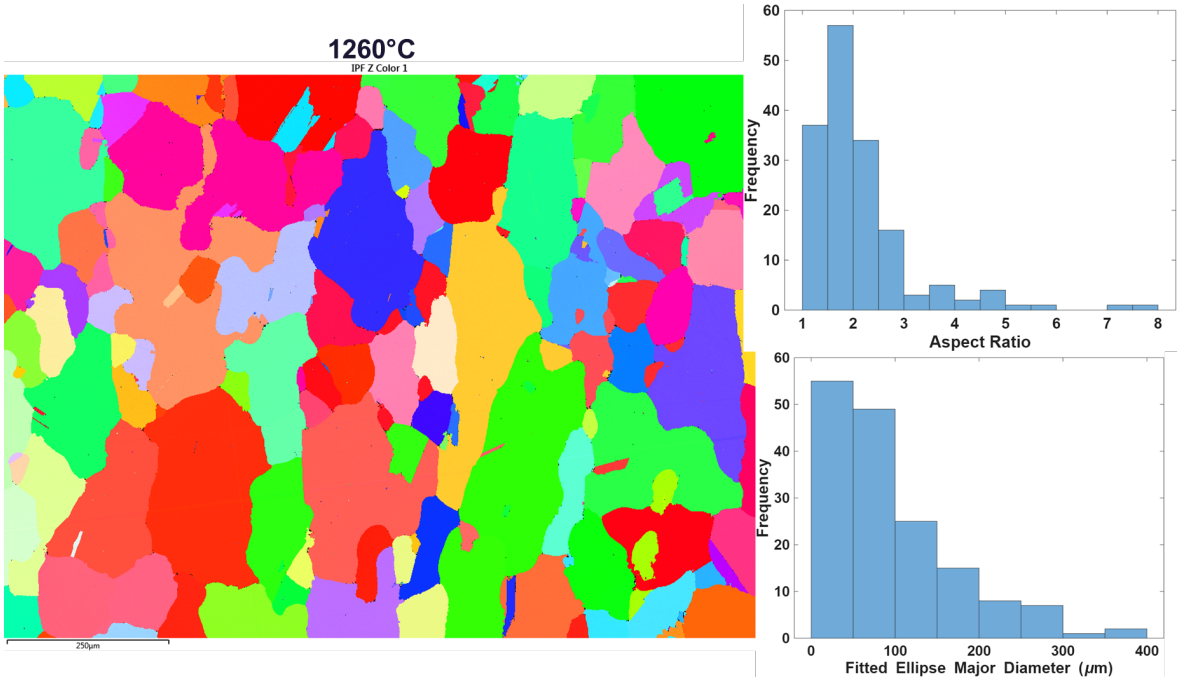


Figure 3.56: On the left the EBSD mapping in Inverse Pole Figure; on the top right the distribution of the Aspect Ratio and below the Fitted Ellipse Major Diameter distribution; 1260°C sample.

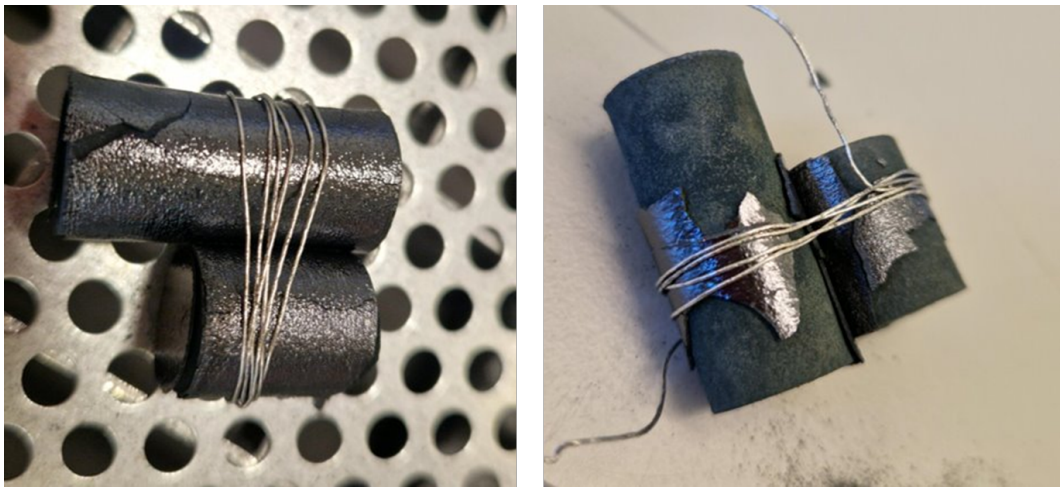

Figure 3.57: Sample look once it was removed from the furnace after the 1260°C treatment.

### 3.4.8 Run – 1280°C - Characterization

As a final trial, the solution temperature was increased to 1280°C in order to evaluate whether the material was approaching its actual melting point; the maximum temperature reached was actually 1286°C.
It is important to note that, at this stage of the thesis work, the DSC results were not yet available; consequently, the solution trials were conducted in a "blind" manner, without the guidance of DSC results. At this temperature the material went into the liquid phase, even over the incipient melting phenomena, as illustrated in Figure3.58 where a lot of porosity is retained.

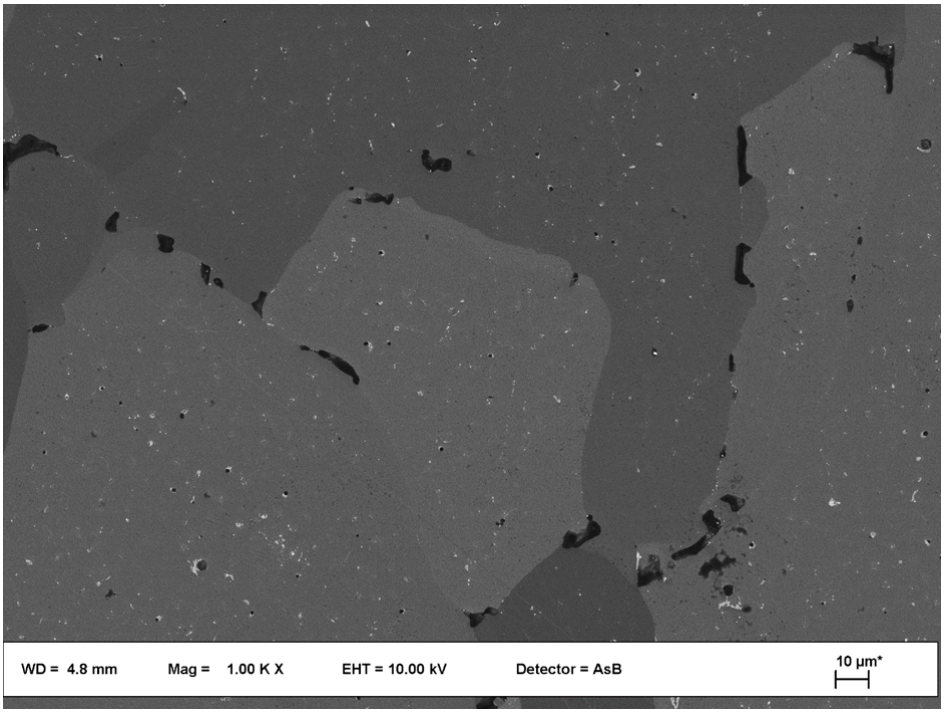


Figure 3.58: Extensive melt regions in the material after treatment at 1280°C

### 3.4.9 Crystallographic evolution and resume of main results

In this section is provided a resume of the main findings after the solution heat treatment performed at: 1180°C, 1200°C, 1220°C, 1240°C (slow cooling and fast cooling), 1260°C and 1280°C. At first instance is provided the direct comparison of the Inverse Pole Figure mapping for all the solution treatment trials (Figure3.59. Other useful information to resume the results and make a comparison are provided in Table3.13, where is reported a resume of the evolution of aspect ratio, grain dimension (expressed as Fitted Ellipse Major Diameter) and a carbide evaluation.

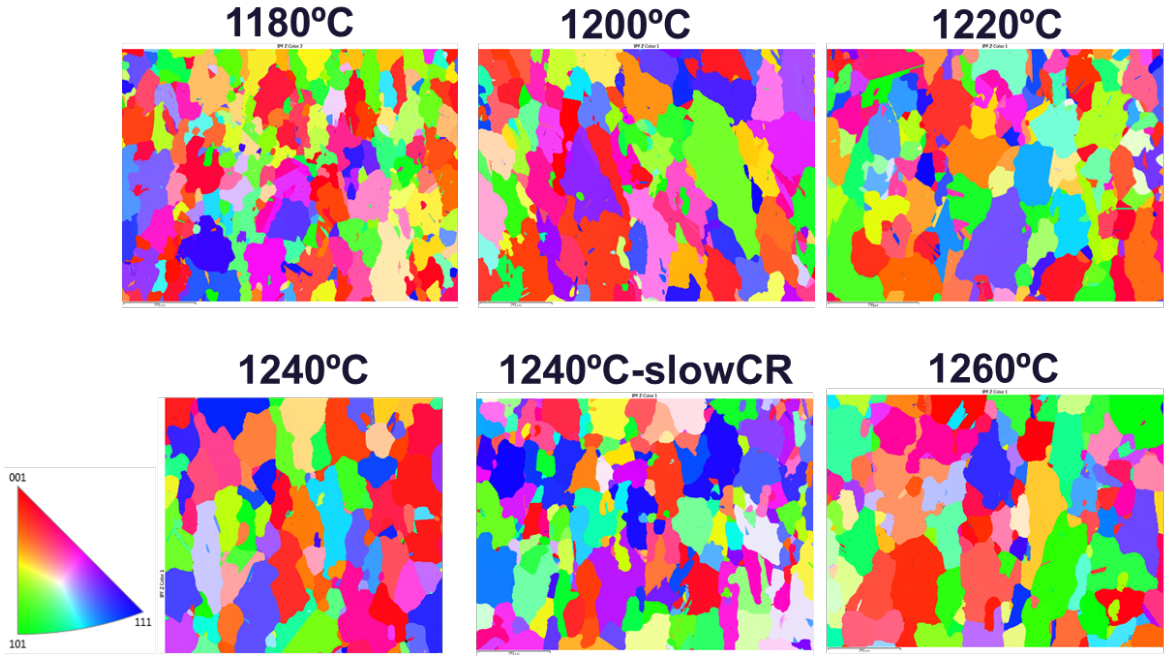


Figure 3.59: EBSD mapping in IPF evolution for the different solution temperature trials.

In Figure3.60 are plotted the cumulative distribution functions for all the temperature trials, comparing the result with the results regarding the preliminary heat treatment characterized in 3.3 and labeled ad "*FHT-1st*".
The plots for the preliminary heat treatment (where the main changes happened after the HIP at 1180°C) almost overlap, for both AR and FEMD with the results of the solution trial performed at 1180°C. This comparable results suggest that there is no much influence of the cooling rate for what concerns the recrystallization and recovery, the cooling rate after HIP was around 10°C/min while for the solution step was >300°C/min.
The plots regarding the FEMD shows almost an overlap for the 1200°C, 1240°C (fast cooling) and the 1260°C; the 1220°C is slightly shifted towards smaller value of fitted diameter.

Table 3.13: Summary of crystallographic and microstructural parameters for the different heat treatments.

| **Condition** | **AR** | **FEMD** [$\mu$**m**] | **Carb. frac. [%]** | **Carb. size [nm]** | **Comment** |
|---|---|---|---|---|---|
| FHT/1st | $2.23 \pm 1.21$ | $84.3 \pm 64.9$ | 0.2 | $\sim 229.5$ | Planar $\gamma'$ at GB; no serration |
| 1180°C (fast) | $2.1 \pm 1.0$ | $69.7 \pm 52.5$ | 0.2–0.3 | ∼85 | Recovery from AB state; grains moderately equiaxed. |
| 1200°C (fast) | $2.6 \pm 1.7$ | $96.9 \pm 83.1$ | 0.2–0.3 | ∼103 | Grain growth; broader AR distribution. |
| 1220°C (fast) | $2.4 \pm 1.6$ | $81.5 \pm 63.0$ | 0.2–0.3 | ∼156 | Mixed grain population; $\gamma'$ limited coarsening. |
| 1240°C (fast) | $2.2 \pm 1.0$ | $95.7 \pm 75.9$ | N.A. | – | Intermetallic phase + incipient melting. |
| 1240°C (slow) | $2.1 \pm 1.4$ | $76.1 \pm 57.8$ | N.A. | – | Phase disappears; fine grains due to recryst. |
| 1260°C (fast) | $2.2 \pm 1.0$ | $97.0 \pm 76.4$ | N.A. | – | Stronger incipient melting; partial recrystallization. |

At the same time the temperature that shows a distributions of aspect ratio shifted to the unity value are the 1180°C, 1240°C in both cooling conditions, and the 1260°C. The trial that shows a distribution shifted to higher values of aspect ratio is the 1200°C, that, at the same time, is the one that presented larger grains. This combination suggest a preferential growth along the building direction respect to a broader grain.

At 1180°C, the microstructure shows mainly recovery, with moderate grain equiaxiality and fine carbides. The 1200°C and 1220°C treatments promote grain growth and a wider aspect ratio distribution, although $\gamma'$ coarsening remains limited.

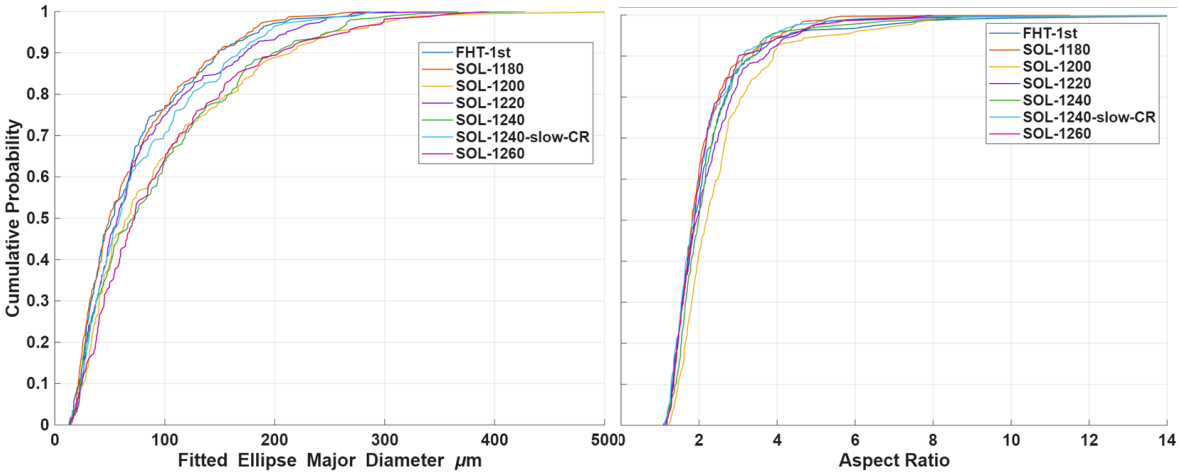


Figure 3.60: On the left, the CDF of the FEMD, on the right the distribution of the AR for all the solution trials; comparison with the preliminary heat treatment results: FHT-1st.

The 1240°C runs reveal a critical transition: under fast cooling, an intermetallic phase related to incipient melting forms, while slow cooling suppresses its retention at room temperature and favors the persistence of finer grains, likely due to recovery and localized recrystallization. Finally, the 1260°C treatment drives further incipient melting features, with evidence of partial recrystallization, suggesting that this temperature approaches the upper limit of thermal stability for the alloy.

## 3.5 Hardness

The result of hardness test presented in 3.3.8 have been "updated" by adding the result of HV10 test also for the solution runs, to see if there is a trend of hardness related to the temperature. In Table3.14 are reported the result of all the solution runs comparing with the full heat treated conditions of the SAM alloy after the preliminary heat treatment and the competitive alloy already presented previously, IN939 and STAL15, both in heat treated condition. The hardness results are also illustrated in Figure 3.61, and show a clear differences between the reference heat treated materials and the various solution heat treatment trials. Among the competitive alloys, IN939 exhibits the highest hardness (469 HV10), consistent with its higher $\gamma'$ fraction and strong solid-solution strengthening, while STAL15 records the lowest value (374 HV10).
For the solution trials, hardness values generally remain in the range of 409–427 HV10, with only minor variations as a function of temperature. A gradual increase from 1180°C (409 HV10) up to 1240°C fast cooling (427 HV10) suggests that increasing temperature up to this point favors precipitation strengthening and recovery effects. However, the 1240°C slow cooling condition stands out with a pronounced drop in hardness (385 HV10), likely due to coarsening of $\gamma'$ and reduced effectiveness of precipitation hardening.
At 1260°C, the hardness (416 HV10) recovers to intermediate values, indicating that the detrimental effect observed at 1240°C slow is not solely due to temperature but strongly related to the cooling rate and associated microstructural evolution.

Table 3.14: Hardness results (HV10) for different samples and heat treatment conditions.

| **Sample** | **HV10** | **Std. Dev.** |
|---|---|---|
| FHT-SAM | 411 | 11.7 |
| FHT-IN939 | 469 | 5.1 |
| FHT-STAL15 | 374 | 6.2 |
| 1180°C | 409 | 4.9 |
| 1200°C | 422 | 7.1 |
| 1220°C | 425 | 5.0 |
| 1240°C fast | 427 | 5.7 |
| 1240°C slow | 385 | 11.3 |
| 1260°C | 416 | 9.6 |

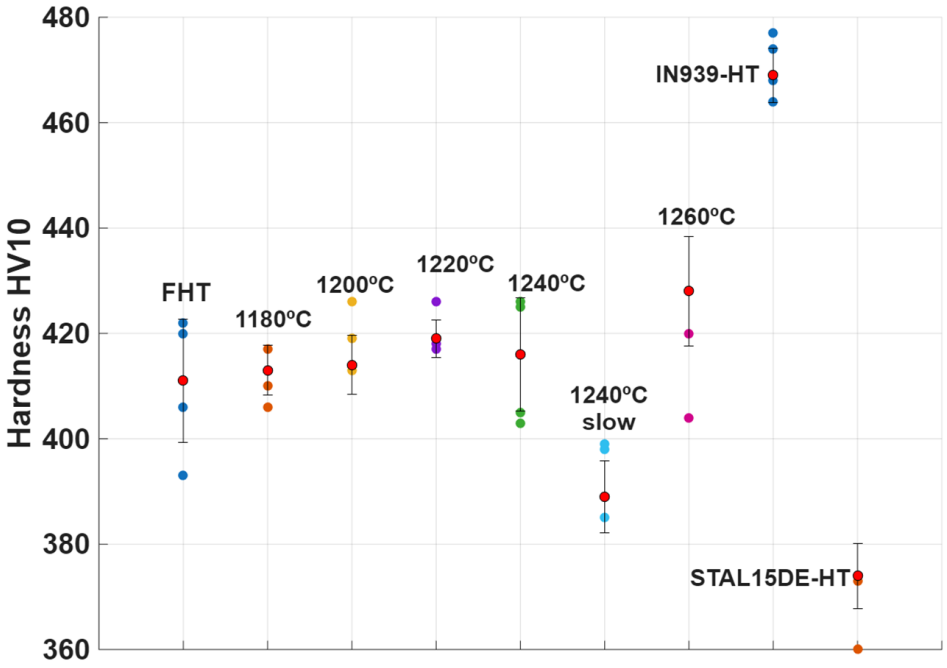


Figure 3.61: Hardness (HV10) results illustrated in a plot with error bar and average values. Evolution with increasing of solution temperature and comparison with competitive alloys.

## 3.6 DSC

The Differential Scanning Calorimetry (DSC) test was performed at the Polytechnic of Turin facility by Professor Emilio Bassini. The obtained results are analyzed and discussed here.
In order to achieve a precise analysis in the temperature range where phase transformations and precipitation events are expected, a two-step heating profile was applied. From room temperature to 1130°C, a relatively high heating rate of 20°C/min was applied; above this temperature, the heating rate was reduced to 5°C/min. As a result, the peak visible at 1130°C in Figure3.62 is related to the change in heating rate and not to any intrinsic transformation of the material. The reduction in heating rate is crucial to minimize segregation and micro-segregation effects, which are well known to influence the thermal response of nickel-based superalloys.

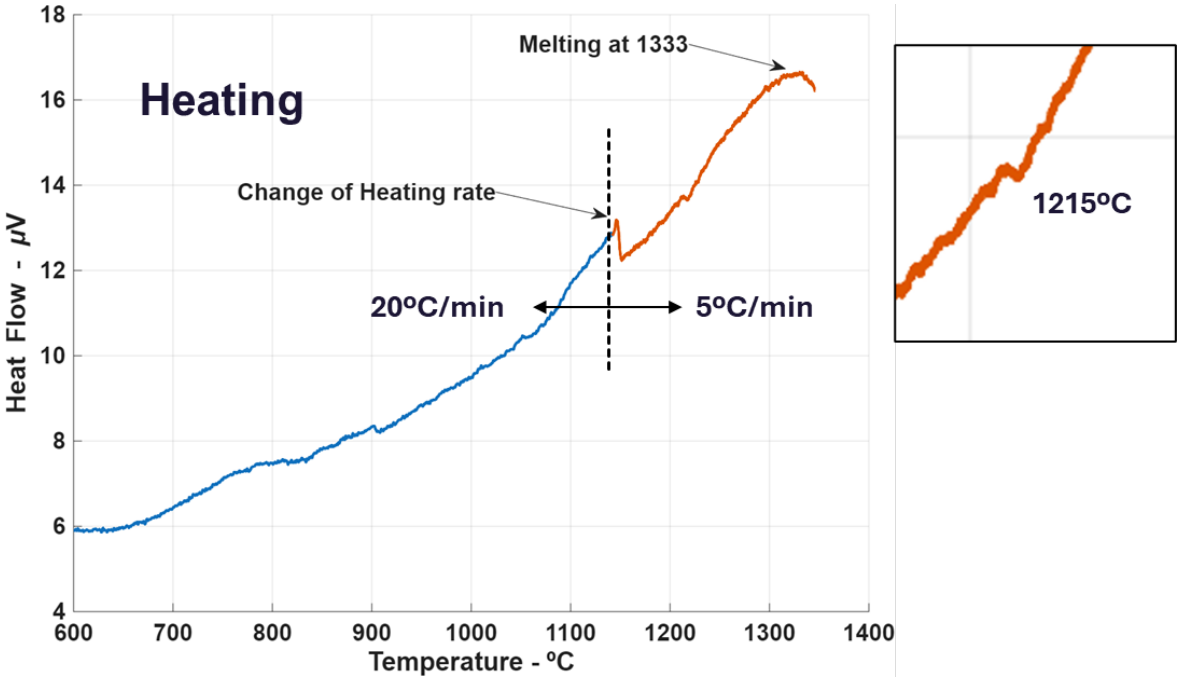


Figure 3.62: DSC results for the heating stage plotted in Temperature-Heat Flow graph.

Segregation in this context refers to the uneven distribution of alloying elements (e.g. Hf) during solidification or thermal treatment. Because these elements diffuse very slowly in the solid state, compositional gradients tend to persist at the microscale. If the heating rate is too high during DSC, these segregated regions may melt locally at lower temperatures than the bulk, leading to premature signals of incipient melting or an inaccurate determination of transformation temperatures.
The DSC results indicate melting at 1333°C. However, due to an instrumental issue, the endothermic peak is not fully closed, preventing a reliable calculation of the enthalpy of fusion ($\Delta H_{\text{fus}}$), i.e., the energy required to fully melt the sample. The rest of

the curve is mostly linear, with the exception of a very small event at 1215°C. Given the small peak area, it is not possible to determine a enthalpy value for this feature.
Interestingly, the DSC results do not fully align with the experimental evidence from the solution heat treatment trials. In the furnace tests, incipient melting was already observed at 1240°C and became more evident at 1260°C, while at 1280°C the material showed clear signs of bulk melting. This discrepancy may be related to the sensitivity of DSC measurements to sample size, geometry, and local chemical inhomogeneity, which can mask or shift the onset of incipient melting compared to bulk-scale observations.
It is also worth noting that both the DSC tests and the furnace heat treatments were conducted with comparable heating rates (∼5°C/min) in the high-temperature range approaching the melting point.
From the cooling curve reported in Figure3.63, no significant heat-flow variations were detected in correspondence with carbide precipitation, or better were it is expected. This observation suggests that, although carbides are clearly visible in the microstructural analysis after heat treatment, their precipitation does not produce a signal strong enough to be detected by DSC. This is consistent with the fact that the overall volume fraction of carbides in this alloy is relatively low (on the order of 0.2–0.3%).
On the other hand, the precipitation of the $\gamma'$ phase is detectable. In the cooling curve, an exothermic event is observed in the range between 950°C and 1050°C, which corresponds to the precipitation of secondary $\gamma'$ particles.
In summary, while carbide precipitation remains "silent", in the DSC curve due to its low fraction and probably extended kinetics, the $\gamma'$ phase shows a clear signal in the range 950–1050°C.

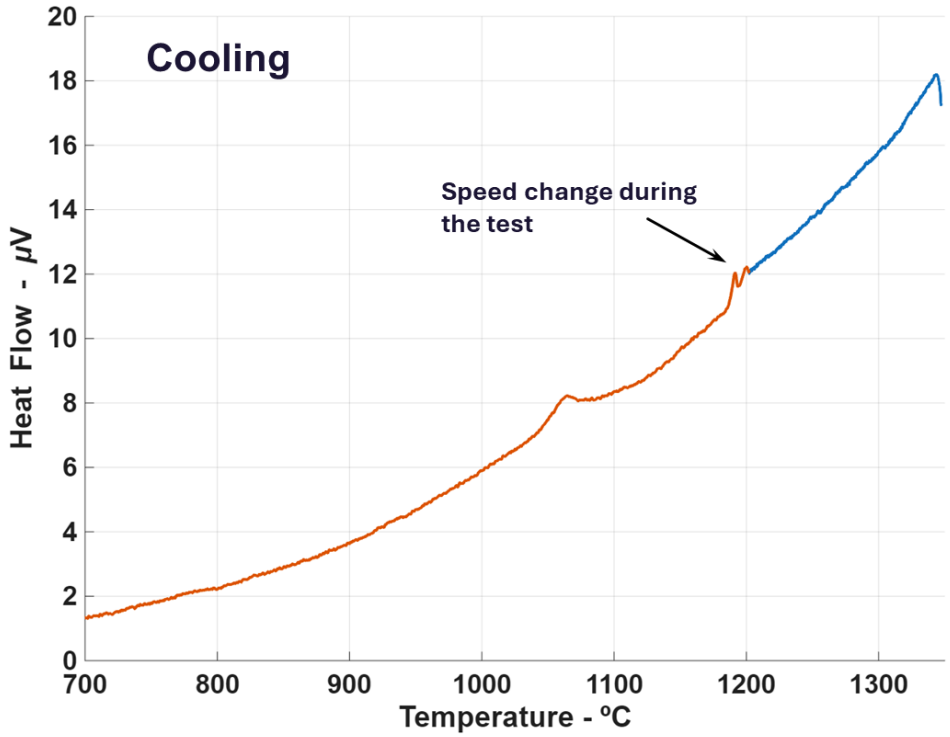


Figure 3.63: DSC results for the cooling stage plotted in Temperature-Heat Flow graph.

# Chapter 4

# Conclusion and Future Work

This thesis investigated the thermal response of the SAM alloy, focusing on the preliminary heat treatments and an extensive campaign of solution heat treatments, with particular attention to microstructural stability, grain growth, and secondary phase formation.

## Conclusions

**ThermoCalc simulations** represented a valuable initial support in predicting phase stability, but the limitations of the available thermodynamic database must be emphasized. Since the database is calibrated on commercial Ni-based superalloys, it did not accurately capture the peculiarities of the SAM composition, leading to discrepancies with the DSC and microscopy results. In the future, experimental data could be integrated into user-defined databases to improve predictive accuracy and establish a correction scheme tailored to this system.
**Preliminary heat treatments** (HIP + Solution + Aging) revealed that HIP at 1180 °C was sufficient to achieve densification and trigger recovery and partial recrystallization. Subsequent solutioning and aging stabilized the microstructure without notable grain growth, producing a more regular $\gamma'$ precipitation at grain boundaries and so losing the degree of serration reached after HIP. This baseline condition was the evidence of the need of a tailored heat treatment for the SAM.
**Hardness measurements** showed that SAM consistently reached values of 409–427 HV10 across solution trials, in line with the fully heat-treated condition (411 HV10). The main exception was the 1240 °C slow cooling condition, which dropped to 385 HV10, attributed to $\gamma'$ coarsening and reduced precipitation hardening. When compared to reference alloys, IN939 exhibited superior hardness (469 HV10) while STAL15 remained softer (374 HV10), confirming SAM's intermediate strengthening potential.
**Tensile testing** revealed strong anisotropy in the as-built condition, with lower stiffness and strength perpendicular to the building direction. After HIP + Solution + Aging, the anisotropy was markedly reduced, as Young's modulus and strength values converged between 0° and 90°. The post-processed SAM achieved significant increases in UTS (up to 1401 MPa), at the expense of reduced ductility, consistent with the

strengthening action of $\gamma'$ precipitation. This confirms the effectiveness of the full heat treatment in homogenizing microstructure and mechanical response. **Solution heat treatments** between 1180 °C and 1280 °C demonstrated distinct regimes of microstructural evolution:

- **1180 °C (fast)**: recovery dominated, with moderate grain equiaxiality and fine carbides. FEMD and AR overlapped with the HIP baseline, confirming negligible influence of cooling rate and pressure.
- **1200 °C (fast)**: noticeable grain growth with the largest FEMD values and a broader AR distribution, suggesting preferential elongation along the building direction.
- **1220 °C (fast)**: mixed grain population, limited $\gamma'$ coarsening, and FEMD slightly shifted towards smaller diameters.
- **1240 °C (fast)**: intermetallic phase formation related to incipient melting, with coarser grains retained.
- **1240 °C (slow)**: suppression of the intermetallic phase at room temperature, accompanied by localized recrystallization and finer grains, confirming the strong role of cooling rate.
- **1260 °C (fast)**: accentuated incipient melting with partial recrystallization, close to the upper thermal stability limit.
- **1280 °C (fast)**: stronger incipient melting, the material overcome the onset of the liquid phase, unsuitable for processing.

**Grain growth and aspect ratio (AR) evolution** followed clear trends:

- AR distributions shifted closer to 1.0 (equiaxed grains) at 1180 °C, 1240 °C (both cooling rates), and 1260 °C.
- At 1200 °C, AR was shifted towards higher values, coupled with larger grains, indicating preferential growth along the building direction.
- FEMD evolution was consistent across 1200 °C, 1240 °C (fast), and 1260 °C, while 1220 °C showed slightly smaller values.

**Case study at 1240 °C**: this condition highlighted the complex interplay between chemistry and processing. Fast cooling trapped the metastable phase, whereas slow cooling suppressed them and stabilized finer grains. This dual behavior demonstrates the importance of cooling strategy and sets a critical benchmark for future alloy optimization.

# Future Work

- **ThermoCalc refinement**: introduce DSC-derived corrections and experimentally informed parameters to improve prediction reliability for SAM.
- **Boundary serration control**: grain boundaries serration could be a powerful feature to enhance creep properties, under certain conditions it's possible to maintain this feature. The serration mechanism for the SAM needs deeper investigation, along with a proper method to quantify the serration amplitude.
- **1240 °C criticality**: explore the kinetic window where slow cooling promotes recrystallization without intermetallic retention, identifying industrially viable processing windows.
- **Onset of the metastable phase**: try to get more information from DSC, also an additional run at 1230ºC could give useful information, since we are blind in the range 1220°C – 1240°C.
- **Long-term aging**: creep, fatigue, and oxidation tests on selected conditions are for sure useful to validate microstructural stability under service conditions.
- **Real component**: the main limitation of the proposed setup for the solution step is the difficulty of transfer the same strategy to a real component; other strategies need to be investigated.

# List of Figures

# List of Tables

# Bibliography


[1] R. C. Reed. *The Superalloys: Fundamentals and Applications*. Cambridge University Press, Cambridge, 2006.

[2] Whittaker Mark T. Kolisnychenko Stanislav Coakley, James. 4. effect of temperature dropping during solution treatment in rejuvenation heat treatment and its long-term heating simulation on microstructures of nickel base alloy, udimet 520, 2020.

[3] T. M. Pollock and S. Tin. Nickel-based superalloys for advanced turbine engines: Chemistry, microstructure and properties. *Journal of Propulsion and Power*, 22(2):361–374, 2006.

[4] U. Glatzel, F. Schleifer, C. Gadelmeier, F. Krieg, and M. Müller. Quantification of solid solution strengthening and internal stresses through creep testing of ni-containing single crystals at 980 °c. *Metals*, 11(7):1130, 2021.

[5] Z. Yu, W. Zhang, Y. Zhao, and Y. Zhou. Review of $\gamma'$ rafting behavior in nickel-based superalloys. *Crystals*, 10(12):1127, 2020.

[6] C. T. Sims, N. S. Stoloff, and W. C. Hagel. Superalloys ii. *Wiley-Interscience*, 1987. Classic reference with extensive coverage of TCP phases.

[7] M. J. Kaufman and J. F. Radavich. The role of tcp phases in modern superalloys. *Superalloys 2000*, pages 481–490, 2000.

[8] A. Sato, H. Harada, Y. Koizumi, T. Kobayashi, T. Yokokawa, and Y. Murakami. The effects of re and ru on the phase stability of ni-base single-crystal superalloys. *Metallurgical and Materials Transactions A*, 37:1679–1684, 2006.

[9] Xinbao Zhao Yuan Cheng. The overview of the formation mechanisms of topologically close-packed phases in ni-based single crystal superalloys. *Journal of Phase Equilibria and Diffusion*, 39:762–773, 2018.

[10] P. Caron and T. Khan. Evolution of ni-based superalloys in aeronautics and space. *Aerospace Science and Technology*, 3(8):513–523, 2001.

[11] A. Sato, H. Harada, Y. Koizumi, and T. Kobayashi. Ttt diagram for tcp phases precipitation of 4th generation ni-base superalloys. *Superalloys 2012*, pages 17–26, 2012.

[12] Wenjun Han Runze Yu, Yijiala Yiliti. Microstructural evolution and its effect on the mechanical properties of a novel second-generation single crystal superalloys after thermal exposure. *Materials Science and Engineering A*, 627:125–134, 2025.

[13] Thermo-Calc Software AB. Thermo-calc, version 2022a. `https://www.thermocalc.com/`, 2022. Stockholm, Sweden.

[14] T. DebRoy, H. L. Wei, J. S. Zuback, T. Mukherjee, J. W. Elmer, J. O. Milewski, A. M. Beese, A. Wilson-Heid, A. De, and W. Zhang. Additive manufacturing of metallic components – process, structure and properties. *Progress in Materials Science*, 92:112–224, 2018.

[15] W. E. Frazier. Metal additive manufacturing: a review. *Journal of Materials Engineering and Performance*, 23(6):1917–1928, 2014.

[16] T. DebRoy, T. Mukherjee, J. O. Milewski, J. W. Elmer, B. Ribic, J. J. Blecher, and W. Zhang. *Additive Manufacturing of Metallic Components*. Elsevier, 2021.

[17] W. E. King, A. T. Anderson, R. M. Ferencz, N. E. Hodge, C. Kamath, S. A. Khairallah, and A. M. Rubenchik. Laser powder bed fusion additive manufacturing of metals; physics, computational, and materials challenges. *Applied Physics Reviews*, 2(4):041304, 2015.

[18] Zhiqiang Wang, Bo He, Zhenfeng Song, Liang Lan, Guoxin Lu, and Shuang Gao. Optimization of the process parameters of laser beam powder bed fusion gtd222 nickel-based superalloy based on two laser energy densities. *Metals*, 12(7), 2022.

[19] A. Deshpande, I. Anderson, H. Fiedler, E. Schwaighofer, O. Kolednik, E. Povoden-Karadeniz, T. Kremmer, G. A. Zickler, and N. Enzinger. Effect of post processing heat treatment routes on microstructure and mechanical property evolution of haynes 282 fabricated with selective laser melting. *Metals*, 10(5):629, 2020.

[20] J. T. Benzing, S. R. Whetten, E. A. Lass, M. R. Stoudt, L. E. Levine, M. E. Williams, and C. E. Campbell. Enhanced strength of additively manufactured inconel 718 by means of a simplified heat treatment strategy. *Journal of Materials Research*, 38(7):1219–1230, 2023.

[21] Bo Liu Yubi Gao Shengbing Xue Yong Hu Yutian Ding Yihang Li, Jiayu Xu. Adaptation of a heat-treatment condition to a precipitation-hardened nickel-based superalloy produced by laser powder bed fusion. *Materials Science and Engineering: A*, 880:145557, 2024.

[22] Majid Laleh, Esmaeil Sadeghi, Reynier I. Revilla, Qi Chao, Nima Haghdadi, Anthony E. Hughes, Wei Xu, Iris De Graeve, Ma Qian, Ian Gibson, and Mike Y. Tan. Heat treatment for metal additive manufacturing. *Progress in Materials Science*, 133:101051, 2023.

[23] Thibaut De Terris, Olivier Castelnau, Zehoua Hadjem-Hamouche, Halim Haddadi, Vincent Michel, and Patrice Peyre. Analysis of as-built microstructures and recrystallization phenomena on inconel 625 alloy obtained via laser powder bed fusion (l-pbf). *Metals*, 11(4):619, 2021.

[24] Michael P. Haines, Vitor V. Rielli, Sophie Primig, and Nima Haghdadi. Powder bed fusion additive manufacturing of ni-based superalloys: a review of the main microstructural constituents and characterization techniques. *Journal of Materials Science*, 57(30):14135–14187, 2022.

[25] P.K. Venkiteswaran and D.M.R. Taplin. The creep fracture of inconel x-750 at 700 °c. *Metallurgical Science*, 8:97–106, 1974.

[26] Maximilian Haack, Martin Kuczyk, André Seidel, Elena Lopez, Frank Brückner, and Christoph Leyens. Comprehensive study on the formation of grain boundary serrations in additively manufactured haynes 230 alloy. *Materials Characterization*, 164:110347, 2020.

[27] Yuanbo T. Tang, Angus J. Wilkinson, and Roger C. Reed. Grain boundary serration in nickel-based superalloy inconel 600: Generation and effects on mechanical behavior. *Metallurgical and Materials Transactions A*, 49(9):4324–4342, 2018.

[28] Qiang Tian, Wenwen Zhang, Hucheng Li, Yunlong Liu, Tonggang Lu, Jinhui Du, Xingang Liu, and Kaiyao Wang. Formation mechanism of serrated grain boundary caused by different morphologies of precipitates in gh4742 superalloy. *Journal of Materials Research and Technology*, 35:4352–4367, 2025.

[29] Pietro Antonio Martelli, Emilio Bassini, and Daniele Ugues. The effect of hot isostatic pressing pressure level and solution annealing cooling rate on cm247 lc nickel-based superalloy processed by laser-based powder bed fusion. *Progress in Additive Manufacturing*, 10(1):605–618, 2024.

[30] Y. Chen, K. Zhang, J. Huang, S. R. E. Hosseini, and Z. Li. Characterization of heat affected zone liquation cracking in laser additive manufacturing of inconel 718. *Materials & Design*, 90:586–594, 2016.

[31] Jalal Al-Lami, Thibaut Dessolier, Talha Pirzada, and Minh-Son Pham. Dislocation distribution, crystallographic texture evolution and plastic inhomogeneity of inconel 718 fabricated by laser powder-bed fusion. *Advanced Engineering Materials*, 27(9):2300524, 2023.

[32] Vera Popovich, E.V. Borisov, A.A. Popovich, V. Heurtebise, M. Heurtier, and B. Baufeld. Functionally graded inconel 718 processed by additive manufacturing: Crystallographic texture, anisotropy of microstructure and mechanical properties. *Materials & Design*, 114:441–449, 2017.

[33] Ke Ma and Jinhai Wang. Microstructural characteristics and mechanical properties of an additively manufactured nickel-based superalloy. *Crystals*, 12(10), 2022.

[34] Jinghao Xu, Håkan Brodin, Ru Lin Peng, Vladimir Luzin, and Johan Moverare. Effect of heat treatment temperature on the microstructural evolution of cm247lc superalloy by laser powder bed fusion. *Materials Characterization*, 185:111742, 2022.

[35] H.Y. Li, H.L. Sun, P. Bowen, and J.F. Knott. Effects of compressive residual stress on short fatigue crack growth in a nickel-based superalloy. *International Journal of Fatigue*, 108:53–61, 2018.

[36] Ahmed Fardan, Johannes Gårdstam, Eva Oscarsson, Håkan Brodin, and Eduard Hryha. Impact of hot isostatic pressing on microstructure evolution and creep performance of powder bed fusion–laser beam processed cm247lc. *Advanced Engineering Materials*, 27(6):2500691, 2025.

[37] P. A. Martelli, M. S. Kenevisi, E. Bassini, and D. Ugues. Definition of an optimal solutioning treatment for a ni-based superalloy processed by additive manufacturing. *La Metallurgia Italiana*, 114(7-8):28–33, 2023.

[38] E. R. Cherkasova A. V. Logunov E. A. Kuleshova. Dendritic segregation in heat-resistant nickel alloys. *Metal Science and Heat Treatment*, 23(5): 1981.